

FABRICATION AND INTEGRATION OF PERMANENT MAGNET MATERIALS INTO  
MEMS TRANSDUCERS

By

NAIGANG WANG

A DISSERTATION PRESENTED TO THE GRADUATE SCHOOL  
OF THE UNIVERSITY OF FLORIDA IN PARTIAL FULFILLMENT  
OF THE REQUIREMENTS FOR THE DEGREE OF  
DOCTOR OF PHILOSOPHY

UNIVERSITY OF FLORIDA

2010

© 2010 Naigang Wang

To my parents and my wife, Ying

## ACKNOWLEDGMENTS

Financial support for this research was provided in part by NSF grant ECCS-0716139, NASA Grant NNXX07AD94A and ARO Grant W911NF-09-1-0511.

I deeply thank my advisor, Dr. David Arnold, for giving me opportunity to work in the interdisciplinary Microsystems Group, for giving me the freedom to do what I am really interested in, for his continuous support and guidance and for all his help and career advice. I would also like to thank Dr. David Norton, for serving as my committee chair and giving me advices on the classes and exams. I am also grateful to Dr. Toshikazu Nishida for serving both my committee member and my minor representative. I would like to also acknowledge the rest of my committee members, Dr. Jacob Jones, Dr. Valentine Craciun and Dr. Simon Phillpot for reviewing my work and kind assistance.

Most of this work would not have been possible without the help of my colleagues in the Interdisciplinary Microsystems Group. I am grateful to Kamiao Jia, Mingliang Wang, Lei Wu and Sheetal Shetye for the training and assistance in the cleanroom. I would like to thank Janhavi Agashe, Benjamin Griffin, Vijay Chandrasekharan, Fei Liu, Matt Williams and Shuo Cheng for assistance with the modeling and valuable discussion. I want to thank Tzu-shun Yang, Robert Regojo and Yaxing Zhang for experimental setups and measurements. I am thankful to Alex Phipps, Jeremy Sells, Jessica Meloy, Chris Mayer, Israel Boniche and Erin Patrick for assistance with the electrical instruments. I would also like to acknowledge all of the rest members of the IMG group.

I am grateful to the staff of the Nanoscale Research Facility (NRF), Alvin Ogdon, Williams Lewis, Ivan Kravchenko, and David Hayes for their constant support and training on the facilities.

I thank all the staff of the Major Analytical Instrument Center (MAIC), Dr. Valentine Craciun, Dr. Wayne Acree and Dr. Gerald Bourne for their training and kind help.

I am also grateful to Dr. Iulica Zana at West Digital Inc. for valuable technical discussions and Dr. Florian Herrault at Georgia Institute of Technology for assistance with the laser ablation.

I would like to thank the staff of Materials Science and Engineering department and Electrical Computer Science department for their kind assistance.

I am eternally grateful to my parents, AihuaXu and Dianjun Wang for their many sacrifices for me. I would like to also thank my beloved wife, Ying Sun for her love and support.

## TABLE OF CONTENTS

	<u>page</u>
ACKNOWLEDGMENTS.....	4
LIST OF TABLES.....	9
LIST OF FIGURES.....	10
ABSTRACT .....	13
CHAPTER	
1 INTRODUCTION .....	15
1.1 Magnetic MEMS.....	15
1.2 Scaling Laws.....	16
1.2.1 Energy Density .....	17
1.2.2 Force .....	18
1.2.3 Current Density .....	21
1.3 Microscale Permanent Magnet Materials for MEMS .....	22
1.4 Research Objectives.....	24
1.5 Dissertation Overview .....	24
2 MICROSCALE PERMANENT MAGNETS-A REVIEW .....	28
2.1 Properties of Permanent Magnets .....	28
2.1.1 Magnetic Properties.....	30
2.1.2 Thermal Properties .....	32
2.1.3 Chemical Properties .....	33
2.2 Bulk Permanent Magnets.....	34
2.3 Requirements for Magnetic MEMS .....	38
2.4 Microfabricated Permanent Magnets .....	41
2.4.1 Conventionally Deposited Micromagnets .....	42
2.4.2 Powder Micromagnets.....	46
2.5 Conclusion.....	48
3 ELECTROPLATING CO-RICH CO-PT MICROMAGNETS.....	54
3.1 Electroplating Bath.....	55
3.2 Fabrication Process .....	57
3.3 Experiment Results and Discussion.....	59
3.4 Conclusion.....	61
4 MICROPACKING WAX-BONDED ND-FE-B MICROMAGNETS .....	69

4.1	Fabrication Process .....	69
4.2	Experiment Results and Discussion.....	71
4.3	Conclusion .....	72
5	INTEGRATION OF PERMANENT MAGNET MATERIALS INTO MICROTRANSDUCERS.....	78
5.1	Cantilever-Type Microtransducer .....	80
5.1.1	Operation Principle .....	80
5.1.2	Fabrication Process.....	80
5.1.3	Experiment Results .....	81
5.2	Piston-Type Microtransducer .....	82
5.2.1	Operation Principle .....	82
5.2.2	Fabrication Process.....	83
5.2.3	Experiment Results .....	84
5.3	Conclusion .....	86
6	LUMPED ELEMENT MODELING OF ELECTRODYNAMIC TRANSDUCERS .....	98
6.1	LEM of Electrodynamic Transduction .....	98
6.1.1	Electrodynamic Transduction Model.....	100
6.1.2	Transduction Coefficient Model .....	103
6.1.2	Planar Coil Model .....	104
6.1.3	Diaphragm Model .....	105
6.2	LEM of Electroacoustic Actuation Mode .....	108
6.2.1	2cc Coupler .....	109
6.2.2	Radiation Impedance.....	109
6.2.3	Complete LEM.....	110
6.3	LEM of Mechanoelectrical Generator Mode.....	113
7	EXPERIMENTAL CHARACTERIZATION AND MODEL VALIDATION OF MICROTRANSDUCERS.....	122
7.1	Lumped Parameter Extraction .....	122
7.1.1	Electrical Impedance .....	123
7.1.2	Diaphragm Impedance .....	123
7.1.3	Transduction Coefficient.....	126
7.2	Acoustic Measurements.....	126
7.3	Energy Harvesting Measurements.....	127
7.4	Conclusion .....	128
8	CONCLUSION AND FUTURE WORK.....	137
8.1	Summary and Conclusion.....	137
8.2	Suggested Future Work.....	139
	LIST OF REFERENCES .....	140

BIOGRAPHICAL SKETCH..... 148

## LIST OF TABLES

<u>Table</u>		<u>page</u>
1-1	Effect of scale reduction $k$ on magnetic force per unit volume.....	25
2-1	Typical bulk hard magnet properties.....	50
2-2	Conventionally microfabricated permanent magnets for MEMS.....	51
2-3	Powder-based permanent magnets for MEMS.....	52
5-1	Dimensions of the piston-type transducers.....	87
6-1	Conjugated power variables in various energy domains .....	116
7-1	Extracted parameters for the piston-type transducers.....	130

## LIST OF FIGURES

<u>Figure</u>	<u>page</u>
1-1 Schematic of magnetically based transduction.....	25
1-2 Breakdown voltage and breakdown field as a function of electrode separation .	26
1-3 Energy densities for constant-voltage electrostatic systems and Ni or Fe magnetostatic systems .....	26
1-4 Scale reduction of a magnet.....	27
2-1 Schematic of the domain wall movements under a magnetic field. ....	52
2-2 The two hysteresis loops of an ideal material.....	53
3-1 XRD patterns .....	63
3-2 Rocking curve around Cu (111) peak of textured seed layer.....	64
3-3 Pole figure of textured Cu (111) seed layer. ....	64
3-4 Schematic of process flow. ....	64
3-5 SEM images of 150 $\mu\text{m}$ x 150 $\mu\text{m}$ x 8 $\mu\text{m}$ Co–Pt micromagnets on an un-textured Cu seed layer .....	65
3-6 Hysteresis loops of Co–Pt micromagnet arrays on un-textured Cu seed layers.....	66
3-7 SEM images of 150 $\mu\text{m}$ x 150 $\mu\text{m}$ x 10 $\mu\text{m}$ Co–Pt micromagnets on a textured Cu (111) seed layer .....	67
3-8 Hysteresis loops of Co–Pt micromagnet arrays on textured Cu (111) seed layers.....	68
4-1 SEM image of a) raw Nd–Fe–B powder and b) wax powder .....	74
4-2 Schematic of the process flow. ....	75
4-3 Photograph of a Nd–Fe–B micromagnet array .....	75
4-4 SEM image of wax-bonded Nd–Fe–B magnet with 6.25 wt% of wax loading.....	76
4-6 Energy products and coercivities of wax bonded Nd–Fe–B micromagnets as function of wax weight percentage. ....	77

5-1	Schematic 3-D cut-away and cross-section view of a cantilever-type microtransducer.....	87
5-2	Simulated deflection of a cantilever-type microtransducer. ....	88
5-3	2D axisymmetric FEM simulation of distribution of magnetic field lines and the radial magnetic flux density in the coil plane.....	88
5-4	Fabrication process of the cantilever-type microtransducers.....	89
5-5	A cantilever-type microtransducers .....	89
5-6	Displacement measurement setup. ....	90
5-7	Normalized vibration amplitude as a function of the driving frequency for two cantilever-type microtransducers.....	91
5-8	Displacement as a function of input rms current of two cantilever-type microtransducers at 100 Hz.....	91
5-9	Schematic 3-D cut-away and cross-section view of a piston-type microtransducer.....	92
5-10	2D axisymmetric FEM simulation of the distribution of magnetic field lines and the radial magnetic flux density .....	92
5-11	The radial magnetic flux density at the coil plane of the piston-type microtransducers .....	93
5-12	Fabrication process of the piston-type microtransducers. ....	94
5-13	Schematic cross-section of copper coil with mushroom head embedded in PDMS diaphragm. ....	94
5-14	Top-view of various microfabricated piston-type transducers with different dimensions. ....	94
5-15	Bottom-view of various microfabricated piston-type transducer with different magnet patterns.....	95
5-16	Normalized vibration amplitude as a function of the driving frequency for piston-type microtransducers.....	95
5-17	Normalized vibration amplitude as a function of the driving frequency for a piston-type.....	96
5-18	Displacement as a function of input rms current.....	97
6-1	Schematic of the direction of force, velocity and radial magnetic flux density. .	116

6-2	The gyrator models for electromechanical and electroacoustical coupling. ....	116
6-3	Radial magnetic flux density at coil position for increasing magnet radius using analytical and FEM calculations. ....	117
6-4	The cross-section schematic of the composite diaphragm. ....	117
6-5	The (A) electromechanical model and (B) electroacoustic model of the piston-type transducer. ....	118
6-6	Schematic of the setup for using the transducers in acoustic actuation mode.	119
6-7	Lumped model of an acoustically short cavity. ....	119
6-8	Lumped model of radiation impedance based on an infinite baffle. ....	120
6-9	A complete LEM circuit model in an electroacoustic actuation mode. ....	120
6-10	Equivalent LEM circuit model in the acoustic domain. ....	120
6-11	A complete LEM circuit model in mechanoelectric generator mode. ....	121
6-12	Equivalent LEM circuit model in the electrical domain. ....	121
7-1	Experiment setup for the impulse response test. ....	131
7-2	Results of the impulse response test. ....	132
7-3	A typical magnetic hysteresis loop. ....	133
7-4	Experiment setup for acoustic measurements. ....	133
7-5	Acoustic measurement results and simulated results. ....	134
7-6	Experiment setup for energy harvesting measurements. ....	135
7-7	Open-circuit voltage response. ....	136

Abstract of Dissertation Presented to the Graduate School  
of the University of Florida in Partial Fulfillment of the  
Requirements for the Degree of Doctor of Philosophy

FABRICATION AND INTEGRATION OF PERMANENT MAGNET MATERIALS INTO  
MEMS TRANSDUCERS

By

Naigang Wang

May 2010

Chair: David Norton

Co-chair: David Arnold

Major: Materials Science and Engineering

Microscale permanent magnets (PM) are a key building block for magnetically based microelectromechanical systems (MEMS), such as sensors, actuators, and energy converters. However, the inability to concurrently achieve good magnetic properties and an integrated magnet fabrication process hinders the development of magnetic MEMS. To address this need, this dissertation develops methods for wafer-level microfabrication of thick (10-500+  $\mu\text{m}$ ), high-performance, permanent magnets using low-temperature ( $<180\text{ }^\circ\text{C}$ ) process steps. These methods and materials are then used to demonstrate fully batch-fabricated magnetic MEMS transducers.

Two methods to fabricate micromagnets are developed: electroplating of Co-rich Co–Pt magnets into photoresist-defined molds and micro-packing of rare-earth magnetic powders to form wax-bonded magnets embedded in silicon. Patterned micromagnets with excellent magnetic properties and process-flow compatibility are demonstrated. Electroplated Co–Pt micromagnets with thickness up to 10  $\mu\text{m}$  exhibit out-of-plane anisotropy with coercivities and energy products of 330 kA/m and 69 kJ/m<sup>3</sup>, respectively. Wax-bonded Nd–Fe–B micromagnets (500 x 500 x 320  $\mu\text{m}^3$ ) exhibit a

coercivity of 737 kA/m and a maximum energy product of 17 kJ/m<sup>3</sup> with isotropic behavior.

The wax-bonded powder magnets are then integrated into MEMS fabrication processes to batch-fabricate various electrodynamic transducer prototypes. A cantilever-type microtransducer achieves a 2.7 μm vertical deflection at a driving current of 5.5 mA<sub>rms</sub> at 100 Hz. A piston-type transducer with elastomeric membrane obtains a 2.2 μm vertical displacement at a driving current of 670 mA<sub>rms</sub> at 200 Hz. These devices demonstrate the integrability of wax-bonded Nd–Fe–B powder magnets into microscale electromechanical transducers.

Electromechanical lumped element models are then developed for the piston-type electrodynamic actuators. The models enable prediction of the device performance as an electroacoustic actuator (microspeaker) and as a mechano-electrical generator (vibrational energy harvester). Then, both the acoustic and energy harvesting performance of the prototype transducers are experimentally measured to verify the LEM models. The validated models provide a design tool for further design and development of these types of micromagnetic MEMS devices.

## CHAPTER 1 INTRODUCTION

### 1.1 Magnetic MEMS

Microelectromechanical systems (MEMS) have accomplished phenomenal growth over the past 20 years. MEMS are machines or devices that integrate micron-sized mechanical and electrical components to achieve certain engineering function by electromechanical means of sensing, actuating, or signal processing elements [1]. Much of MEMS technology is silicon based, with three-dimensional structures being fabricated from a silicon platform using various lithographic processes [2]. MEMS transducers, such as microsensors, microactuators, micromirrors and micromotors, have had a huge impact on the automotive, portable electronics, biochemical and biomedical industries. These successful applications of MEMS in industry and consumer households stimulate further related research in wide interdisciplinary engineering fields such as electrical engineering, materials science, mechanical engineering, bio-science and so on.

Magnetically based MEMS are emerging, in which electrodynamic or electromagnetic transduction schemes provide forces and torques for energy conversion instead of the electrostatic, thermoelastic, or piezoelectric forces commonly found in most MEMS. Electrodynamic transduction relies on a moving coil; motor and generator action are produced by the motion of an electric conductor located in a fixed transverse magnetic field, as shown in Figure 1-1 A. In contrast, electromagnetic transduction relies on the interaction between a magnetic field produced by an electromagnet and the induced magnetic field in a soft magnetic material. In this case, when the components of the device move with respect to each other, the magnetic field

distribution changes significantly. Figure 1-1B shows one example where motor action is produced by attractive forces tending to close the air gap.

Magnetically based transducers are commonly found in macroscale systems that have a huge impact on our daily lives. Examples of these include audio and video players, telecommunications equipment, electrical motors and generators, and hard disk drives. Magnetically based transducers offer many performance advantages when compared to other electromechanical transduction schemes. The potential key advantages of magnetic MEMS are

- High actuation force and stroke (displacement);
- Direct, fully linear transduction (in the case of electrodynamic);
- Bi-directional actuation;
- Contactless remote actuation;
- Potentially high energy density;
- Low voltage actuation;
- Biocompatibility

Thus, magnetic MEMS offer good opportunities for potential applications in the fields of acoustics (microspeakers and microphones), flow control (synthetic jets and flaps), bio-medicine (microvalves and micropumps), information technology (microdelays and microswitches), as well as energy conversion (micromotors, microgenerators and vibrational energy harvesters) [3]-[4].

## **1.2 Scaling Laws**

In order to apply magnetically based transduction schemes to MEMS, it is important to know how the device behaves when the size of the transducer shrinks down to micron size and even further to nanometer scale. Two important figures of merit will be discussed. First is the density of field energy that can be stored in an air gap by a

magnet. The other is the force-to-volume ratio (or equivalently the torque-to-volume ratio) of an actuation scheme.

### 1.2.1 Energy Density

Electrostatic actuation is well known for its favorable of scaling. In order to clearly show the energy density level of magnetic transducers, a comparison of field energy density between electrostatic and magnetic actuator is performed. More details of this discussion can be found in [3]-[4].

The field energy density of an electrostatic actuator can be simply calculated by

$$U_{electrostatic} = \frac{1}{2} \epsilon \cdot E^2 \quad (1-1)$$

where  $\epsilon$  is the permittivity and  $E$  is the electric field in the electrode gap. Since the gap is usually in air with  $\epsilon = \epsilon_0$ , the maximum energy density of electrostatic is mainly limited by the maximum electric fields. In the macro-world, this maximum electrical field is about 33 MV/m which results an energy density of 40 J/m<sup>3</sup> [3].

The field energy density of a magnetostatic actuator is given by

$$U_{magnetostatic} = \frac{1}{2\mu} B^2 \quad (1-2)$$

where  $\mu$  is the permeability of the media in the gap and  $B$  is the magnetic flux density. Therefore, the maximum energy density of magnetic actuators is basically limited by saturation magnetic flux density  $B_{sat}$ . The flux densities of common soft ferromagnetic metals, such as Ni and Fe, are about 1–2 T. Thus, assume only air in the gap, the resulting energy density is about 2,000,000 J/m<sup>3</sup>, which is 50,000 times larger than the electrostatic case. This explains why magnetic actuators dominate macroscopically [3].

When a device is scaled down, however, a larger electric field can be applied across the electrode gap, as shown by the *Paschen* curve in Figure 1-2. Thus, the maximum energy density of electrostatic actuators increases as the gap becomes smaller. On the other hand, the maximum energy density of magnetic actuators is independent of scale, assuming constant magnetic material properties. Therefore, when the size scales down, the maximum energy density of electrostatic and magnetic will meet at a crossover point, which is about 1-3  $\mu\text{m}$ , as shown in Figure 1-3. In other words, if the size of an air gap is smaller than 1-3  $\mu\text{m}$ , the electrostatic is favorable, but above this dimension, the magnetic actuator is preferred.

### 1.2.2 Force

The force and torque that can be obtained from an electromechanical interaction is another important consideration for an actuator designing. The scaling laws for forces and torques created by different magnetic interaction involving permanent magnets, soft magnets, and current carrying coils have been discussed in detail by [5]. Since it is important for this work, a brief summary is given below.

Consider first the scaling of the magnetic field created by a permanent magnet of volume of  $V$  and a constant magnetization of  $M$ . The magnetic field  $H$  generated by the magnet at point  $P$  is given by [5]

$$H = \frac{V}{4\pi} \frac{\vec{M} \cdot \vec{r}}{r^4} \quad (1-3)$$

where  $r$  is the distance from magnet to point  $P$ .

When all dimensions are scaled down by a factor of  $k$  (where  $k$  is a essentially a “shrinkage factor”), then  $r' = r/k$  and  $V' = V/k^3$ , where the value with prime is the value

after scale reduction. The resulting magnetic field remains unchanged with scale, as depicted in Figure 1-4.

$$H' = \frac{V'}{4\pi} \frac{\vec{M} \cdot \vec{r}'}{r'^4} = \frac{V}{k^3} \frac{\vec{M} \cdot \frac{\vec{r}}{k}}{\left(\frac{r}{k}\right)^4} = \frac{V}{4\pi} \frac{\vec{M} \cdot \vec{r}}{r^4} = H \quad (1-4)$$

In other words, a large magnet and a small magnet possess the same magnetization, and thus are capable of producing similar external magnetic field strengths. This is because the source of the magnetic field from a permanent magnet is residual material magnetization, which arises at the atomic level.

In contrast to the field from a magnet, the magnetic field created by an electric current scales differently. The field from a conductor of infinitesimal length  $d\vec{l}$  is given by the Biot-Savart law as

$$\vec{H} = \frac{1}{4\pi} \cdot \int_l \frac{J \cdot S \cdot d\vec{l} \times \vec{r}}{r^3} \quad (1-5)$$

Where  $r$  is the distance from the conductor segment to a point  $P$ ,  $S$  is the cross-section of the coil and  $J$  is the current density. Assuming constant current density, the field  $H$  generated by the conductor is divided by  $k$ , after scale reduction of  $k$ .

$$\vec{H}' = \frac{1}{4\pi} \cdot \int_l \frac{J \cdot S \cdot d\vec{l}' \times \vec{r}'}{r'^3} = \frac{1}{4\pi} \cdot \int_l \frac{J \cdot S \cdot \frac{d\vec{l}}{k} \times \frac{\vec{r}}{k}}{\left(\frac{r}{k}\right)^3} = \frac{\vec{H}}{k} \quad (1-6)$$

Hence, magnetic fields from a current-carrying electromagnet scale unfavorably with diminishing size.

Now consider the magnetic force  $F$  acting on magnetic materials, which can be calculated by,

$$\vec{F} = -V \cdot \nabla(\vec{M} \cdot \vec{H}) \quad (1-7)$$

Where  $M$  and  $V$  are the magnetization and the volume of the magnetic material, respectively, and  $H$  is the magnetic field created either by another magnet or a current carrying coil. How the force scales is dependent on how the magnetic field scales, i.e. whether the magnetic field is from a permanent magnet or a current-carrying coil.

**Interaction between magnets.** As shown by equation (1-3), the magnetic field generated by this PM does not change in amplitude and geometrical distribution. Consider now a second PM or a soft magnet (SM) placed nearby the first PM. The magnetization of  $M$  of this second PM or SM is also unchanged with scale. Thus, equation (1-7) becomes

$$\vec{F}' = -V' \cdot \nabla(\vec{M}' \cdot \vec{H}') = -\frac{V}{k^3} k \nabla(\vec{M} \cdot \vec{H}) = \frac{F}{k^2} \quad (1-8)$$

Therefore, for PM-PM or PM-SM interactions, the interaction force  $F$  only decreases by  $k^2$ . Thus the force to volume ratio will increase by  $k$ , which means that systems using the attraction or repulsive forces between magnetic materials (will greatly benefit from being downscaled [5].

**Interaction between permanent magnet and conductor.** With scale reduction of  $k$ , the magnetic field generated by a conductor will be decreased by  $k$  according to equation (1-6). The magnetization of PM remains unchanged, so, equation (1-7) becomes

$$\vec{F}' = -V' \cdot \nabla(\vec{M}' \cdot \vec{H}') = -\frac{V}{k^3} \nabla(\vec{M} \cdot \frac{\vec{H}}{k}) = \frac{F}{k^3} \quad (1-9)$$

Therefore, the force to weight/volume ratio remains unchanged. Thus the most popular electrodynamic transduction as shown in Figure 1-1(a) works as well at small dimensions as it does at macroscopic dimensions.

**Interaction between soft magnet and conductor.** In this case, the situation depends on whether the field created by the conductor is high enough to saturate the soft magnet. If the field can saturate the SM, the magnetization of SM will not change with scale so that the force to volume ratio remains unchanged. However, if the magnetic field generated by conductor is weak, the magnetization of SM will depend on the magnitude of the magnetic field. Therefore, the force per unit volume will be scaled down by  $k$ .

### 1.2.3 Current Density

Because of their high surface-to-volume ratio, microscale coils can withstand much higher current densities than macroscopic conductors ( $10^6$ – $10^8$ A/m<sup>2</sup> vs.  $10^6$ A/m<sup>2</sup>)[5]. Moreover, MEMS devices are often fabricated on silicon substrates, which provide good heat conduction and thus minimize Joule heating. Thus, when shrinking physical dimensions, the current density may increase by a factor  $k_i$ , and thus the field from a current-carrying coil may similarly increase according equation 1-5. Assuming this favorable benefit modifies the force scaling laws described in the previous sections.

Table 1-1 summarizes the effect of scale reduction  $k$  and increased current density  $k_i$ , on the force per unit volume of different magnetic interactions. In summary, all magnetic interactions involving permanent magnets are favorable of geometric scaling.

In contrast, the use of current-carrying coils to create magnetic fields only scales favorably if higher current densities are used. In this case, however, the coils are limited by Joule heating.

### **1.3 Microscale Permanent Magnet Materials for MEMS**

As suggested above by the scaling laws, microscale permanent magnets are a critical enabling component for the development of high-performance microscale magnetic machines such as motors, generators, switches, pumps, acoustic speakers, energy harvesters, etc. However, the application of permanent magnets at the microscale has been fairly limited, with the notable exception of magnetic recording media. The reason is that the methods for magnet fabrication at the macroscale—casting and powder processing—are hardly applicable to traditional thin-film microfabrication approaches—physical vapor deposition, chemical vapor deposition, or electrochemical deposition. While there is a wealth of information on both soft and hard magnetic thin films as it relates to magnetic media [6]-[7], these films are too thin (often less than 100 nm) to be applicable for most magnetic MEMS. For example, magnetic actuators are more favorable than electrostatic actuators when the actuation gap is greater than  $\sim 2 \mu\text{m}$  [3]. This implies the need for relatively voluminous (thick) magnetic structures in order to establish reasonably strong magnetic fields over multi-micron length scales.

The design and fabrication challenges of application and integration of hard magnets in MEMS include,

1. The need for relatively thick films of hard magnetic materials is somewhat unique to MEMS applications.

2. There are different classes of hard magnetic materials, each with strengths and weaknesses. Magnetic performance, temperature effects, chemical stability, and fabrication constraints all play a role in the material selection and microfabrication strategy.

3. The material properties of most hard magnets are typically quite sensitive to both microstructure and chemical composition. This requires careful control over the processing conditions and may require the application of magnetic fields, additional thermal steps, or other processing steps to induce optimal magnetic properties, thus adding cost and complexity to the fabrication.

4. Hard magnets require in situ or post-fabrication magnetization steps to “pole” the magnets in a specific direction. This complicates the integration process, particularly for wafer-scale batch-fabrication.

5. Perhaps most importantly, the total system performance of a permanent-magnet-based system is usually limited by the magnet. Thus, the quality and performance of the magnetic material plays a critical role in the overall design.

In 1996, when magnetic MEMS started to attract attention, MEMS pioneer Henry Guckel remarked that “*Permanent magnets are vital to magnetic actuation, but that unfortunately their integration still needs to be mastered*” [8]. Unfortunately, more than a decade later, this statement still mainly true [5]. As a result, researchers often have to machine micromagnets from bulk magnets and manually assembly individual magnets into devices. However, this method is hardly compatible with small scale integration or batch fabrication.

## **1.4 Research Objectives**

The objectives of this work are to develop new methods for microfabricating thick (10-100+  $\mu\text{m}$ ), high-performance, PM materials and to integrate these materials within complex MEMS process flows to fabricate MEMS transducers.

## **1.5 Dissertation Overview**

This dissertation is organized into seven chapters. The first chapter discusses the motivation of this work and the research goal. Chapter 2 reviews the microscale permanent magnets for MEMS. Chapter 3 and Chapter 4 introduce two new methods developed to fabricate microscale permanent magnets: (1) electroplating of Co-rich Co–Pt magnets into photoresist-defined molds and (2) micro-packing of wax-bonded rare-earth magnets to form magnets embedded in silicon, respectively. Chapter 5 presents the electrodynamic microtransducers fabricated based on micropacked magnets. Chapter 6 discusses lumped element modeling of the transducers in two different operating modes: (1) as an electroacoustic actuator (microspeaker) and (2) as a mechano-electrical device (vibrational energy harvester). Then in Chapter 7, the models are verified experimentally. Finally, Chapter 8 provides conclusions and suggestions for future work.

Table 1-1. Effect of scale reduction  $k$  on magnetic force per unit volume, taking into account increased admissible current density  $k_i$  [Adapted from [5] O. Cugat, 2003. (Page 3609, Table I). Divided attention, perception and auditory recall]

Reduction Factor (1/k)	Permanent Magnet	Soft magnet	Conductor
Magnet	$\times k$	$\times k$	$\times k_i$
Current	$\times k_i$	$\times k_i/k$	$\times k_i^2/k$

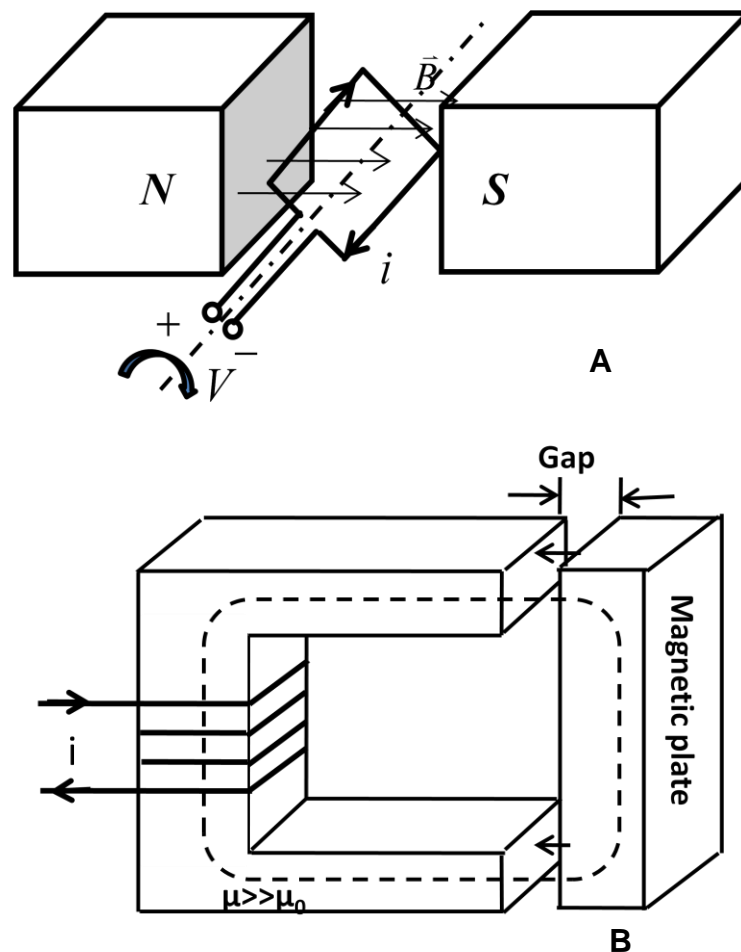


Figure 1-1. Schematic of magnetically based transduction. A) Electrodynamic transduction; B) Magnetic transduction [Adapted from [12] E. P. Furlani, 2001. (Page 337, Figure5.1). Divided attention, perception and auditory recall].

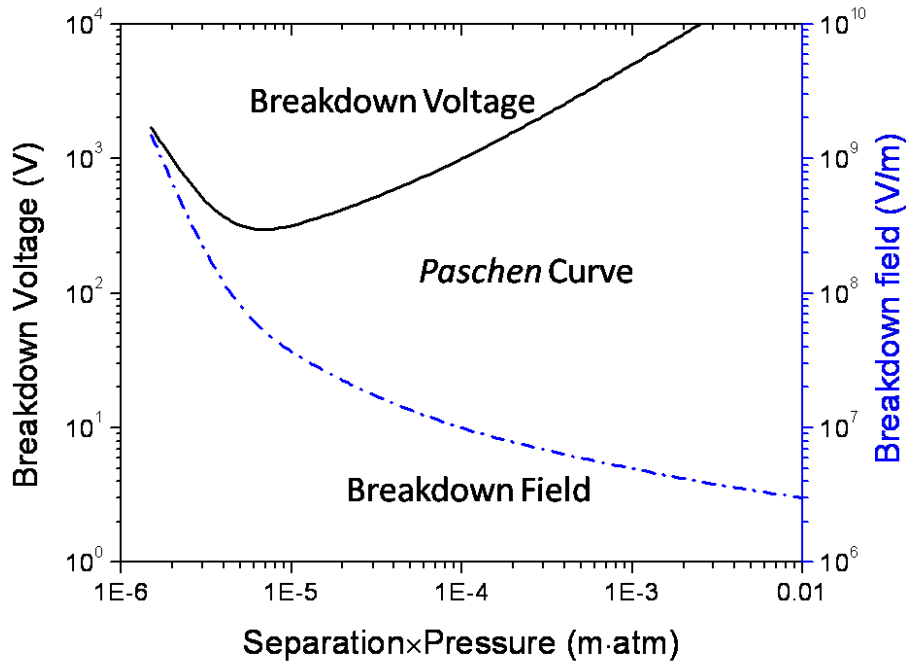


Figure 1-2. Breakdown voltage and breakdown field as a function of electrode separation [Adapted from [3] J. W. Judy, 2001. (Page 1118, Figure2). Divided attention, perception and auditory recall].

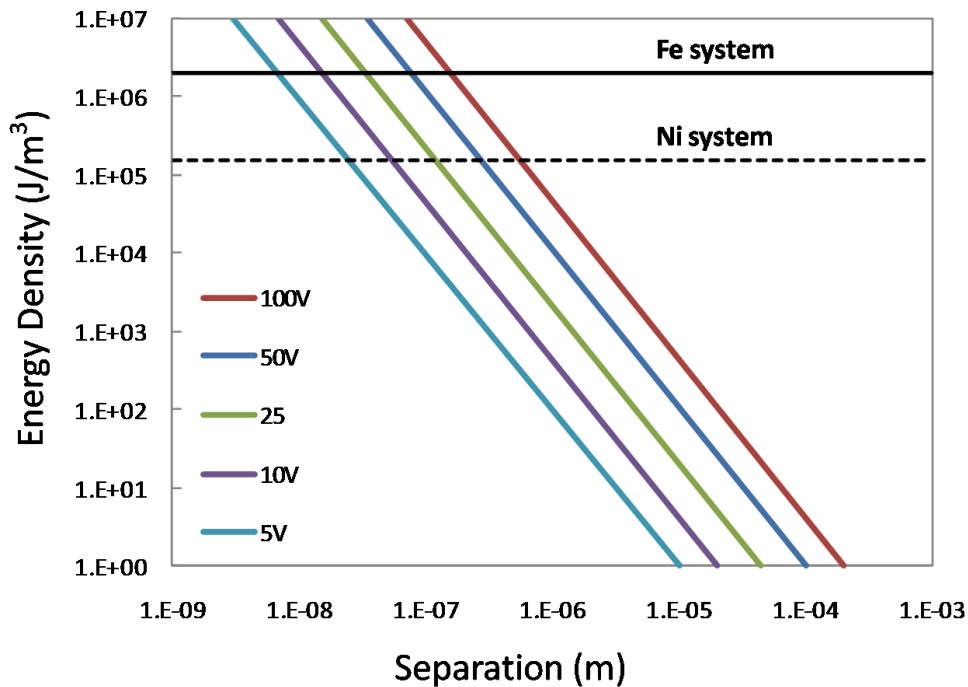


Figure 1-3. Energy densities for constant-voltage electrostatic systems and Ni or Fe magnetostatic systems [Adapted from [3] J. W. Judy, 2001. (Page 1118, Figure 3). Divided attention, perception and auditory recall].

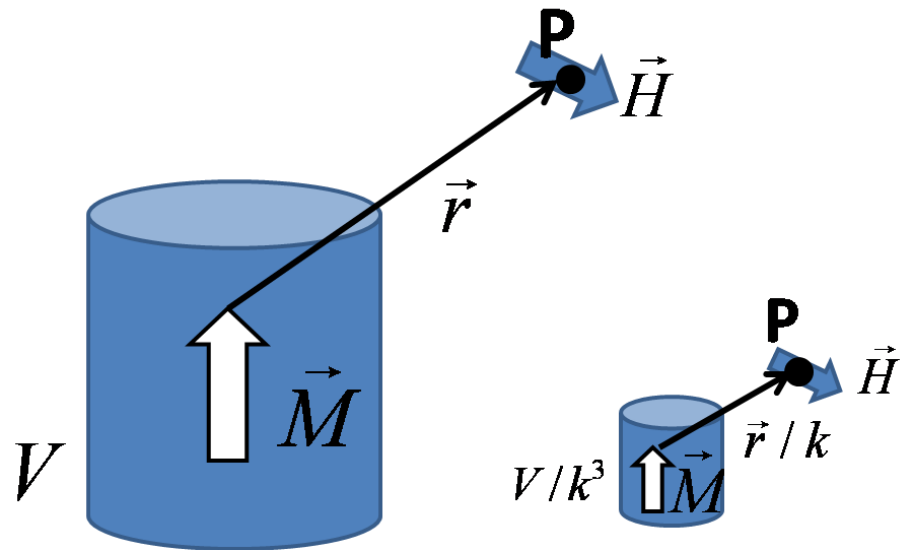


Figure 1-4. Scale reduction of a magnet [Adapted from [5] O. Cugat, 2003. (Page 3608, Figure 2). Divided attention, perception and auditory recall].

## CHAPTER 2 MICROSCALE PERMANENT MAGNETS-A REVIEW

Portions of this chapter are reproduced with permission from IEEE from the following article: D. P. Arnold and N. Wang, "Permanent Magnets for MEMS," *J. Microelectromech. Syst.*, vol. 18, pp. 1255-1266, 2009.

This chapter reviews the state of the art for microfabrication of permanent magnets applicable to microelectromechanical systems (MEMS). Basic theories and operational concepts for permanent magnets are first described. Then, different classes of permanent magnet materials and associated performance tradeoffs are introduced. Challenges relating to the integration of permanent magnets into MEMS applications are then discussed. Lastly, a detailed summary and review of previously reported fabrication strategies and material properties is provided.

### **2.1 Properties of Permanent Magnets**

Permanent magnets are ferromagnetic or ferrimagnetic materials that exhibit a strong magnetization in the absence of an external magnetic field. Once magnetized, they provide a "free" source of magnetic field, requiring no external power. In contrast, soft magnets only become magnetized in the presence of an external magnetic field, either from a current-carrying wire or a permanent magnet. Hard magnets are often coupled with soft magnetic cores to guide and concentrate magnetic fields in specific regions, e.g. across coils for an electrodynamic actuator.

This section describes important material properties for hard ferromagnetic materials from an engineering perspective. For design purposes, the most relevant engineering properties are the magnetic properties (intrinsic coercivity, coercivity, remanence, maximum energy product); the thermal properties (Curie temperature,

maximum operating temperature, temperature coefficient of remanence); and the chemical stability. More thorough treatments of these topics can be found in [9]-[13].

In the localized moment theory [10], each atom is assumed to possess a small vector magnetic moment. The total magnetic moment of a magnet is the superposition (vector sum) of all the atomic moments that comprise the magnet. Dividing this total magnetic moment by the volume of the region yields the magnetization, denoted  $M$ . The magnetization is a vector field quantity describing the magnetic moment density.

In a ferromagnetic material, the neighboring magnetic moments tend to align parallel with each other due to exchange coupling of quantum mechanical origin, which macroscopically gives rise to a “spontaneous” magnetization. This strong spontaneous magnetization is the origin of the strong magnetic performance of a ferromagnetic material. The magnetic moments are also interacting with the crystalline lattice, which results in crystalline-dependent magnetoanisotropy. In addition, each magnetic moment has magnetic dipolar interactions with other moments. As a result of these three interactions, a bulk ferromagnetic material decomposes into magnetic domains. Each domain typically has  $10^{17}$ – $10^{21}$  atoms [11].

Inside of each domain, the local magnetization is oriented along one of the equivalent easy magnetization axes, depending on the crystal structure of the materials. Neighboring domains orient in an equivalent easy axes in a manner so as to minimize magnetostatic energy. When an external magnetic field is applied to a ferromagnetic material, the magnetic moments will rotate/switch in order to align with the external field. Microscopically, this is achieved by the moving of domain wall between magnetic domains, as shown in Figure 2-1. Macroscopically, a nonlinear hysteresis loop is

formed, as shown in Figure 2-2. Therefore, the hysteresis loop can be treated as characteristic of ferromagnetic materials.

### 2.1.1 Magnetic Properties

There are three vector fields that define the state of a magnet: the magnetic flux density,  $\vec{B}$ , the magnetic field,  $\vec{H}$ , and the magnetization,  $\vec{M}$ . At any given point, these field quantities are related by the constitutive equation  $\vec{B} = \mu_0(\vec{H} + \vec{M})$ , where  $\mu_0 = 4\pi \times 10^{-7}$  H/m is the permeability of free space. The magnetic properties of a material are often characterized by measuring the magnetization while cycling the magnetic field, the so called  $M$ - $H$  loop. An equivalent  $B$ - $H$  loop can be derived from the  $M$ - $H$  loop via the constitutive equation, and vice versa, depicted in Figure 2-1. These two plots have slightly different appearance and interpretation, but convey similar information.

One confusing aspect is the magnetic field in the constitutive equation and depicted in Figure 2-1 is the total internal field,  $H = H_{tot} = H_a + H_d$ , where  $H_a$  is an externally applied field and  $H_d$  is an internally generated demagnetizing field. In any finite-length magnet, a demagnetizing field arises because of the free magnetic poles at the terminating ends of the magnet. This strength of the field is dependent on the magnetization and the physical magnet shape; furthermore, it acts in a direction opposite to the magnetization, essentially acting to demagnetize the magnet. The demagnetizing field is generally expressed as  $H_d = -N_d M$ , where  $N_d$  is the demagnetization factor. Values for  $N_d$  can be found in [10].

The important ramification of this demagnetizing field is that when a permanent magnet is used as a source of magnetic flux, its operating point is somewhere in the

second-quadrant of the hysteresis loop; the internal magnetic field  $H$  is actually in opposite direction to the magnetic flux density  $B$  and magnetization  $M$ . This second-quadrant portion of the hysteresis loop, known as the demagnetization curve, provides the critical information necessary for magnetic design.

The key features of the hysteresis loop for a permanent magnet are described as follows. The intrinsic coercivity,  $H_{ci}$ , is the reversal magnetic field required to force the magnetization to zero. The coercivity,  $H_c$ , is similarly the reversal magnetic field required to force the magnetic flux to zero. Practically speaking, the coercivity values indicate how hard it is to magnetize or demagnetize the magnet, with larger coercivities preferred.

In contrast, the remanence,  $B_r$ , indicates how strong a magnet is, once magnetized. More specifically,  $B_r$  is the maximum magnetic flux density that the magnet can provide. This maximum value is only achieved when the total internal magnetic field is zero. For a simple magnet, this specific condition is only met if the end poles of the magnet are “short-circuited” by a highly permeable magnetic structure, thus eliminating all internal demagnetizing fields. However, in this configuration, the magnetic fields are completely contained within the magnetic structures (no air gaps), so this is of limited practical use, except perhaps for latching-type structures.

While the coercivities and remanence indicate theoretical material limits, the normal operating point for a magnet is somewhere in between these bounds. For a simple magnet in free space, the  $B$ -fields near the pole surfaces are usually only 20–50% of  $B_r$ . The product of  $B$  and  $H$  has units of energy density,  $\text{kJ/m}^3$ . The maximum energy density product,  $(BH)_{max}$ , is the operating point where the product  $|B \cdot H|$  is

maximized in the 2nd quadrant. This value represents an operating point where the magnet can supply the most magnetic energy to an air gap, particularly important for actuator applications [12]. As such, the maximum energy product (often termed “energy product” for conciseness) is often used as the primary figure-of-merit for comparison of hard magnetic materials.

### **2.1.2 Thermal Properties**

The performance of a permanent magnet is highly dependent on temperature, with properties generally decreasing with increasing temperature. This motivates several system design considerations. The first is selection of suitable magnet materials that can withstand the highest operating temperatures expected in a given application. This is important because heating a magnet too hot may cause permanent degradation to the magnetization. Additionally, a material with only moderate room-temperature performance may at higher temperatures excel over other materials. A second design consideration is to understand how temperature variations affect the magnetic properties and thus affect the overall system. This is critical to ensure consistent performance (or at least quantifiable temperature sensitivity) over a specified operational temperature range.

While not universally true, in many magnets the remanence, coercivity, intrinsic coercivity, and energy product all decline with increasing temperature. (A counter example to this generalization is ferrite magnets, where the coercivity can increase with temperature over a certain range [11].) Any thermally induced change may be reversible or irreversible, depending on the magnitude temperature change.

For a thermally demagnetized magnet, the full magnetization can usually be recovered by remagnetization with a magnetic field, so long as chemical or

microstructural changes have not occurred (e.g. oxidation, phase change). Note, however, once a magnet is installed in an application, remagnetization may be not possible. To avoid in situ performance degradation, magnets are often heated before installation to a level above the expected operating temperature. This “burn-in” procedure results in a one-time performance decline, but ensures the magnets remain thermally stable once in use.

The relevant thermal properties are quantified as follows. The maximum operating temperature  $T_{max}$  is defined as the temperature above which irreversible changes occur. The Curie temperature  $T_c$  is the temperature above which a magnet no longer exhibits any net magnetization. The Curie temperature is well-defined intrinsic material property for a given composition; above it, a magnetic phase transition occurs, and the material exhibits a paramagnetic rather than ferromagnetic behavior [10]. While  $T_c$  provides an absolute upper limit for material magnetization,  $T_{max}$  is often several hundred degrees Celsius lower, and it usually sets the practical temperature limit. Below  $T_{max}$ , the reversible magnetization degradation is usually quantified by the reversible temperature coefficient of remanence  $\alpha$  (units of % / °C). This value is the initial slope of the curves, which indicates the temperature stability of a material.

### **2.1.3 Chemical Properties**

In addition to the temperature stability, chemical stability is a key concern for two reasons. First, in application a magnet may be exposed to standard atmospheric conditions, so an important consideration is a magnet’s propensity for oxidation, especially when considering small magnets with high surface-area-to-volume-ratios. Second, thinking ahead toward microfabricated devices, a microfabricated magnet in an integrated process flow may be subjected to numerous chemical treatments. Thus, a

magnet must be able to survive short-term chemical exposure and long-term exposure to the ambient atmosphere.

Certain magnet compositions (especially rare-earth magnets) readily oxidize in normal ambient air [11]. This oxidized layer is not strongly magnetic, and thus reduces the net magnetic volume. Protective coatings or alloy modifications are often used in order to increase the corrosion resistance. While the qualitative chemical stability of different alloys is widely discussed, quantitative characterization of corrosivity is less commonly reported. Where reported, characterization of corrosion is usually performed by standard electrochemical methods measuring corrosion potential and corrosion current density. Additionally, oxidizing tests are usually performed in an oven at 80 °C in 80% relative humidity atmosphere and followed by chemical analysis of the surface (e.g. EDS or XPS) [14].

## **2.2 Bulk Permanent Magnets**

Before delving into microscale magnets, the well-known properties and tradeoffs of bulk permanent magnet materials are first discussed. Macroscale hard magnets are most commonly created by powder metallurgical processes, and to a lesser degree, casting. A thorough description of permanent magnet manufacturing can be found in [11]. To create a magnet, the desired magnetic alloy is first blended by melting appropriate quantities of the raw elements in large furnaces. To form cast magnets, the molten mixture is poured into a mold and allowed to cool. For powder-based magnets, the cooled alloy material is usually ball-milled or jet-milled to form fine powders. Particle sizes range from a few micrometers up to hundreds of micrometers. The powders are then pressed into molds to create a desired shape. Subsequent or simultaneous heat treatments (sintering) are used to bond the powder and also to induce precipitation,

diffusion, or microstructural changes to enhance the magnetic properties. Magnetic fields can also be applied to achieve preferred magnetic orientations (anisotropy).

Because most of the high-performance magnetic materials are brittle, the magnetic powders are often augmented with organic binders to create bonded magnets. These bonded magnets are more mechanically robust and can be formed into complex shapes using extrusion or injection molding processes. However, because of the volumetric dilution from the binder material, these bonded magnets exhibit decreased magnetic properties in comparison to fully-dense sintered or cast magnets.

Common, bulk permanent magnet materials can be broadly categorized as low-energy-density ferrites (e.g.  $\text{BaFe}_{12}\text{O}_{19}$ ,  $\text{SrFe}_{12}\text{O}_{19}$ ), medium-energy-density metal alloys (e.g. Al–Ni–Co, Fe–Pt, Co–Pt alloys), or high-energy-density rare-earth alloys (e.g.  $\text{SmCo}_5$ ,  $\text{Sm}_2\text{Co}_{17}$ ,  $\text{Nd}_2\text{Fe}_{14}\text{B}$ ). Table 2-1 summarizes some of the more common bulk alloys and relevant material selection considerations.

**Ferrites.** Most hard ferrites have composition of  $\text{MO}\cdot 6(\text{Fe}_2\text{O}_3)$ , where the metal M is usually Ba, Sr, or sometimes Pb. These ceramic materials are technically ferrimagnetic, but their macroscopic behavior is similar to a ferromagnet. The material composition is usually formed by reacting a metal carbonate, e.g.  $\text{BaCO}_3$ , with iron oxide  $\text{Fe}_2\text{O}_3$ , e.g. to form  $\text{BaO}\cdot 6(\text{Fe}_2\text{O}_3)$ . From there, powder processing is the preferred manufacturing method, and both sintered and bonded ferrite magnets are commonly found. The particle size (few micrometers for most hard ferrites) is often much smaller than the metal-alloy or rare-earth magnetic powders, since ferrites are not subject to deleterious oxidation like other common hard magnetic materials.

Ferrites usually exhibit hexagonal microstructure, which leads to significant uniaxial crystalline anisotropy and a large magnetic hysteresis. In spite of their relatively limited magnetic properties (remanence  $\sim 0.4$  T, intrinsic coercivity  $\sim 380$  kA/m, energy product up to  $\sim 30$  kJ/m<sup>3</sup>), hard ferrites are the most commonly used general-purpose magnets because of their low cost and excellent corrosion resistance.

**Transition metal alloys.** Transition metal alloy magnets (or just “metal alloy” for brevity) employ ferromagnetic transition-metal elements of Fe, Co, and Ni with other non-ferromagnetic metal elements such as Al, Pt, or Cr. Historically, ferrous steels were widespread as permanent magnets, but their magnetic properties are so low by today’s standard, they are rarely considered. Metal alloy magnets are usually manufactured by direct casting, but powder processing methods are also sometimes used.

Al–Ni–Co (often written “Alnico”) magnets—alloys consisting primarily of Al, Ni, and Co with traces of Cu, Fe, and Ti—were one of the earliest high-performance hard magnets, heavily developed in the 1940’s. Alnico magnets have high remanence (0.7-1.3 T) but relatively low intrinsic coercivity (40-170 kA/m). In application, the low coercivity makes them susceptible to demagnetization or remagnetization. The hard magnetic properties arise from fine, rod-shaped particles precipitated from the matrix, which induce strong shape anisotropy. Al–Ni–Co magnets are not widely used today because of their low coercivity, poor mechanical properties and relative high cost. However, their excellent thermal stability and high Curie temperature makes them suitable for high-temperature applications. Other similar but less widely employed bulk alloys include Fe–Co–Cr and Cu–Ni–Fe, which have better ductility compared to Al–Ni–Co [9].

Binary alloys of Co–Pt and Fe–Pt have also been shown to exhibit impressive magnetic properties. The most interesting is the so-called  $L1_0$  phase, which is a 50:50 composition of either Co or Fe with Pt having face-centered tetragonal structure and exceptionally strong uniaxial crystalline anisotropy. Unfortunately, Co–Pt and Fe–Pt alloys are rarely used because of the extremely high cost of Pt. They are sometimes found in niche applications that require high corrosion resistance and good mechanical properties [13].

**Rare-earth alloys.** Many rare-earth lanthanide elements are ferromagnetic, but with Curie temperatures well below room temperature. Rare-earth permanent magnets combine rare-earth and transition-metal elements to form compounds with strong ferromagnetic behavior at room temperature. Alloys of Sm–Co and Nd–Fe–B are the two most common commercially available rare-earth magnets, known for their exceptionally high magnetic strength. These magnets are almost exclusively manufactured from powders to form sintered or bonded magnets. General weaknesses of rare-earth magnets are their susceptibility to oxidation and their relatively low operating temperatures.

Two different alloys of Sm–Co are common,  $\text{SmCo}_5$  and  $\text{Sm}_2\text{Co}_{17}$ .  $\text{SmCo}_5$  exhibits higher coercivity but lower remanence, whereas  $\text{Sm}_2\text{Co}_{17}$  exhibits higher remanence but lower coercivity. The energy products are up to  $\sim 180 \text{ kJ/m}^3$  for  $\text{SmCo}_5$  and  $\sim 240 \text{ kJ/m}^3$  for  $\text{Sm}_2\text{Co}_{17}$ . Sm–Co alloys have very high Curie temperature (720–900°C), a benefit of the high Co content. The drawback is that Co is becoming increasingly expensive, making Sm–Co magnets more costly than their better-performing Nd–Fe–B counterparts. Compared to Nd–Fe–B, the advantage of Sm–Co alloys is better chemical

stability and higher maximum operating temperature, generally in the range of 250-350 °C. Some special alloys have been developed with for temperatures up to 550 °C [16]. Therefore, despite their relatively high cost, Sm–Co alloys find use in high-temperature, high-performance applications.

Nd–Fe–B magnets, usually the alloy  $\text{Nd}_2\text{Fe}_{14}\text{B}$ , show the highest magnetic performance (energy product up to  $400 \text{ kJ/m}^3$ ) of all widely manufactured magnets. They are readily available in various shapes and sizes at relatively low cost. The primary disadvantages of Nd–Fe–B magnets are poor corrosion resistance and very low maximum operation temperature (125-150 °C). The magnet surfaces are almost always coated with a metal coating (usually Ni) to limit degradation, even for room temperature applications.

### 2.3 Requirements for Magnetic MEMS

The application of permanent magnets at the microscale requires many considerations. Most MEMS devices and process flows are highly custom and application specific. Each system has different needs and different constraints (size, performance, temperature range, cost, process limitations, etc.). Thus, no single magnetic material or fabrication process will meet all needs. However, there are some general goals that are common to many MEMS platforms. Before delving into previously published results, it makes sense to first describe rough targets for desired properties, and to provide examples of tradeoffs in the selection of suitable magnetic materials.

**Magnet size.** For MEMS device design, relatively large magnetic volumes are often desired in order to achieve large magnetic fields, magnetic forces, or electromechanical energy exchange. For example, unlike electrostatic forces, which are dependent on surface area, magnetic forces depend on volume. Additionally, one

advantage of a magnet is the ability to create magnetic fields over fairly long distances, e.g. for actuators with large working gaps. However, the magnetic field emanating from the surface of a magnet decays rapidly with distance (e.g. the field from a magnetic dipole decays). While it is possible to achieve strong magnetic fields over long distances, this requires magnets of substantial size. Typical magnet dimensions required for MEMS range from a few micrometers to hundreds of micrometers, or possibly even larger depending on the application.

**Material performance.** For functional use, a magnet should exhibit strong magnetic properties and suitable thermal and chemical stability for the intended application. As discussed in the previous section, general material tradeoffs are well documented for bulk materials. For microscale magnets, temperature and chemical stability are generally similar to the macroscale material properties. However, the magnetic performance of microscale magnets is often lower than in bulk, largely due to process and integration constraints (discussed further below). A decent quality microscale magnet could be expected to have  $H_{ci} > 200$  kA/m,  $B_r > 0.5$  T, and  $(BH)_{max} > 30$  kJ/m<sup>3</sup>, roughly the performance of a bulk ferrite magnet.

Also, while chemical reactivity is expected to be about the same between macroscale and microscale magnets, corrosion/oxidation effects become more important at small size scales, where surface area to volume ratios become large. For example, a 50  $\mu\text{m}$  thick “skin” of oxidation may be tolerable on a 1 cm<sup>3</sup> magnet, but certainly not in a 100  $\mu\text{m}$  thick magnetic film, since half of the film would no longer be magnetic.

**Process integration.** One of the biggest challenges for realizing microscale magnetic systems is process integration. Unlike bulk magnetic devices where magnets are separately manufactured and then assembled into the final system, microfabrication demands monolithic integration of the magnets within a multistep, sequential process flow. This integrated manufacturing approach places constraints on the magnetic materials and processes that are not normally found in macroscale manufacturing.

First, wafer-level deposition processes are desired to maintain the cost, throughput, and repeatability advantages afforded by batch-fabrication. As described previously, most macroscale magnets are manufactured using processes (casting, powders) that are very different than commonly employed in microfabrication. Thus, to be suitable for microsystem integration, different processing approaches are needed.

Second, deposited micromagnets should be lithographically defined in order to form precise, aligned geometries for device design. This requires methods for selective deposition (e.g. electroplating, screen printing, etc.) or selective etching of blanket-deposited magnetic layers. Chemical etchants for many of the complex magnetic alloys are not widely known, so selective deposition may be highly preferred.

Third, the magnets should be deposited at low temperatures and avoid post-annealing requirements, so other integrated circuits or common MEMS materials (e.g. polymers, Al) can survive the process conditions. Ideally, room-temperature processes are preferred, but at minimum, processing temperatures should be kept below 450 °C for potential post-CMOS compatibility.

Fourth, not only should deposition of the magnets not affect pre-existing structures on a wafer, the deposited magnets must also be stable enough to survive any

subsequent processing steps (e.g. photolithography, chemical etching, plasma processes, thermal steps, etc.).

All of these integration issues place strict limitations on material selection and fabrication methods. For example, metal alloys can be deposited by electrodeposition or physical vapor deposition. Electroplating offers a relatively low-cost, high-deposition-rate approach for achieving multi-micron films, as well as the ability to selectively deposit material using photoresist masks [17]. In contrast, vapor deposition is usually slower, more costly, and requires post-deposition etching or polishing steps to define the pattern since standard “lift-off” methods may not work with thick layers. While electroplating may seem highly desirable, it requires careful control over many process parameters and often suffers from lack of repeatability. Additionally, ferrites and rare-earth magnets cannot be electrodeposited from aqueous solutions, so vapor deposition or other methods are necessary. In general, there are many tradeoffs in the selection of a material and fabrication approach.

## **2.4 Microfabricated Permanent Magnets**

With a general understanding of magnetic materials and the hurdles for application at the microscale, this section now presents a review of permanent magnet materials suitable for MEMS integration. This summary is restricted to permanent magnets that can be deposited or grown on typical MEMS substrates (e.g. Si, glass) and have film thicknesses of at least 0.5  $\mu\text{m}$ . This specifically excludes magnets that require manual assembly for integration, magnets on “exotic” substrates, and very thin magnetic films. The discussion is divided into two sections. The first subsection describes micromagnets fabricated using conventional thin-film microfabrication methods. The

second subsection highlights “unconventional” microfabrication strategies that employ magnetic powders for the realization of micromagnets.

#### **2.4.1 Conventionally Deposited Micromagnets**

Conventional deposition encompasses physical vapor deposition (sputtering, evaporation, pulsed-laser deposition (PLD)) and electrochemical deposition (electroplating). These wafer-level batch fabrication processes are familiar to the MEMS community and have enabled a large majority of the prior investigations into micromagnets. Table 2-2 summarizes many conventionally deposited magnets.

Of the various magnetic material categories, metal alloy magnets have been the most widely studied for potential integration in MEMS, primarily because of the favorable cost, simplicity, and process integration afforded by electrodeposition. The earliest efforts for integrating permanent magnetic materials for MEMS focused on Co–Ni–X alloys, where X is normally non-magnetic element such as P and W. These non-magnetic elements are usually very small in relative quantity but important. During electroplating, these elements tend to segregate at grain boundaries forming defects that inhibit domain walls from moving, hence increase the coercivity. However the resulting magnetic properties are usually fairly limited. The intrinsic coercivities are usually in the range of 30-200 kA/m, and the energy products are usually less than 10 kJ/m<sup>3</sup>. Despite this modest performance, these films are readily integrated into MEMS processes using straightforward electrodeposition methods.

Motivated by the successful application in magnetic recording area, deposition of ordered L1<sub>0</sub> CoPt and FePt films have also been investigated. L1<sub>0</sub> refers tetragonal distortion of an fcc structure, where atomic layers of Pt are sandwiched between Fe (or Co) layers. Relatively thick films can be deposited by electroplating [24]-[26], [29] or

sputtering [27], but high-temperature annealing (generally 400–800°C) is often required to induce the ordered  $L1_0$  structure. Intrinsic coercivities up to 1440 kA/m and energy products up to 124 kJ/m<sup>3</sup> has been achieved after annealing. Recently, Nakano et al. [28] reported an as-deposited Fe–Pt thick films with  $L1_0$  phase without intentionally heating substrate. The film was deposited by a high-power pulse laser deposition on an area of 5×5 mm<sup>2</sup>. An anisotropic property had been achieved with out-of-plane energy product up to 105 kJ/m<sup>3</sup>. For deposition, electroplating has been primarily explored, but thicknesses of the films have been less than 1 μm [24-26]. In contrast, multi-micron sputtered films have been reported by Liu with an energy product up to 124 kJ/m<sup>3</sup> [27].

Another metal alloy is the Co-rich Co–Pt system, where the Co content is approximately 80% [30]-[33]. This alloy was developed heavily by Zangari and Zana [30] and offers strong magnetic properties in the as-deposited state, i.e. without any high-temperature annealing. Strong out-of-plane magnetic anisotropy is achieved by aligning the c-axis of the Co crystalline perpendicular to the substrate and encouraging columnar microstructure with phosphorous-segregated grain boundaries. This process is enhanced by using textured seed layers, e.g. Cu (111) on Si (110), that provides a template lattice for the desired crystalline structure.

While great strides have been made with metal-alloy magnets, their properties are still much lower than that possible with rare-earth magnets. Thus, interest has steadily grown in integrating rare-earth magnetic materials. Since rare-earth magnets cannot be electroplated from aqueous baths, most efforts have employed sputtering or pulsed-laser deposition.

In the materials community, the magnetic properties of rare-earth thin films (<0.5  $\mu\text{m}$ ) have been shown to approach that of bulk magnets. Technical challenges such as control over stoichiometry, crystal structure, and microstructure have been overcome, and protection layers (to mitigate oxidation and corrosion) are readily deposited on top of the magnetic films. Unfortunately, less attention has been paid to thicker films and MEMS integration issues (patterning, batch fabrication, and deposition rate). Recently, however, investigations have begun focusing on increasing deposition rates and developing wafer-level deposition processes with specific intent for MEMS applications [35]-[44].

Prados et al. demonstrated fairly thin (0.5  $\mu\text{m}$ ) sputtered Sm–Co films with a very high intrinsic coercivity of 2080 kA/m after annealing at 550 °C [35]. Pina et al. fabricated a relative thicker (1.5  $\mu\text{m}$ ) films by sputtering Sm–Co onto a heated substrate and followed by annealing. Similar intrinsic coercivity had been achieved [37]. In order to avoid oxidation and also increase the thickness, Cadieu et al. [36] deposited nanophase SmCo into metal matrix. The final composite film had a thickness of 1  $\mu\text{m}$  and an intrinsic coercivity of 1200 kA/m. Recently, Budde and Gatzen [38] sputtered Sm–Co films at deposition rates of 2.9 nm/s up to 50  $\mu\text{m}$  in thickness. A maximum energy product of 90 kJ/m<sup>3</sup> was achieved after post-annealing at 560 °C. Patterning the thick films by ion beam etching and wet chemical etching was demonstrated on glass and Al<sub>2</sub>O<sub>3</sub>, but similar processes have not yet been achieved on Si substrates.

Nd–Fe–B has poor corrosion resistance so that the deposition of thick films is more difficult than other materials. Yamasawa et al. [40] reported an multi-layer structure with W layer in between Nd–Fe–B layers in order to prevent the Nd from

oxidation. Castaldi et al. [41] used Cu and Nb buffer and cap layers to obtain similar thickness of Nd–Fe–B films. Walther and Dempsey et al. [42] have developed a DC triode sputtering technique to produce 5  $\mu\text{m}$  of both Sm–Co and Nd–Fe–B thick films at deposition rates up to 5 nm/s. The films were patterned by filling pre-etched trenches in the substrate, followed by chemical-mechanical-planarization (CMP) in a Damascene-like process. Wet-etching has also proved suitable for Nd–Fe–B films [43]. The maximum energy product for the Nd–Fe–B films can be as high as  $400 \text{ kJ/m}^3$ , which is comparable to bulk rare-earth magnets.

Nakano et al. has demonstrated pulsed-laser-deposited Nd–Fe–B films up to 120  $\mu\text{m}$  in thickness [44]. This deposition method is very promising, but so far has been limited to fairly small surface areas.

In summary, the simple Co–Ni alloys are readily integrable, but fundamentally limited in performance. The better-performing Fe–Pt  $L_{10}$  alloys and rare-earth alloys require in situ or post-deposition annealing at high temperatures ( $>400^\circ\text{C}$ ) to achieve their high magnetic properties, so the thermal budget and temperature compatibility of other materials must be considered. The middle ground is occupied by the electroplated Co-rich Co–Pt alloys, which exhibit moderate performance in the as-deposited state.

Also, with the exception of the Co–Ni–Mn alloys, which have relatively low magnetic performance, most of the better performing sputtered or electroplated films are limited to a few microns in thickness. This is due to intrinsic stresses that develop during deposition and/or thermal mismatch stresses that arise during annealing steps. Also, the magnetic performance of a film tends to degrade with thickness due to variations in the microstructure, e.g. grain size and shape.

### 2.4.2 Powder Micromagnets

While the use of magnetic powders is ubiquitous for macroscale magnet fabrication, their use in microfabrication is certainly a foreign concept. The idea of intentionally introducing small powder particles into a “clean” environment is sure to raise eyebrows with cleanroom managers! Despite potential segregation/contamination issues, the magnetic properties of bulk-manufactured powder-based magnets are too attractive to overlook. If suitable integration methods can be developed, the complex, high-temperature materials processing steps required to achieve ideal magnetic properties can be delegated to the powder manufacturing, separate from the MEMS fabrication.

Additionally, the use of magnetic powders affords the opportunity to batch-fabricate magnets with thicknesses that are not technologically feasible with other standard microfabrication or bulk-manufacturing methods. As described previously, sputtered or electroplated magnets are often limited to a few microns in thickness, while bulk manufacturing techniques do not enable magnets much smaller than 1 mm. Thus, microscale powder processing methods may be well suited for magnets in the 10  $\mu\text{m}$  – 1 mm range.

Naturally, the magnetic particle size dictates the minimum magnetic feature size. The particles must be smaller than the desired feature size to ensure a quasi-homogenous distribution of particles. Commercially available hard ferrite powders are available down to  $\sim 2 \mu\text{m}$ , Sm–Co down to 5-10  $\mu\text{m}$ , and Nd–Fe–B down to  $\sim 50 \mu\text{m}$ . The minimum particle size is dependent on a combination of the microstructural grain size, the magnetic domain size, and thermal stability.

As summarized in Table 2-3, attempts have been made to incorporate magnetic microparticles into microfabrication processes in several ways. In one approach, coined magnetic composite electroplating (MCE) by Guan and Nelson [45]-[46], [56], non-soluble magnetic particles were incorporated into conventional magnetic alloy electroplating baths to create metal-particle composites. During deposition, the magnetic particles (e.g.  $\text{BaFe}_{12}\text{O}_{19}$ ) were mechanically and electrochemically captured into the growing electrodeposit. So far, this approach has achieved energy densities up to  $6\text{-}9\text{ kJ/m}^3$  for arrays of magnets  $15\text{-}50\text{ }\mu\text{m}$  thick using  $\text{BaFe}_{12}\text{O}_{19}$  particles in a Co–Ni–P matrix [46].

Other approaches emulate macroscale bonded magnet powder methods using polymers/resins/inks loaded with magnetic particles. These composites can be spin-coated, screen-printed, or “squeegeed” into cavities to form magnets with micron to millimeter scale features. Bonded micromagnets have been achieved using ferrite, Sm–Co, and Nd–Fe–B powders in epoxy [50], SU-8 [51], polyimide [47], PMMA [57], and resin binders [48], [50], [53]-[55]. Intrinsic coercivities up to  $900\text{ kA/m}$  and energy products of  $22\text{-}24\text{ kJ/ m}^3$  have been achieved.

As in bulk-manufactured bonded magnets, the final magnet properties are usually weaker than those of the original magnetic powder. The coercivity generally remains constant, but the remanence is proportional to the particle fill factor, typically  $60\text{--}80\%$  at best. This results in lower energy density. For higher fill factors, the magnet/particle mixtures are too viscous, so screen-printing and spin-casting are no longer feasible.

In an attempt to overcome this fill factor limitation, Bowers et al. [52] demonstrated dry-packing of raw  $\text{Sm}_2\text{Co}_{17}$  particles into Si trenches to form embedded micromagnets.

Magnets ranging in size from 15–500  $\mu\text{m}$  were achieved with energy densities up to 23  $\text{kJ}/\text{m}^3$ .

## 2.5 Conclusion

Technology development for fabrication and integration of permanent micromagnets has steadily advanced over the past decades. Ongoing interest in micromagnetic devices has spawned a variety of investigations on materials and methods for microfabricating thick, high-energy-product, permanent magnets for MEMS applications.

From a size scale perspective, conventionally deposited (sputtered, electroplated, PLD) micromagnets have demonstrated excellent magnetic performance, but are limited in thicknesses to  $\sim 100 \mu\text{m}$ . Powder-based fabrication methods appear to be filling a niche for magnets in the  $100 \mu\text{m} - 1 \text{ mm}$  size range, but their properties have been limited by the availability of magnetic powders and non-ideal fabrication strategies.

From a magnet property perspective, the best performing micromagnets have been achieved using rare-earth alloys. Unfortunately, the high performers are hampered by requirements for special substrates, high-temperature annealing, or other integration issues. The best performing sputtered Nd–Fe–B magnets have approached the theoretical performance limits currently known for magnetic materials. However, the requirement for high-temperature annealing and specialized deposition systems may preclude their widespread adoption. Where high temperatures are not permissible, Co-rich Co–Pt alloys offer good magnetic performance and are highly integrable via electrodeposition methods. Lastly, while powder-based micromagnets are relatively immature, there appears to be many opportunities for enhancing the processes and the magnetic properties, so these materials may become more prominent in time.

From an integration perspective, many of the superb magnetic properties described above were obtained under ideal conditions, without explicit consideration for integration into a MEMS device process. Examples of process incompatibilities include using high-pH electroplating solutions at elevated temperatures, which will dissolve standard photoresist masks; requiring non-standard substrate materials or specific crystalline orientations, which limits versatility; requiring in-situ or post-deposition heat treatments, which exceed temperature limits of other common MEMS materials; and lacking means for photolithographic patterning. Clearly, if these magnetic films are to be integrated into more complex micromachined MEMS transducers, these integration issues must be resolved.

Additionally, the process compatibility and long-term stability of these films with regard to pre- and post-deposition thermal cycling, chemical exposure, mechanical stress, etc. are largely unknown. Systematic characterization of long-term thermal and chemical stability is a fairly mundane research task, but of critical importance. The stability of any micromagnetic material must be well understood for application in any viable commercial end-product. In conclusion, while great strides have been made over the last decade to develop suitable permanent magnet materials, there are still many opportunities for advancements. As in bulk materials, there is no “silver bullet” process or material that can satisfy all performance needs for all applications. Magnetic materials and their application in MEMS remains an active and interesting area for research and development.

Table 2-1. Typical bulk hard magnet properties

Material	Category	Intrinsic Coercivity $H_{ci}$ [kA/m]	Remanence $B_r$ [T]	Energy Product $BH_{max}$ [kJ/m <sup>3</sup> ]	Curie Temp. $T_c$ [°C]	Max. Op. Temp. $T_{max}$ [°C]	Reversible Temp. Coeff. Remanence $\alpha$ [%/°C]	Corrosion Resistance
MO·6(Fe <sub>2</sub> O <sub>3</sub> ) [13]	Ferrite	200-380	0.2-0.4	8-30	450-470	200-300	-0.2	Excellent
Al-Ni-Co [13]	Metal Alloy	40-170	0.7-1.3	11-72	810-860	450-550	-0.02	Very good
CoPt – L <sub>10</sub> [13]	Metal Alloy	360		75	840			Very good
FePt – L <sub>10</sub> [13]	Metal Alloy	390		160	750			Very good
SmCo <sub>5</sub> [15]	Rare Earth	1300-2400	0.8-0.95	130-180	685-750	250-300	-0.04	Moderate
Sm <sub>2</sub> Co <sub>17</sub> [15]	Rare Earth	560-2100	1.0-1.2	190-240	750-970	300-350	-0.03	Moderate
Nd <sub>2</sub> Fe <sub>14</sub> B [15]	Rare Earth	880-3300	1.0-1.4	190-400	310	125-150	-0.1	Poor

Table 2-2. Conventionally microfabricated permanent magnets for MEMS.

Reference	Alloy	Fabrication Method	Integration Notes	Thickness [ $\mu\text{m}$ ]	Intrinsic Coercivity $H_{ci}$ [kA/m]	Remanance $B_r$ [T]	Energy Product $(BH)_{max}$ [ $\text{kJ/m}^3$ ]
Myung et al. [18]	CoNiP	Electrodeposited	None	2	75-170	--	--
Guan, Nelson [19]	CoNiP	Electrodeposited	None	1-52	55-105 <sup>a</sup>	0.06-0.1	1.3-1.8
Liakopoulos et al. [20]	CoNiMnP	Electrodeposited	None	10-45	70-100	0.2-0.3	14
Guan, Nelson [21]	CoNiMnP	Electrodeposited	None	2-40	30-180 <sup>a</sup>	0.01-0.1	0.3-2.6
Yufeng et al. [22]	CoNiMnP	Electrodeposited	0.2 T magnetic field	25	40-210	0.06-0.2	0.6-10
Ng et al. [23]	CoNiReWP	Electrodeposited	None	34-90	160-190	0.31-0.51	--
Rhen et al. [24]	FePt – L1 <sub>0</sub>	Electrodeposited	400°C anneal	0.45	240	--	--
Leistner et al. [25]	FePt – L1 <sub>0</sub>	Electrodeposited	600°C anneal	0.7	880	--	--
Thongmee et al. [26]	FePt – L1 <sub>0</sub>	Electrodeposited	400-800°C anneal	0.15-0.8	320-1440	--	--
Liu et al. [27]	FePt – L1 <sub>0</sub>	Sputtered	600°C anneal	6-7	446		124
Nakano et al. [28]	FePt– L1 <sub>0</sub>	PLD	small area	19-26	600	1.4	12-105
Berkh et al. [29]	CoPt– L1 <sub>0</sub>	Electrodeposited	700°C anneal	10-16	800	0.37	--
Myung et al. [18]	CoPtP	Electrodeposited	None	1	230	0.2-0.3	--
Franz et al. [30]	CoPtW(P)	Electrodeposited	None	5-20	50-195	0.2-0.5	--
Zana et al. [31]	CoPt(P)	Electrodeposited	(110) Si substrate	2	370	0.6	52
Vieux-Rochaz et al. [32]	CoPt(P)	Electrodeposited	1.2 T	5	225	--	--
Kulkarni, Roy [33]	CoPt(P)	Electrodeposited	None	1-6	120	--	--
Berkh et al. [34]	CoPt(P)	Electrodeposited	None	40	220	0.3	--
Prados et al. [36]	SmCo	Sputtered	550°C anneal	0.5	2080	--	--
Pina et al. [37]	SmCo	Sputtered	550°C anneal	1.5	2100	--	--
Cadieu et al. [38]	SmCo	PLD	550°C anneal;	1	1200	--	--
Budde, Gatzel [39]	SmCo	Sputtered	560°C anneal;	3-50	1200	0.7-0.75	75-90
Walther et al. [40]	SmCo	Sputtered	750°C anneal	5	1035	0.8	140
Yamasawa et al. [41]	NdFeB/W	Sputtered	450 °C deposition;	1	800	1	53
Castaldi et al. [42]	NdFeB	Sputtered	470°C deposition	1	500-800	0.4-1.5	130-150
Dempsey et al. [43]	NdFeB	Sputtered	500°C deposition,	5	1280	1.4	400
Nakano et al. [44]	NdFeB	PLD	750°C anneal; 650°C anneal;	120	1000	0.55	77

<sup>a</sup>Coercivity  $H_c$  values, not intrinsic coercivity  $H_{ci}$ .

Table 2-3. Powder-based permanent magnets for MEMS.

Reference	Magnetic Powder	Carrier Material	Fabrication Method	Thickness [ $\mu\text{m}$ ]	Intrinsic Coercivity $H_{ci}$ [kA/m]	Remanance $B_r$ [T]	Energy Product $(BH)_{max}$ [kJ/m <sup>3</sup> ]
Guan et al. [45]	BaFe <sub>12</sub> O <sub>19</sub>	Ni	MCE <sup>a</sup>	5	24-170 <sup>b</sup>	0.16-0.22	1-2
Guan et al. [45]	BaFe <sub>12</sub> O <sub>19</sub>	CoNiMnP	MCE	5	76-160 <sup>b</sup>	0.2-0.25	7-8
Guan, Nelson [46]	BaFe <sub>12</sub> O <sub>19</sub>	CoNiP	MCE	15-50	120-175	0.2-0.25	6-9
Lagorce, Allen [47]	SrFe <sub>12</sub> O <sub>19</sub>	Polyimide	Spin-casting	10-20	320	0.16-0.28	5-12
Yuan et al. [48]	SrFe <sub>12</sub> O <sub>19</sub>	Resin	Screen-printing	8-15	160-320	15-50 <sup>c</sup>	--
Cho, Ahn [49]	SrFe <sub>12</sub> O <sub>19</sub>	Epoxy resin	Squeegee	60-70	350-360	0.03	2-3
Rozenberg et al. [50]	SrFe <sub>12</sub> O <sub>19</sub>	Resin	Screen-printing	10-220	480	0.4	24
Dutoit et al. [51]	Sm <sub>2</sub> Co <sub>17</sub>	SU-8	Spin-casting	15	140-550	0.25-0.34	22
Bowers et al. [52]	Sm <sub>2</sub> Co <sub>17</sub>	none	Dry-packing	15-500	130-140	0.3-0.5	18-23
Pawlowski et al. [53]	Nd <sub>2</sub> Fe <sub>14</sub> B	Resin	Tape-casting	100-800	300-800	0.35-0.45	--
Pawlowski, Töpfer [54]	Nd <sub>2</sub> Fe <sub>14</sub> B	Resin	Screen-printing	10-50	300-900	0.2-0.4	--
Schwarzer et al. [55]	Nd <sub>2</sub> Fe <sub>14</sub> B	Resin	Screen-printing	10-50	800	0.4-0.5	--
Guan, Nelson [56]	Nd <sub>2</sub> Fe <sub>14</sub> B	NiP	MCE	5-20	50-190	0.24-0.35	2-3
Romero et al. [57]	Nd <sub>2</sub> Fe <sub>14</sub> B	PMMA	"Rain-dropping"	500	1090	0.25-0.7	--

<sup>a</sup> MCE = magnetic composite electroplating; <sup>b</sup> Coercivity  $H_c$  values, not intrinsic coercivity  $H_{ci}$ ; <sup>c</sup> Unit of J/(T·kg)

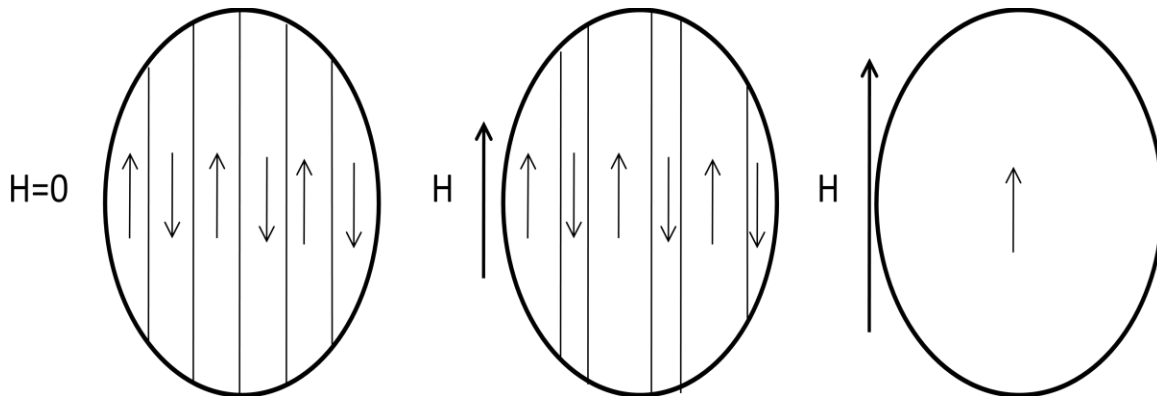


Figure 2-1. Schematic of the domain wall movements under a magnetic field.

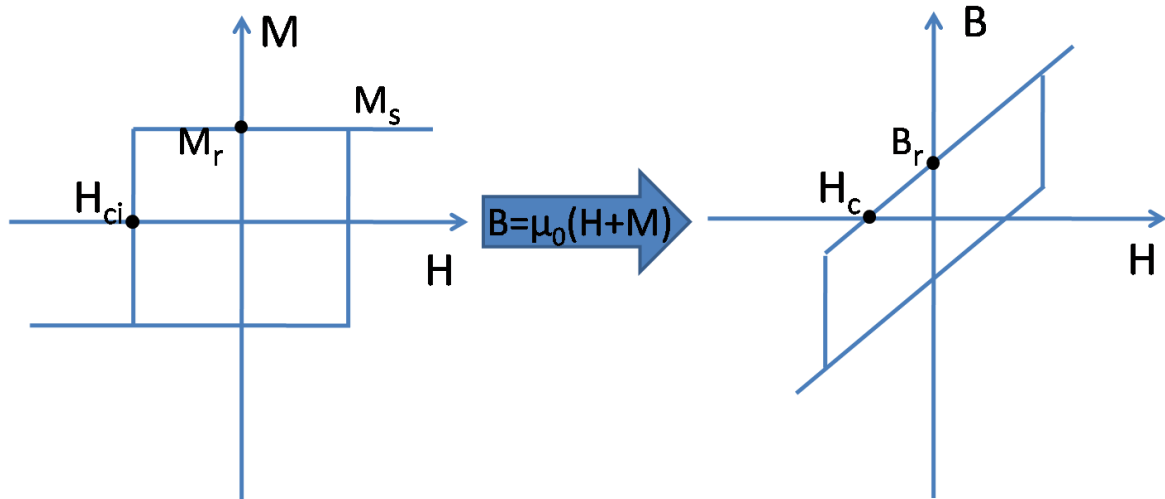


Figure 2-2. The two hysteresis loops of an ideal material: (a) magnetization loop; (b) induction loop.

## CHAPTER 3 ELECTROPLATING CO-RICH CO–PT MICROMAGNETS

Portions of this chapter are reproduced with permission from IEEE from the following article: N. Wang and D. P. Arnold, "Electroplated Co-rich Co–Pt thick films and patterned arrays for magnetic MEMS," *IEEE Trans. Magn.*, vol. 44, no. 1, pp 3969-3972, November 2008

As introduced in Chapter 2, electrodeposited Co-rich Co–Pt films with atomic ratios of 80:20 have been shown to exhibit large coercivities without any high-temperature processing steps. These films exhibit good magnetic properties in their as-deposited state due to the high magnetic anisotropy induced by the incorporation of Pt in the hexagonal close-packed (hcp) phase of Co. Furthermore, the use of textured seed layers of Cu (111) [58]-[59] or Ru (0001) [60]-[61] have been shown to induce a fine-grained columnar microstructure and a preferential orientation of the hcp c-axis perpendicular to the substrate. Moreover, higher electroplating current densities have been shown to eliminate the face-centered cubic (fcc) phase altogether, resulting in the preferred hcp phase only. These effects all contribute to perpendicular shape and crystalline anisotropy and hence enhanced out-of-plane magnetic properties.

Because of their high magnetic performance and entirely low-temperature process, these electroplated Co-rich Co–Pt films seem to be an ideal candidate to meet the needs for MEMS applications. However, the previously reported  $\text{Co}_{80}\text{Pt}_{20}$  films on textured seed layers were only up to 1-2  $\mu\text{m}$  in thickness. For films on Cu (111) seed layers, Zana et al. reported increasing perpendicular coercivities and squareness when the thickness increased from 100 nm to 1  $\mu\text{m}$ , which correlated with decreasing dispersion of the c-axis hcp phase [59]. The films showed intrinsic coercivity of 370 kA/m and remanance of 0.6 T. However, cracking was reported for films thicker than 1-2  $\mu\text{m}$  [59], indicative of high stress. For films on Ru (0001), Pattanaik et al. showed

marginally decreasing perpendicular coercivities and squareness when the film thickness increased from 25 nm to 2  $\mu\text{m}$ , which was attributed to limited grain coarsening [60]. An intrinsic coercivity of 280 kA/m was achieved on the 2  $\mu\text{m}$  films. These results indicate that thicker films on textured seed layers may be possible, but definitive results have not yet been reported.

In contrast, thicker ( $>2 \mu\text{m}$ ) Co-rich Co–Pt films have been investigated on untextured seed layers, but so far the magnetic performance has been fairly limited. Cavallotti et al. found a rapid decrease of coercivity from 320 kA/m to 160 kA/m when the film thickness grew larger than 2  $\mu\text{m}$  [62]. Kulkarni and Roy reported stress and cracking issues for multi-micron films, and despite attempts to use stress-relieving agents and pulse-reverse plating, coercivities up to only 120 kA/m were achieved for films in the 3–6  $\mu\text{m}$  range [33]. Similarly, Vieux-Rochaz et al. reported in-plane coercivities of only 100 kA/m for a 3.5  $\mu\text{m}$ -thick magnet [32]. Berk et al. achieved 220 kA/m out-of-plane coercivities for 27  $\mu\text{m}$ -thick Co–Pt–P films [34]. One reason for the limited performance of these thicker films is because of lack of good control of the electroplating bath and electroplating conditions in order to achieve microstructures with high anisotropy.

Based on these prior efforts, the goal of this chapter is to further investigate the magnetic properties of thick ( $\sim 10 \mu\text{m}$ ) Co-rich Co–Pt arrays electroplated on both untextured Cu and textured Cu (111) seed layers on crystalline Si substrates for their suitability for magnetic MEMS applications.

### **3.1 Electroplating Bath**

The aqueous electrolyte is amino-citrate-based. The original solution that has been widely used for Co–Pt electroplating was prepared by a complex, multi-step

process. For example, the constitutive Pt salt  $\text{Pt}(\text{NH}_3)_2(\text{NO}_2)_2$  (P-salt) and Co salt  $\text{Co}(\text{NH}_2\text{SO}_3)_2$  were independently synthesized by slow and complex chemical reactions before mixing together to form the plating bath. The reason is that a fresh chemical mixing was reported as very important to achieve a successful deposition. During this complex process, however, unexpected solid precipitates often occurred. If a precipitation happened, the whole process had to be started from beginning. In addition, in order to obtain good results, a large quantity of plating bath (1 liter) was usually prepared, even for plating on a small sample. Additionally, the shelf life of the bath was typically relatively short, only one or two weeks. Considering the high cost of both Pt and Co salts, these complex processes and unstable baths are undesirable, especially for use in a MEMS process flow, which requires high repeatability.

In order to solve some of the aforementioned problems, some changes on the plating bath are made in this work. Table 3-1 summarizes two slightly different bath recipes that were tailored for deposition on un-textured and textured (111) Cu seed layers, respectively. First, commercially available chemicals were used, instead of complex chemical reactions. For example, the P-salt used in this work was a pre-made solution, composed of 3.4 wt% p-salt and 96.6 wt% ammonia. The cobalt (II) sulfamate,  $\text{Co}(\text{NH}_2\text{SO}_3)_2 \cdot 2(\text{H}_2\text{O})$  was purchased in solid crystal form. However, these chemicals could not mixed directly with each other, otherwise precipitation would occur due to the instability of the p-salt. Therefore, sulfamic acid ( $\text{H}_3\text{NSO}_3$ ) was added before the cobalt in order to stabilize the p-salt and prevent it from reacting with other chemicals, e.g. precipitation. Then the rest of chemicals listed in Table 3-1 were added. The solution was continuously stirred to achieve a uniform and transparent solution. Among the rest

of chemicals, sodium hypophosphite ( $\text{NaH}_2\text{PO}_2 \cdot \text{H}_2\text{O}$ ) was used as a source of phosphorus, which deposits at the grain boundary to isolate the grains and hence improve the coercivity of the magnetic films. Glycine ( $\text{NH}_2\text{CH}_2\text{COOH}$ ) and saccharin ( $\text{C}_7\text{H}_5\text{NO}_3\text{S}$ ) were used to mitigate stress in the plated films. When all the chemicals were mixed to a stable bath, the electrolyte had a pH of  $\sim 2$ . The final step was to adjust the pH of the electroplating bath to 8.5 or 9 (depending on the recipe) by adding sodium hydroxide (NaOH) pellets. With this recipe, the plating bath was found to be stable for months.

### 3.2 Fabrication Process

The Co–Pt alloys were deposited into photolithographically defined photoresist molds on Cu-coated silicon substrates. Two different types of substrates were prepared: Cu on (100) Si wafers and textured (111) Cu on (110) Si wafers. The substrate fabrication process is described here.

The first step was deposition of the Cu seed layers. In order to obtain the textured (111) Cu, an H-terminated Si surface was created by dipping the Si (110) substrate in a 10% HF acid solution for 3 minutes just prior to sputtering. No special treatment was performed on the standard (100) silicon substrates with the expectation that the native oxide. Cu seed layers of 100 nm thickness were then sputtered by DC magnetron sputtering. The details of the sputtering method can be found in [63]. After reaching a base pressure of  $10^{-6}$  Torr, the sputtering power on a 2-inch target was 300 W under Ar at 5 mTorr with no intentional substrate heating.

Figure 3-1 shows the resulting  $\theta$ - $2\theta$  x-ray diffraction (XRD) spectrum of the two different substrates. An un-textured polycrystalline Cu seed layer was formed on the standard Si (100) wafer for which the native oxide had not been removed. This is

evident in Figure 3-1A by the (200) and (400) peaks for Si along with (111) and (200) peaks for Cu. In contrast, a textured Cu (111) seed layer was formed on H-terminated Si (110). Figure 3-1B shows a Si (220) diffraction peak and a Cu (111) diffraction peak. Note that a few other small peaks appear in both spectrums. These small peaks do not belong to pure Cu or Si, and are potentially caused by some intermediate phases such as copper silicide.

The corresponding rocking curve on the Cu (111) peak of the textured seed layer is shown in Figure 3-2A, indicating a full-width, half-maximum (FWHM) angle of only  $0.78^\circ$ . The rocking curve is not symmetric, indicating non-uniformity in the structure, for example a double-layer structure with one well-aligned layer and another layer that is not as well aligned. Furthermore, Figure 4-2 B shows the pole figure for the textured Cu film deposited on Si (110) indicating a clear (111) texture with twin orientations. The results confirm that nearly epitaxial Cu (111) films were deposited on the Si. The epitaxial orientation is Cu(111)/Si(110) with Cu[1-10]//Si[001] for the A orientation, and Cu[-110]//Si[001] for the B orientation [63].

After the seed layer preparation, AZ-4620 photoresist mask patterns were defined by conventional photolithographic techniques. The mask pattern contained arrays of square apertures of  $150\ \mu\text{m} \times 150\ \mu\text{m}$ . The Co-rich Co–Pt alloys were then electroplated into the defined mask. The processing steps are shown in Figure 3-4.

The samples were electroplated galvanostatically in a 200 mL bath with no agitation using a Co anode. It was found that, in order to obtain optimal magnetic properties, different bath chemistries and plating conditions were required for the two different seed layers. Additionally, the current density and bath pH were found to

significantly impact the composition, deposition rates, and ultimately the magnetic properties. Therefore, different sets of parameters were used for the two different seed layers, as summarized in Table 3-1. The current density, pH, and molar ratio of the Co- and Pt-salts differ slightly from those previously reported in [58]-[61]. To maintain consistency for long plating durations, the pH was continuously monitored and adjusted using sodium hydroxide. In addition, the anode was cleaned every 15 min.

After electroplating, the photoresist molds were removed in a solvent bath, and the resulting magnets were analyzed. The microstructure was characterized by scanning electron microscopy (SEM JEOL JSM-6400). The chemical composition of Co–Pt films was measured by energy dispersive X-ray spectrometry (EDS). The film thickness was measured using a stylus profilometer (Dektak). The in-plane and out-of-plane (perpendicular) hysteresis loops were characterized by a vibrating sample magnetometer (ADE Technologies, EV9) with fields up to 2000 kA/m (25 kOe).

### **3.3 Experiment Results and Discussion**

After 90 min of electroplating, magnet arrays with thickness of 8 and 10  $\mu\text{m}$  were successfully fabricated on un-textured Cu and textured Cu (111) seed layers, respectively. Figure 3-5a shows SEM images of Co–Pt micromagnet arrays electroplated on the un-textured Cu seed layer where each magnet is 150  $\mu\text{m}$  x 150  $\mu\text{m}$  x 8  $\mu\text{m}$ . The magnets were well patterned with relatively flat surfaces. As shown in Figure 3-4 b, the cross-sections show that the films grew columnar through the whole thickness due to the high current density applied during electroplating. From EDS analysis, the Co:Pt ratio was determined to be approximately 80:20, which is in agreement with the reported values under similar electroplating conditions [59].

Figure 3-6 shows the corresponding in-plane and out-of-plane hysteresis loops. The out-of-plane coercivity is 260 kA/m (3.3 kOe), much higher than in-plane coercivity of 130 kA/m (1.6 kOe). In order to compare the in-plane and out-of-plane magnetization, demagnetization correction was performed on the out-of-plane data using the slope compensation method by increasing the slope of the loop until the line at saturation region remain flat [9]. The extracted out-of-plane demagnetization factor was about 0.55, which accounts for sample shape, grain shape, and roughness of the magnetic film [64].

Figure 3-7 shows SEM images of Co–Pt micromagnet arrays electroplated on the textured Cu (111) seed layer where each magnet is 150  $\mu\text{m}$  x 150  $\mu\text{m}$  x 10  $\mu\text{m}$ . The magnets show a microstructure similar to those deposited on the un-textured Cu seed layers, with well-defined square shapes, flat surfaces and columnar growth grains. EDS analysis also confirmed a Co:Pt ratio of about 80:20.

Figure 3-8 shows the corresponding in-plane and out-of-plane hysteresis loops. Here, the magnet arrays electroplated on the textured Cu seed layers show a significant enhancement of magnetic properties. The out-of-plane coercivity is 330 kA/m (4.1 kOe), and the in-plane coercivity is similar at 320 kA/m (4.0 kOe). After demagnetization correction of the out-of-plane data using a demagnetization factor of 0.51, the hysteresis loop indicates a squareness of 0.77. The remanant magnetization of the out-of-plane is 0.91 T compared to 0.46 T for the in-plane direction. It is clear from the data that the easy axis of the magnetization is in the out-of-plane direction. Moreover, these results indicate that an enhanced anisotropy is induced by the textured seed layer. It is believed that this anisotropy is not just the shape anisotropy induced by the columnar

grain growth, but also a crystalline anisotropy induced by an hcp phase that grows along the c-axis. The c-axis growth propagated so well during the deposition that even with film thicknesses up to 10  $\mu\text{m}$ , the out-of-plane easy axis could be maintained.

A summary of the measured magnetic properties of the micromagnet arrays is shown in Table 3-2. The data indicates a maximum energy product (demag corrected) for the magnet arrays electroplated on un-textured and textured seed layers of 23  $\text{kJ/m}^3$  and 69  $\text{kJ/m}^3$ , respectively. For completeness, demag corrected and uncorrected values are included for the out-of-plane data.

### **3.4 Conclusion**

In conclusion, strong magnetic properties were maintained for these thick patterned films using optimized electroplating conditions. The perpendicular coercivity, remanance, and maximum energy product reached as high as 330  $\text{kA/m}$ , 1.0 T, and 69  $\text{kJ/m}^3$ , respectively, for magnets on textured Cu (111) seed layers on Si (110). These properties are significantly better than previously reported  $\text{Co}_{80}\text{Pt}_{20}$  magnets of similar thickness on un-textured seed layers and indicate that strong perpendicular magnetic anisotropy induced by textured seed layers can be extended to at least 10  $\mu\text{m}$ . For magnets on un-textured seed layers on standard Si (100), 260  $\text{kA/m}$ , 0.54 T, and 27  $\text{kJ/m}^3$  were obtained. These properties are also higher than similar sized previously reported electroplated magnets listed in Table 2-2. It should be noted that the film thicknesses reported here were primarily limited by degradation and peeling of the photoresist masks when subjected to the alkaline plating bath for long durations. In summary, the high performance and entirely low-temperature fabrication process makes these permanent magnetic arrays well suited for integration in magnetic MEMS applications.

Table 3-1. Electroplating conditions for Co–Pt magnets.

Parameters	Un-textured Cu seed layer	Textured Cu (111) seed layer
Diamminedinitritoplatinium-- $\text{Pt}(\text{NO}_2)_2(\text{NH}_3)_2$	0.01 M	0.03 M
Sulfamic acid-- $\text{H}_3\text{NSO}_3$	0.1 M	0.1 M
Cobalt(II) Sulfamate-- $\text{Co}(\text{NH}_2\text{SO}_3)_2$	0.15 M	0.15 M
Ammonium citrate-- $(\text{NH}_4)_2\text{C}_6\text{H}_6\text{O}_7$	0.1 M	0.1 M
Sodium hypophosphite-- $\text{NaH}_2\text{PO}_2 \cdot \text{H}_2\text{O}$	0.1 M	0.1 M
Glycine-- $\text{NH}_2\text{CH}_2\text{COOH}$	0.1 M	0.1 M
Current Density	30 mA/cm <sup>2</sup>	70 mA/cm <sup>2</sup>
Temperature	65 °C	65 °C
pH	8.5	9

Table 3-2. Magnetic properties of Co–Pt micromagnet arrays.

Seed Layer	Orientation	H <sub>c</sub> (kA/m)	B <sub>r</sub> (T)	(BH) <sub>max</sub> (kJ/m <sup>3</sup> )			Squareness	
Un-textured Cu	Out-of-plane	260	0.29	0.51*	8.8	23*	0.26	0.46*
	In-plane	130	0.47		16		0.41	
Textured Cu (111)	Out-of-plane	330	0.47	0.91*	21	64*	0.40	0.77*
	In-plane	320	0.36		15		0.30	

\* Values after demagnetization correction

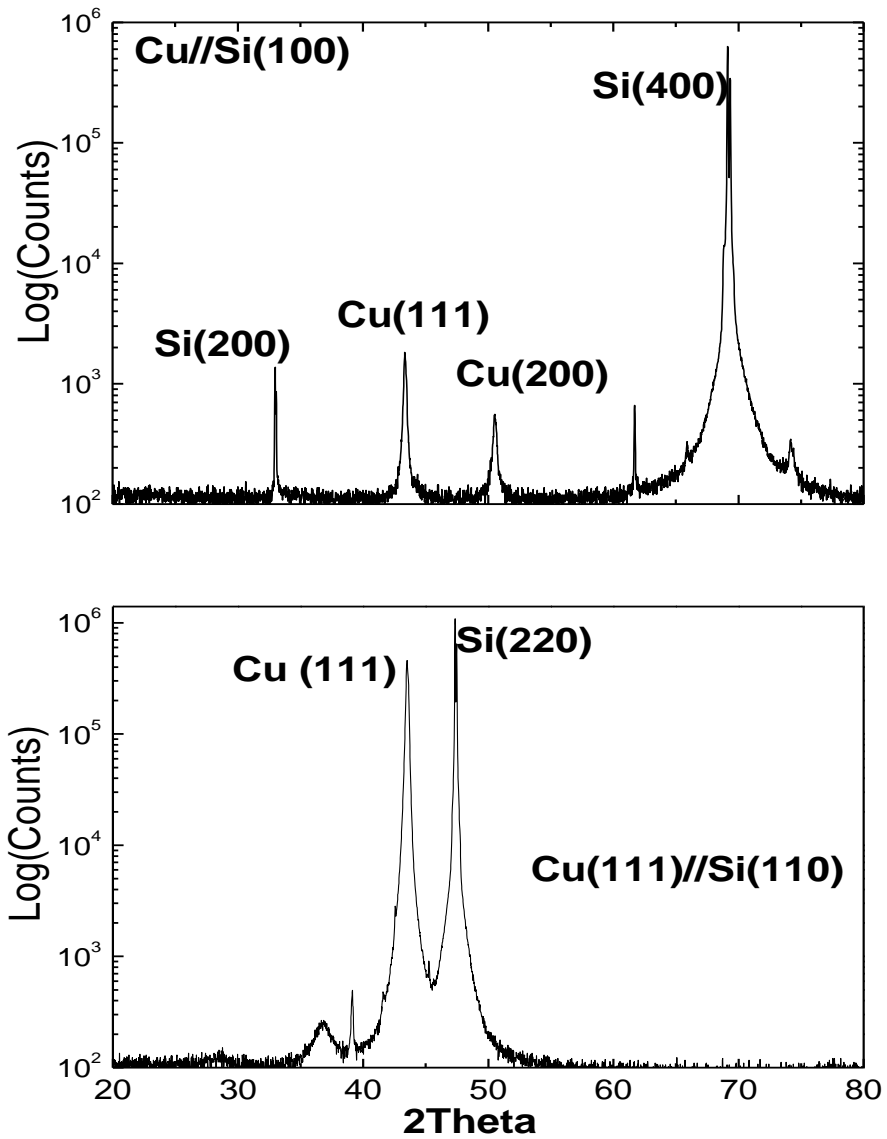


Figure 3-1. XRD patterns of (a) un-textured Cu on Si (100) and (b) textured Cu (111) seed layer on H-terminated Si (110) wafer.

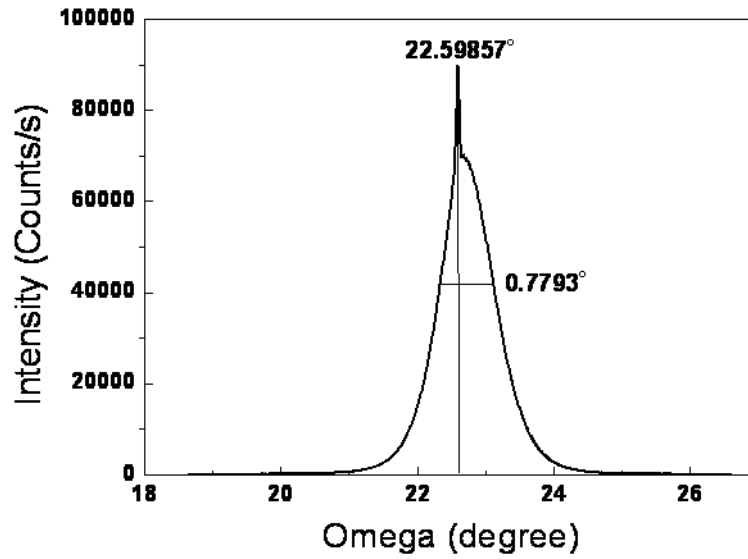


Figure 3-2. Rocking curve around Cu (111) peak of textured seed layer.

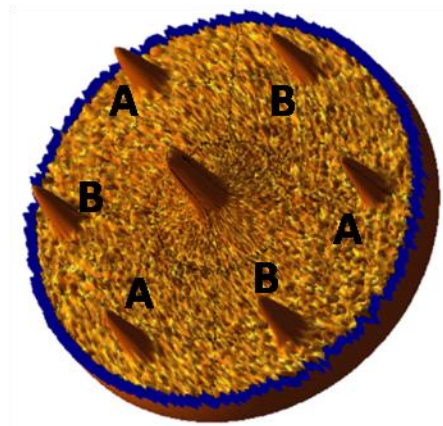


Figure 3-3. Pole figure of textured Cu (111) seed layer.

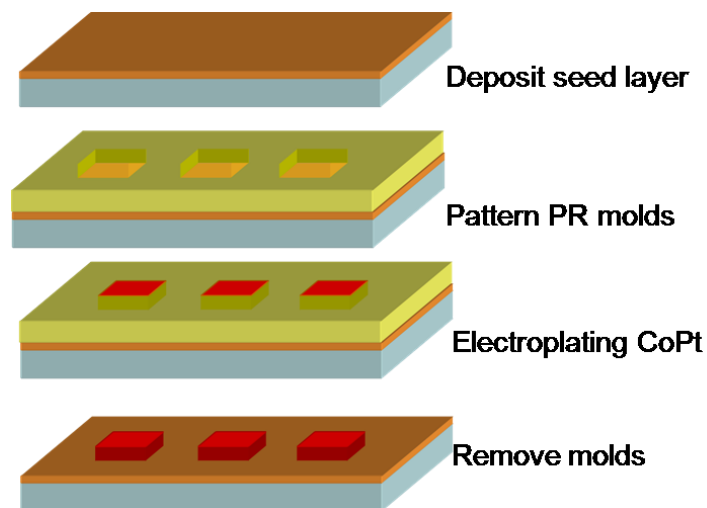


Figure 3-4. Schematic of process flow.

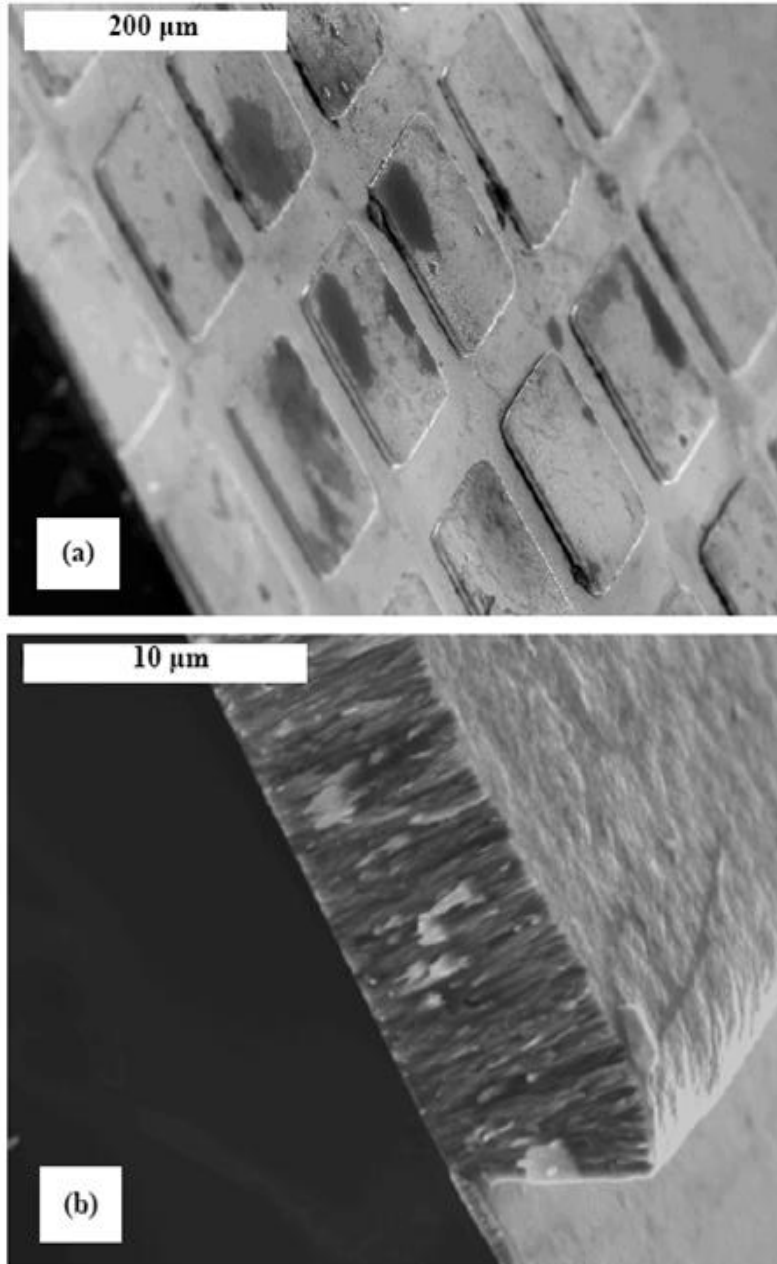


Figure 3-5. SEM images of 150 μm x 150 μm x 8 μm Co–Pt micromagnets on an untextured Cu seed layer, (a) micromagnet arrays and (b) the corresponding cross-section.

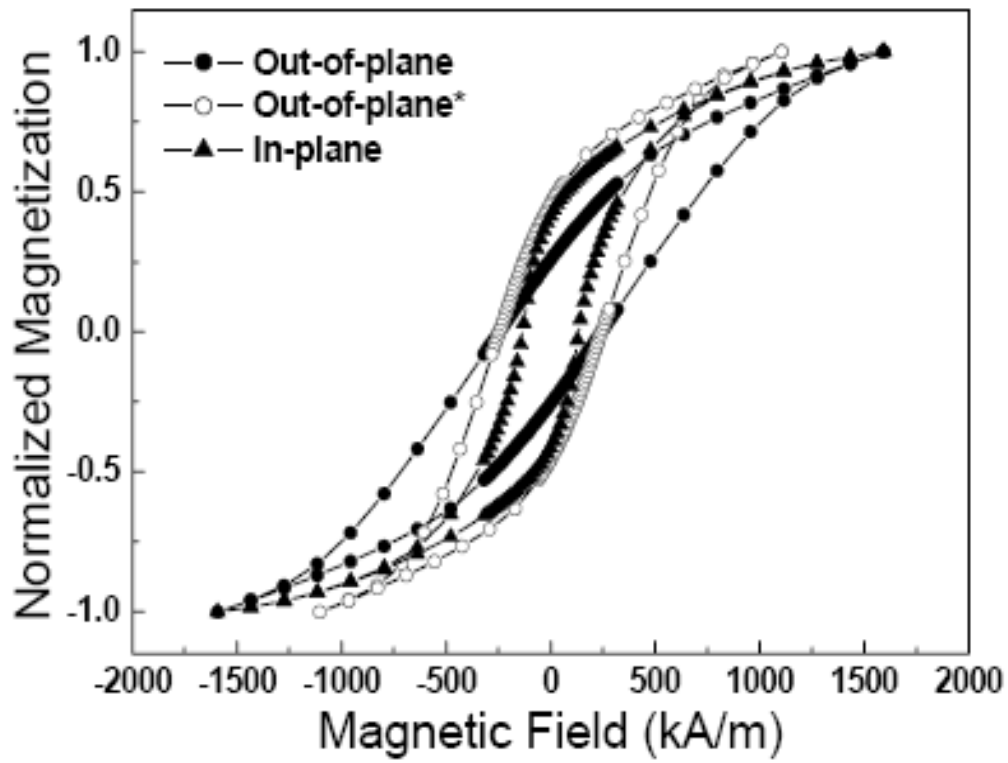


Figure 3-6. Hysteresis loops of Co–Pt micromagnet arrays on un-textured Cu seed layers. \*Hysteresis loop after demagnetization correction.

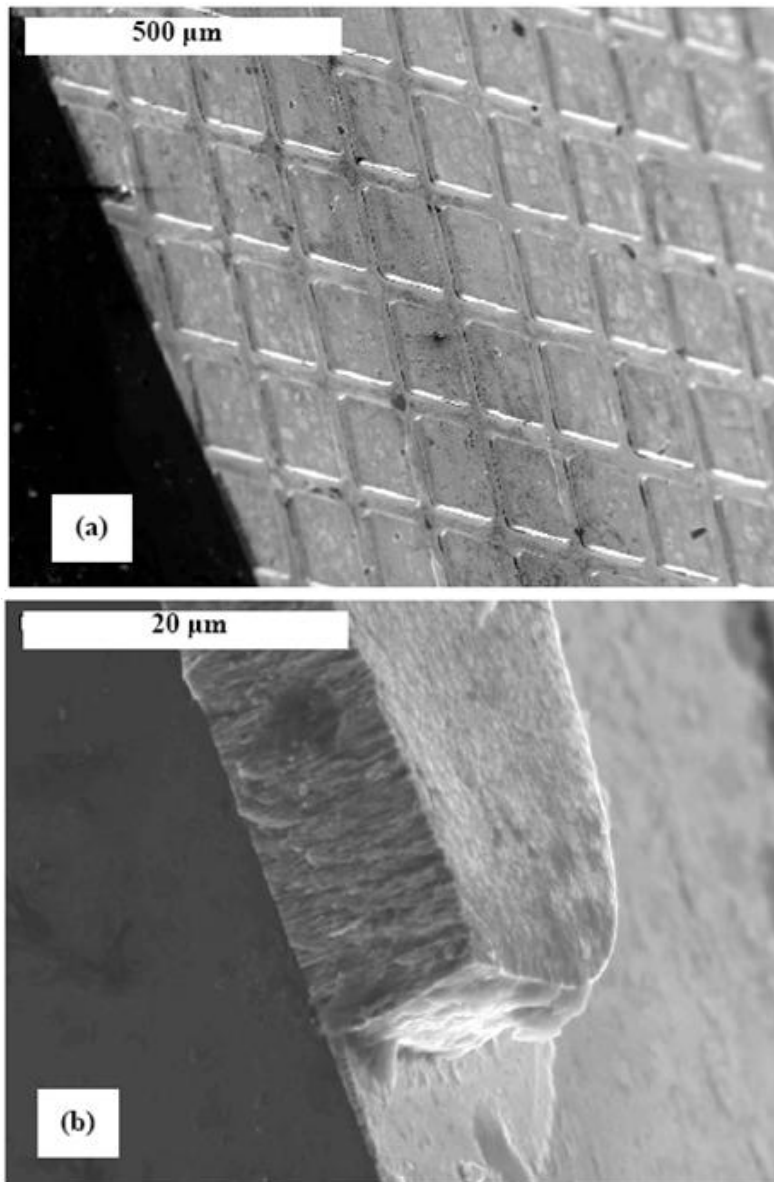


Figure 3-7. SEM images of 150  $\mu\text{m}$  x 150  $\mu\text{m}$  x 10  $\mu\text{m}$  Co–Pt micromagnets on a textured Cu (111) seed layer, (a) micromagnet array and (b) the corresponding cross-section.

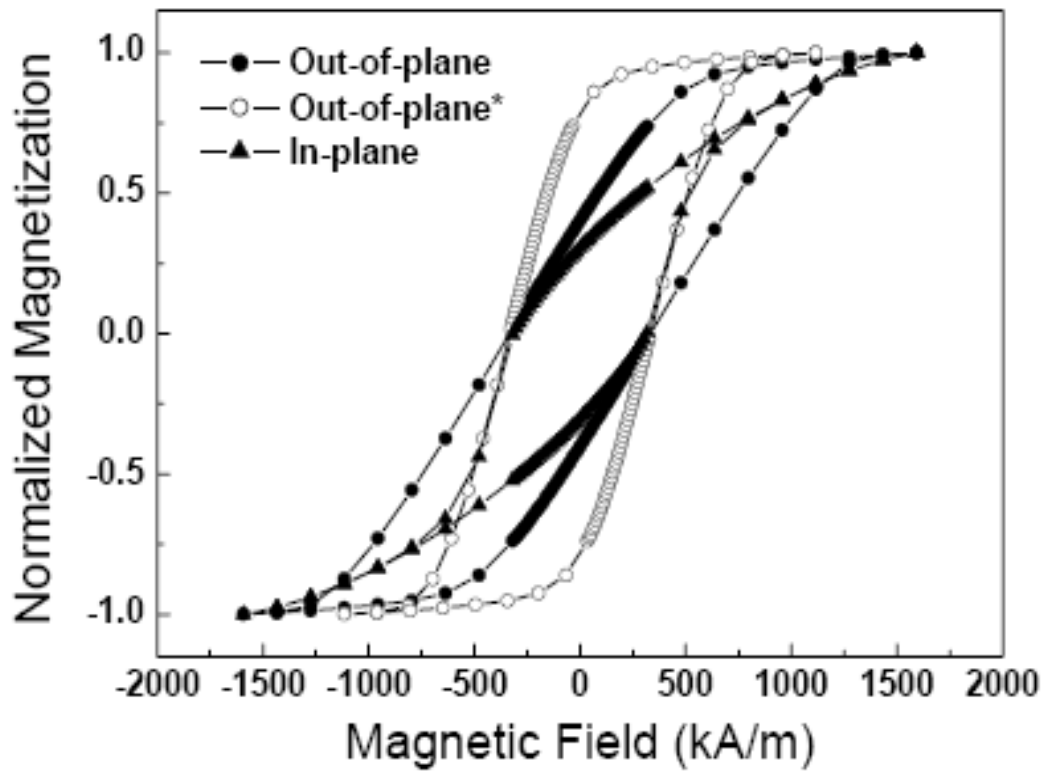


Figure 3-8. Hysteresis loops of Co–Pt micromagnet arrays on textured Cu (111) seed layers. \*Hysteresis loop after demagnetization correction.

## CHAPTER 4 MICROPACKING WAX-BONDED ND–FE–B MICROMAGNETS

Portions of this chapter are reproduced with permission from American Institute of Physics from the following article: N. Wang, B. J. Bower and D. P. Arnold, "Wax-bonded NdFeB micromagnets for MEMS applications," *J. Appl. Phys.* vol.103, pp. 07E109-1-3, April 2008.

Since magnetic force depends on magnetic volume (e.g. see equation (1-9)), many microscale magnetic devices require the development of relatively voluminous permanent magnetic structures in order to produce strong force. In Chapter 2, it was discussed that conventional microfabrication techniques such as electrodeposition and sputtering are usually limited to film thicknesses of a few microns because of film stresses and slow deposition rates. Powder magnets have the ability to achieve high thickness, but the properties are often limited by the raw powder or fill factor. In this chapter, a microfabrication technique is reported for the fabrication of wax-bonded micromagnets intended for the 100  $\mu\text{m}$  to mm range. This dimensional size is not typically achievable by thin-film deposition techniques or by conventional macroscale magnet processing, and is of interest for magnetic MEMS applications.

### 4.1 Fabrication Process

The rare-earth Nd–Fe–B magnetic powder used in the fabrication of micromagnets is an isotropic powder supplied by Magnequench Inc. (MQP-S-11-9). Unlike most other commercially available Nd–Fe–B powders, this powder has high corrosion resistance, which is highly desired for MEMS processing. However, it has only mediocre magnetic properties ( $B_r=0.73\text{-}0.76$  T,  $H_{ci}=670\text{-}750$  kA/m and  $(BH)_{\text{max}}=80\text{-}92$  kJ/m<sup>3</sup>) [65], which is a tradeoff for this application. Ideally, powder with good corrosion resistance and better magnetic properties would be desired. Another advantage of this powder is that the particles have fine, spherical shape, as shown in the SEM image of Figure 4-1-A. The

particles have distributed size and an average diameter of about 50  $\mu\text{m}$ . Compared to most other Nd–Fe–B powders—which are flake shaped and have average diameters of 200–300  $\mu\text{m}$ —the morphology of the particles makes the packing process much easier.

The binder wax, supplied by South Bay Technology Inc. (MWH080), has a melting temperature of 80  $^{\circ}\text{C}$ . The wax was crushed to a coarse powder, followed by 24 hours of ball milling to obtain fine particles. After milling, the wax powder has an average diameter about 5  $\mu\text{m}$ , as shown in Figure 4-1-B. The magnetic powder was homogeneously mixed with various wax powder in a glass mortar with loading fractions from 2 wt% to 15 wt%. The mixture was then dry-packed at room temperature into pre-etched rectangular cavities (500  $\mu\text{m}$  x 500  $\mu\text{m}$  laterally; 320  $\mu\text{m}$  deep) in a silicon wafer with compression by wiping a flat edge across the wafer leaving only powder in the trenches. After packing, the whole silicon wafer was heated on a hotplate at 90  $^{\circ}\text{C}$  for 30 second and then cooled down in air, allowing the wax to melt and bond the magnetic particles. Finally, the wafer surface was cleaned by de-ionized water and blown dry with nitrogen.

A typical magnet array after microfabrication is shown in Figure 4-2. Figure 4-3-A is a SEM picture of a surface of a magnet with 6.25 wt% wax loading. It shows that the wax was well melted and distributed homogeneously between magnetic particles. Figure 4-3-B shows an image of a magnet that is cleaved along an edge. It is shown that the powder completely fills the cavity, and no obvious shrinkage is observed.

For characterization, the wafer was placed in a pulse magnetizer and magnetized in the in-plane direction using a pulsed magnetic field of  $\sim 3$  T. Individual micromagnets were then diced from the processed wafer, and the magnetic properties were measured

by a vibrating sample magnetometer (ADE Technologies, EV9 VSM). Note that the wax bonding seemed rather strong, as the magnets survived the cleaning, dicing and magnetizing processes without any additional protection procedures.

## 4.2 Experiment Results and Discussion

Figure 4-4 shows the 2<sup>nd</sup>-quadrant demagnetization curves of wax-bonded micromagnets with different wax powder loadings. The micromagnets all have the same dimensions of 500  $\mu\text{m}$  x 500  $\mu\text{m}$  x 320  $\mu\text{m}$ . The demagnetization curves were measured by applying the field in-plane (along the 500  $\mu\text{m}$  length), and no corrections for demagnetization were performed. For comparison, the demagnetization curve of the raw Nb-Fe-B powder packed (without wax) tightly into a cylindrical capsule is also shown. The results show that, even tightly packed, the raw magnetic powder exhibits a relatively low coercivity of 280 kA/m, compared to the vendor-supplied “data sheet” value of 721 kA/m. This low coercivity suggests free motion of the particles under the applied external field.

However, when a small amount of wax powder is introduced into magnetic powder, the resulting composite exhibits strong enhancement of coercivity up to 737 kA/m, close to the expected value. This enhancement appears for all of the wax-bonded micromagnets with the wax loading from 2 to 15 wt%. However, with increasing amounts of wax, the remanant magnetization decreases due to the dilution of net magnetic moment. This dilution effect is not significant when the wax loading is below 6.25%, because the wax particles are so small compared to the magnetic particles. For low wax fractions, the wax particles tend to fill the spaces between the magnetic particles. However, for wax loadings greater than 6.25 wt%, there are no more voids

left, and the wax particles tend to displace the magnetic particles, thereby reducing the net volumetric magnetic moment.

Furthermore, it is interesting to see that there are kinks on the demagnetization curves when the magnetic field reached to -100 kA/m, and this effect is more pronounced when the wax loading is small (<6.35%). These kinks are attributed to the smaller magnetic particles, as seen in Figure 1a, which may not be sufficiently “locked” in place by the wax. For example, a smaller particle may sit in “pocket” formed by larger surrounding particles and may lack the necessary amount of wax to be bonded in place. Under an external field, these poorly bonded smaller particles would rotate more readily than the larger particles.

Figure 4-5 shows the energy product and coercivity as a function of the wax weight percentage. The data shows an optimum wax loading condition at 6.25%. Below this value, the motion of un-bonded particles causes a decrease in the energy product, while above this value; the dilution of the magnetic moment by the binder wax also decreases the energy product. These two mechanisms compete with each other to yield an optimum point. In addition, the results indicate that the coercivity is substantially improved when a small amount of wax is introduced and fairly constant for all weight fractions tested.

### **4.3 Conclusion**

In summary, a technique was developed for the fabrication of wax-bonded micromagnets with feature sizes of 100 $\mu$ m - 1 mm. The incorporation of the wax binder is shown to greatly improve the micromagnet coercivity over the raw dry-packed powder without bonding media (from 287 to 737 kA/m). Using this method, 500  $\mu$ m x 500  $\mu$ m x 320  $\mu$ m magnets were demonstrated with a maximum energy product of 16.6 kJ/m<sup>3</sup>.

Compared to other powder-based micromagnets listed in Table 2-3, these wax-bonded micromagnets are among the best in magnetic performance. Moreover, the whole packing process is simple, fast, repeatable, and easy to integrate with other processing steps.

In addition, this approach can be also applied to other magnetic powders, and naturally the smallest magnet dimension is limited by the power size. For integration of these micromagnets into wafer-scale fabrication processes, the wax used in this study exhibits too low of a melting point (80 °C), which is lower than the baking temperature of commonly used photoresist (90–120 °C). To avoid melting of the wax during these types of process steps, a higher melting-point wax may be used. For example, a wax with a melting temperature of 180 °C is used in the fabrication of devices described in Chapter 5. Also, to enable smaller magnets, Magnequench Inc. recently developed a new isotropic Nd–Fe–B powder with a smaller particle size (5–6 $\mu$ m), which could be used to realize micromagnets of less than 100  $\mu$ m in size.

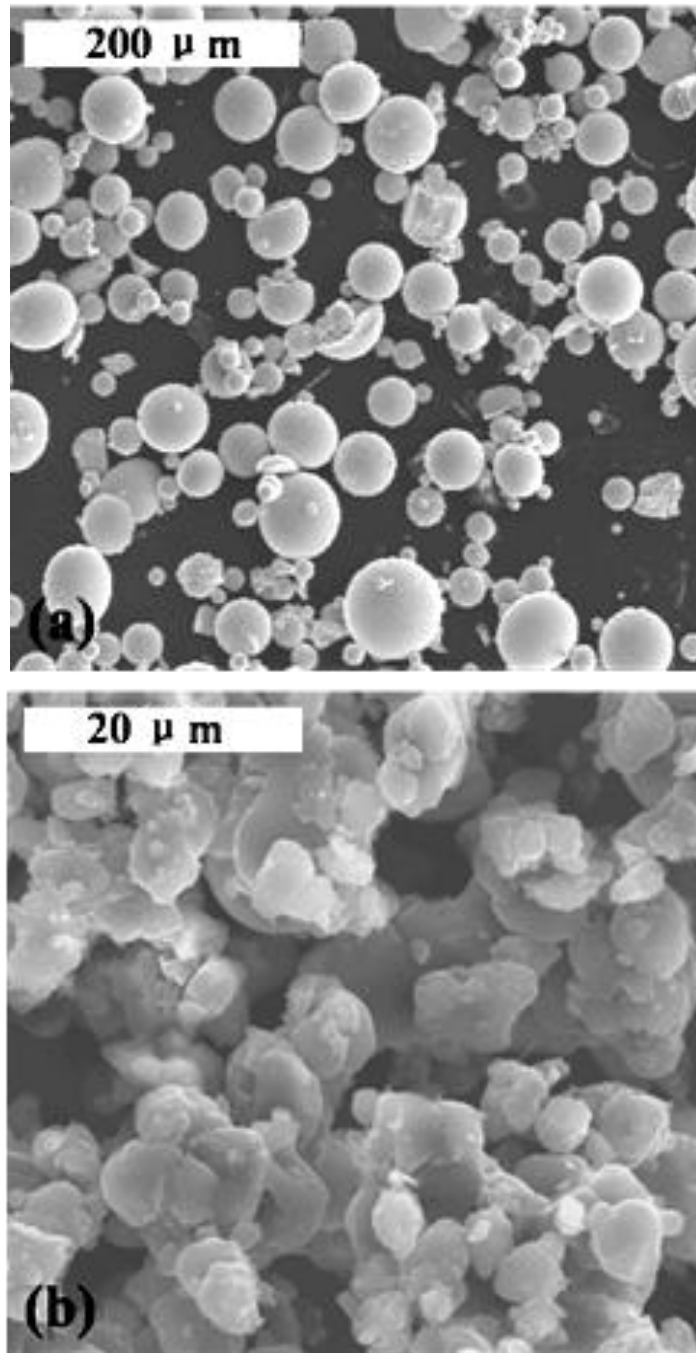


Figure 4-1. SEM image of a) raw Nd-Fe-B powder and b) wax powder after ball-milling for 24 hours.

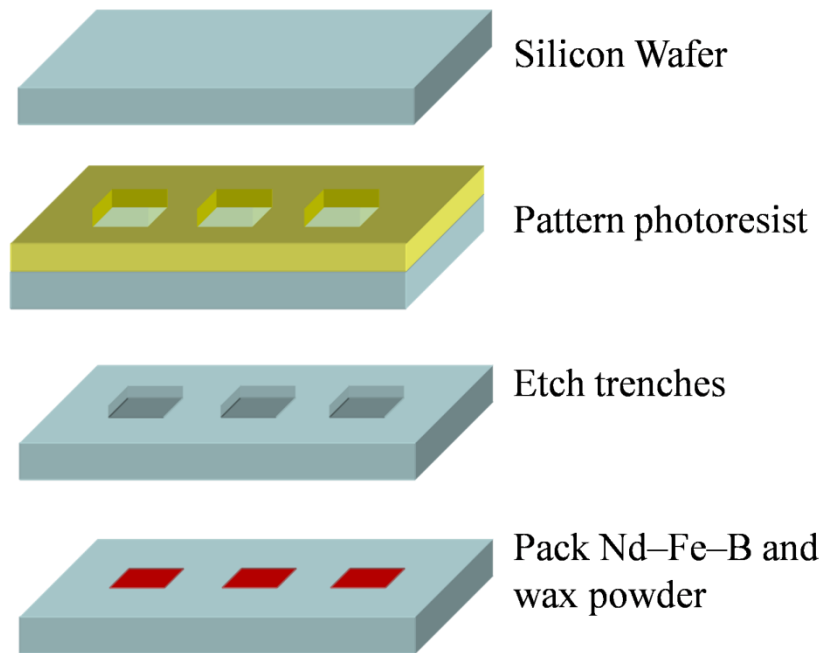


Figure 4-2. Schematic of the process flow.

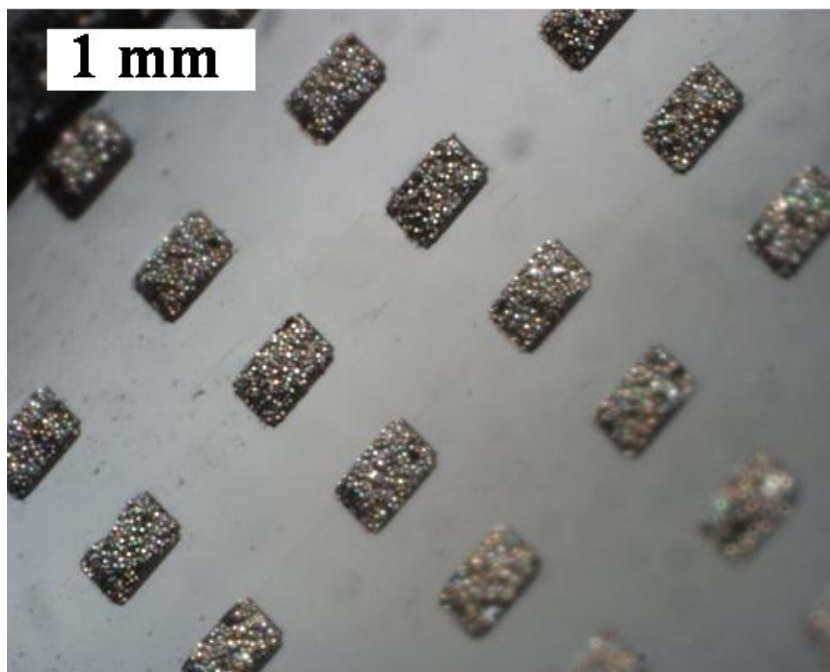


Figure 4-3. Photograph of a Nd-Fe-B micromagnet array where each magnet is  $500\ \mu\text{m} \times 500\ \mu\text{m}$  in lateral dimension and  $320\ \mu\text{m}$  thick.

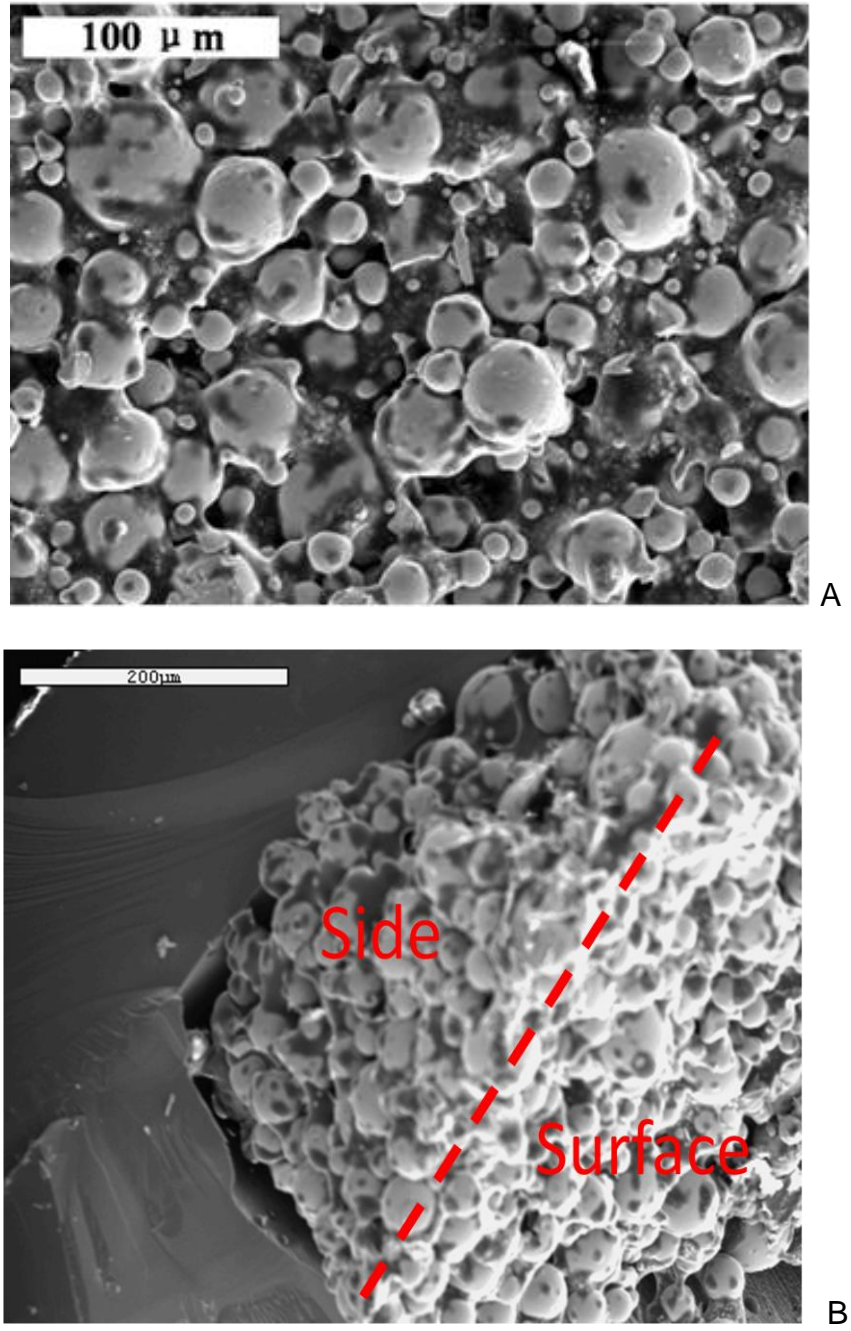


Figure 4-4. SEM image of wax-bonded Nd-Fe-B magnet with 6.25 wt% of wax loading  
A) top view of surface and B) oblique view sample cleaved along one edge.

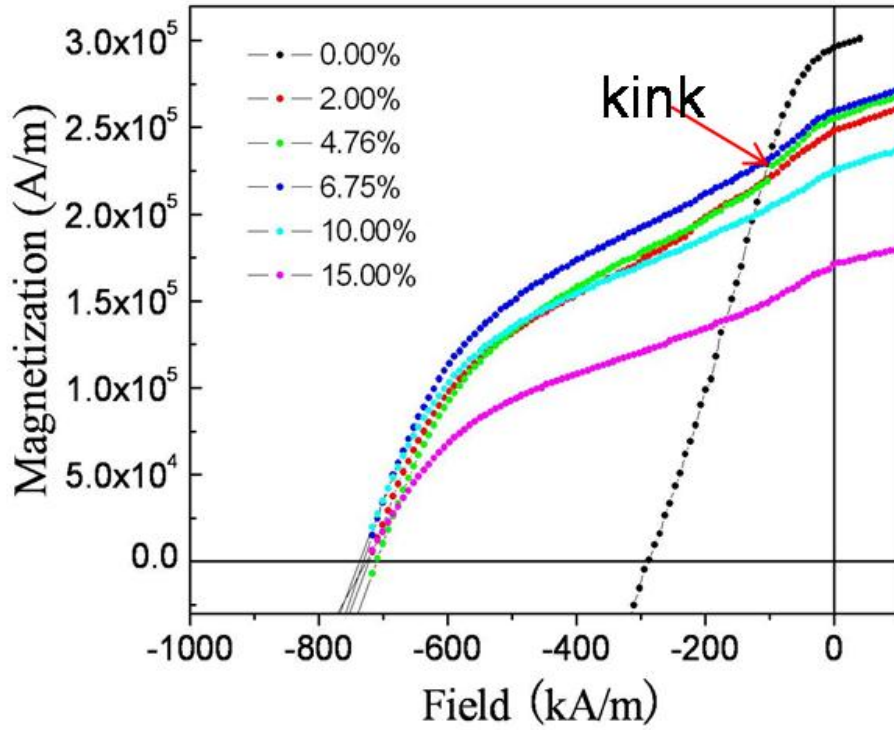


Figure 4-5. Demagnetization curves of wax bonded Nd-Fe-B micromagnets with various loading of wax powder.

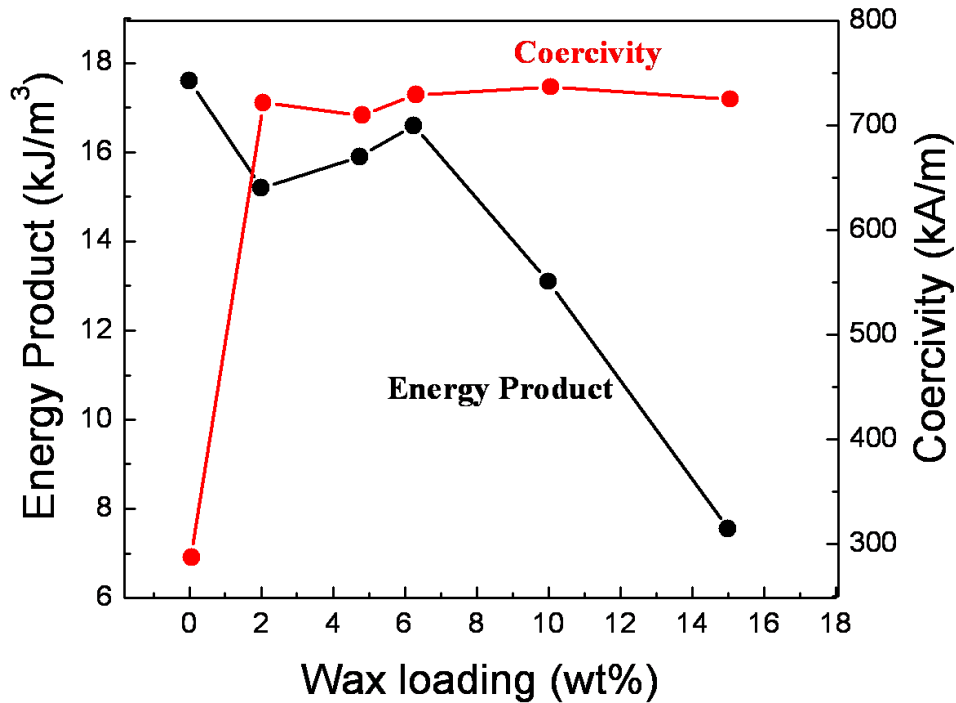


Figure 4-6. Energy products and coercivities of wax bonded Nd-Fe-B micromagnets as function of wax weight percentage.

## CHAPTER 5 INTEGRATION OF PERMANENT MAGNET MATERIALS INTO MICROTRANSDUCERS

Portions of this chapter are reproduced with permission from IEEE from the following article: N. Wang and D. P. Arnold, "Batch-Fabricated Electrodynamic Microactuators with Integrated Micromagnets," *IEEE Trans. Magn.*, accepted, 2010.

As discussed in Chapter 1, magnetically-driven transducers are attractive for MEMS because of the potential for creating large actuation displacements at low voltages [66]. Specifically, electrodynamic transducers with permanent magnets are promising due to the favorable scaling with decreased size [67]. However, while there are numerous examples of magnetic MEMS using soft magnets, the integration of permanent magnetic materials into MEMS processing has been a challenge [6]. Therefore, most reported micro electrodynamic transducers use external magnetic fields [66] or manually assembled bulk magnets for the device structure [68]-[69]. This manual assembly raises problems of misalignment and low manufacturability.

In the past, only a few micromagnetic transducers with fully-integrated permanent micromagnets have been demonstrated. Lagorce and Allen [72] reported cantilever-type microactuators with integrated polymer magnets. The magnets consisted of ferrite powder and epoxy resin with volume loading of 80%. The magnets were placed at the free end of 7-mm-long Cu cantilever beams. Planar coils (31 turns) under the magnets were used to drive the magnets to vibrate vertically. A static deflection of 15  $\mu\text{m}$  was achieved with input current of 100 mA. Cho and Ahn [70] also reported a cantilever-type microactuator with electroplated Co-Ni-Mn-P magnet array. The magnets were fabricated at the free end of a 6-mm-long silicon cantilever beam. A commercial inductor was used to drive the beam to vibrate. Bi-direction deflection of 80  $\mu\text{m}$  had been

obtained with a dc current of 100 mA. Dieppedale [71] investigated an in-plane, bi-stable magnetic switch using an electroplated Co–Pt–P magnet. A mobile Co–Pt–P magnet was placed between two sets of fixed magnets. The mobile magnet could be move in plane by applying pulse current in a coil placed under the magnets. Switching time of 30  $\mu$ s was demonstrated with peak actuation current of 4 A. Sutanto and Hesketh reported bidirectional microvalves using electroplated Co–Pt [73] and Co–Ni–Mn–P magnets [74]. The microvalve consisted of an Au microcoil sitting on a soft magnetic base and an electroplated magnet hanging below a soft magnetic membrane with supported legs. Displacements of 30–100  $\mu$ m were reported for input power of 1.2–1.6 W.

In this chapter, wax-bonded powder Nd–Fe–B permanent magnets are integrated into functional MEMS transducers in order to demonstrate the utility of these magnets for electrodynamic transduction. The reason that the wax-bonded magnets are chosen instead of the Co–Pt magnets is because the processing of the wax-bonded magnets are faster and lower cost. Moreover, magnets with high volume ( $\text{mm}^3$  range) can be obtained which is important for maximizing the strength and range of the magnetic fields. Two types of electrodynamic microtransducers based on the wax-bonded magnets are introduced, specifically, the cantilever-type and the piston-type microtransducers. The details of operation principles and fabrication processes will be presented. Finally, the actuation performance will be characterized and the results will be discussed.

## 5.1 Cantilever-Type Microtransducer

### 5.1.1 Operation Principle

The first transducer is a cantilever-type design. Figure 5-1 shows the basic structure of the cantilever-type microtransducer. The device consists of a wax-bonded powder Nd–Fe–B micro magnet embedded in a standard silicon wafer and a suspended lollipop-shaped electroplated copper coil sitting above the magnet. When current flows in the coil, a Lorentz force acts to deflect the suspended coil in the vertical direction. A cartoon of the deflection mode is shown in Figure 5-2. In order to maximize the radial magnetic field intensity, the coil is located directly above the inner edge of the magnet, as shown in the finite element modeling (FEM) in Figure 5-3 (COMSOL Multiphysics 3.2). At the coil location, a radial magnetic flux density of 0.09 T is estimated.

### 5.1.2 Fabrication Process

Figure 5-4 shows a schematic of the fabrication process for the cantilever-type transducer. The fabrication process starts by deep reactive ion etching (DRIE) cavities ~15  $\mu\text{m}$  deep on the front side of a double-side polished 100 mm diameter silicon wafer. DRIE is also used from the backside to define ~450  $\mu\text{m}$  deep cavities for the magnets. Wax-bonded Nd–Fe–B micromagnets are then formed in the cavities using the methods described in Chapter 4. The only difference here is that a wax powder (Logitech Ltd. 0CON-196) with a higher melting point (180 °C) is used here. The wax melting temperatures were adjusted accordingly and the wax melting time was kept the same (30 s).

After fabrication of the magnets, AZ 9260 photoresist is spun on the front side as a sacrificial material to fill the shallow front cavities. The thickness of the photoresist needs to be precisely controlled in order to get a flat surface. Ti (10 nm)/Cu (200 nm)

seed layers are dc sputtered on top of the sacrificial photoresist, followed by patterned electroplating of Cu coils. After electroplating, the copper coil is released by wet etching the Ti/Cu seed layers and the photoresist. After fabrication, the wafer is singulated, and individual devices are glued and wire-bonded onto a PCB. Before characterization, the device is put in a pulse magnetizer to magnetize the magnets with a magnetic field of ~3T.

Figure 5-5 shows top-side and back-side views of a cantilever-type microtransducer. The copper coil has a trace width of 100  $\mu\text{m}$ ; the radial portion is 1 mm in length, and the central circular portion is 1 mm in diameter. Two different coil thicknesses were fabricated, 6.5  $\mu\text{m}$  and 12.0  $\mu\text{m}$ . On the back side of the device is an annular-shaped magnet with inner diameter of 1 mm so that the coil is located directly above the inner edge of the magnet for maximum radial magnetic field intensity and thus high Lorentz force.

### **5.1.3 Experiment Results**

For characterization, the devices are actuated using ac current excitation, and the vibration amplitudes are measured under an optical microscope using a scanning laser vibrometer (LV) (Polytec MSV 300). A schematic of the experiment setup is shown in Figure 5-6. The laser point is placed at the end of the beam where the maximum deflection occurs. The LV system supplies a driving signal through a Techron 7540 power amplifier to the device. A Tektronix TCPA 300 current probe is used to measure the current flowing in the coils. The measured current signal is then input back into LV as a reference signal in order to obtain the normalized vibration amplitude (displacement divided by current).

Figure 5-7 shows the normalized vibration amplitude as a function of the driving frequency for the two different coil thicknesses, 6.5  $\mu\text{m}$  and 12.0  $\mu\text{m}$ . The resonant frequencies of the two devices are 680 Hz and 1185 Hz, respectively, and the quality factors are 83 and 131, respectively.

Figure 5-8 shows the displacement as a function of input rms current of these two devices in the flat band at 100 Hz. Both of the devices show linear response, i.e. the deflections increase linearly with the driving current amplitude. The 6.5  $\mu\text{m}$  thick coil has much larger displacement compared with the 12  $\mu\text{m}$  thick coil. This is expected since the thicker beam will have a higher mechanical stiffness. A 2.66  $\mu\text{m}$  displacement is obtained from the 6.5  $\mu\text{m}$ -thick-coil microtransducer for a driving current of 5.5  $\text{mA}_{\text{rms}}$ .

## **5.2 Piston-Type Microtransducer**

### **5.2.1 Operation Principle**

Figure 5-9 shows the schematic of the piston-type microtransducer. Here, a wax-bonded Nd–Fe–B micromagnet is suspended in the center of a compliant polydimethylsiloxane (PDMS) membrane. PDMS is an attractive material for large-stroke, low-frequency applications. PDMS has very low Young's modulus of 750-2000 kPa [75], much lower than silicon (162 GPa) or other polymers such as polyimide (2.5 GPa) [77] or parylene (2.8 GPa) [76]. A lower modulus enables more compliant mechanical flexures, generally at the expense of lower resonant frequencies. PDMS has a tensile strain limit up to 100%, which also makes possible high stroke devices. In addition, PDMS can be spin-deposited/cured at low temperature and has good thermal and chemical stability, permitting integration with other MEMS processing steps.

In contrast to the cantilever-type transducer described previously, this transducer relies on a moving magnet, as opposed to a moving coil. A 3-turn spiral Cu coil on the

top wafer surface surrounds the membrane. When currents flow in the Cu coil, a Lorentz force acts on the center magnet, acting to deflect the PDMS diaphragm vertically.

The FEM of the radial magnetic flux density distribution is shown in Figure 5-10. The B field at the location of the coils depends on the dimension of the devices, i.e. the size of the magnets and the distance between the magnets and coils. The dimensions of two piston-type devices are listed in Table 5-1. Figure 5-11 shows the magnetic field distribution of these two transducers at the coil plane. The maximum radial magnetic flux densities are 0.15 and 0.13 for the magnet in Transducer 1 and Transducer 2 respectively. The details about the modeling of these devices are further discussed in Chapter 6.

### **5.2.2 Fabrication Process**

Figure 5-12 shows the fabrication process for the piston-type transducer. The process starts from a double-side-polished 100-mm-diameter silicon wafer. First, a seed layer of Ti (10 nm)/Cu (100 nm) is deposited by dc sputtering, followed by patterning 25  $\mu\text{m}$  thick photoresist (AZ 9260) to form an electroplating mold for the Cu coil. Thick Cu coils ( $\sim 35 \mu\text{m}$ ) are then electroplated. The thickness of the Cu coils is intended to be larger than the thickness of the photoresist mold in order to form a mushroom head on top of the coils, as shown in Figure 5-13. This mushroom head is used to mechanically lock the PDMS membrane and enhance the adhesion of the PDMS with the silicon substrate. After stripping the photoresist mold and seed layers, 20  $\mu\text{m}$  thick PDMS is then spin-coated overtop the coil and cured at 90 °C for 2 hours.

After fabrication of the coil and diaphragm on the front side, embedded Nd–Fe–B magnets (450  $\mu\text{m}$  in depth and 2 mm in diameter) are fabricated on the backside using

the methods described in Chapter 4 (but again with the higher melting point wax). Lastly, the backside of the wafer is patterned again and deep-etched using DRIE to release the diaphragm. Individual devices are then diced from the processed wafer for characterization. Contact windows for the coil bond pads are opened by laser ablation of the PDMS using a 1047-nm Nd:YLF laser (Resonetics, Inc.).

Figures 5-14 and 5-15 show the top-side and back-side views of two piston-type microtransducers. The 3-turn coil has a linewidth of 100  $\mu\text{m}$  and line spacing of 50  $\mu\text{m}$ . The PDMS diaphragm is transparent with thickness of 15  $\mu\text{m}$ .

### **5.2.3 Experiment Results**

For characterization, the devices are actuated using ac current excitation, and the vibration amplitudes are measured using a Polytec MSV 300 scanning laser vibrometer, as shown in Figure 5-6. Figure 5-16 shows the normalized vibration amplitude as a function of the driving frequency for these transducers. The measurement point is placed in the center of the mass in an effort to measure the peak displacement. Note that the performances of the two transducers are similar. In particular, both transducers have the same vibration amplitude in the low-frequency flat-band range and at resonance. The low-frequency response of a second-system is dominated by the mechanical compliance. At the resonant frequency, the response is dominated by the mechanical damping. Because the width of PDMS spring (opening) of both devices is the same (200  $\mu\text{m}$ ), the compliance and damping of diaphragm are close, which results in the similar performance. The resonant frequencies of the two devices are 565 Hz and 800 Hz, respectively, with the lower resonant frequency a result of the larger center mass.

In order to examine the uniformity of the vibration on the whole surface of the center mass, the laser measurement point was also placed at the edges of the center mass. The points are named east, west, north and south points in order to distinguish them from the center point discussed above. Figure 5-17 shows the frequency response of the transducers at these points. All the points show similar behavior. However, at some measurement points, small peaks are shown at high frequency (~900 Hz), indicating more complex vibration modes. These small peaks are potentially caused by the wobbling of the center mass due to the non-uniform etching of the back opening during DRIE. For the smaller transducer 2, the differences between the measurement points are less prominent than that of Transducer 1, which indicating a better control of DRIE when the open area is small.

Figure 5-18 shows the displacement as function of applied rms current at flat band of 200 Hz and at resonance of the two transducers. At 200 Hz, the deflection amplitude of both the transducers increases near linearly with the input current amplitude. The displacements of 1.8  $\mu\text{m}$  and 2.2  $\mu\text{m}$  are achieved for Transducer1 and Transducer 2 with input current of 630 and 670  $\text{mA}_{\text{rms}}$ , respectively. At resonance, however, nonlinear effects (specifically a spring stiffening effect) start to appear when the current increases. This nonlinearity starts when the current reach to 200  $\text{mA}_{\text{rms}}$  current /  $\sim 3 \mu\text{m}$  displacement for Transducer 1, and 300  $\text{mA}_{\text{rms}}$  current /  $\sim 4 \mu\text{m}$  displacement for Transducer 2. A maximum deflection of 4.7  $\mu\text{m}$  is achieved for an input current of 310  $\text{mA}_{\text{rms}}$  for Transducer1 at the resonance; while a maximum deflection of 5.2  $\mu\text{m}$  is achieved for an input current of 400  $\text{mA}_{\text{rms}}$  for Transducer2.

### 5.3 Conclusion

This work demonstrates the feasibility of using wax-bonded powder Nd–Fe–B permanent magnets to fabricate electrodynamic micro transducers. Both cantilever- and piston-type microtransducers were fabricated using batch MEMS fabrication processes. Vertical deflections of 2.66  $\mu\text{m}$  and 2.2  $\mu\text{m}$  were achieved by cantilever-type and piston-type transducers, respectively, with input currents of 5.5  $\text{mA}_{\text{rms}}$  and 670  $\text{mA}_{\text{rms}}$ . The purpose here was to demonstrate functional, fully microfabricated, electrodynamic out-of-plane transducers. The devices here were not “designed” for any particular application. However, with slight modifications and focused design, these simple microtransducers can be expanded to develop new types of micro transducers for applications such as switches, valves, pumps, etc. In addition, the same fabrication process can be applied to fabricate smaller devices (100  $\mu\text{m}$ –1 mm in diameter) with smaller magnets using magnetic powders with smaller particle size.

Table 5-1. Dimensions of the piston-type transducers.

Transducers	Transducer 1	Transducer 2
Diameter of diaphragm (mm)	5.37±0.02	2.57±0.01
Diameter of center mass (mm)	5.03±0.01	2.22±0.01
Diameter of the magnet (mm)	4.80±0.02	1.82±0.03
Thickness of PDMS ( $\mu\text{m}$ )	15.1±0.04	15.1±0.04
Thickness of the center mass ( $\mu\text{m}$ )	475±5	475±5

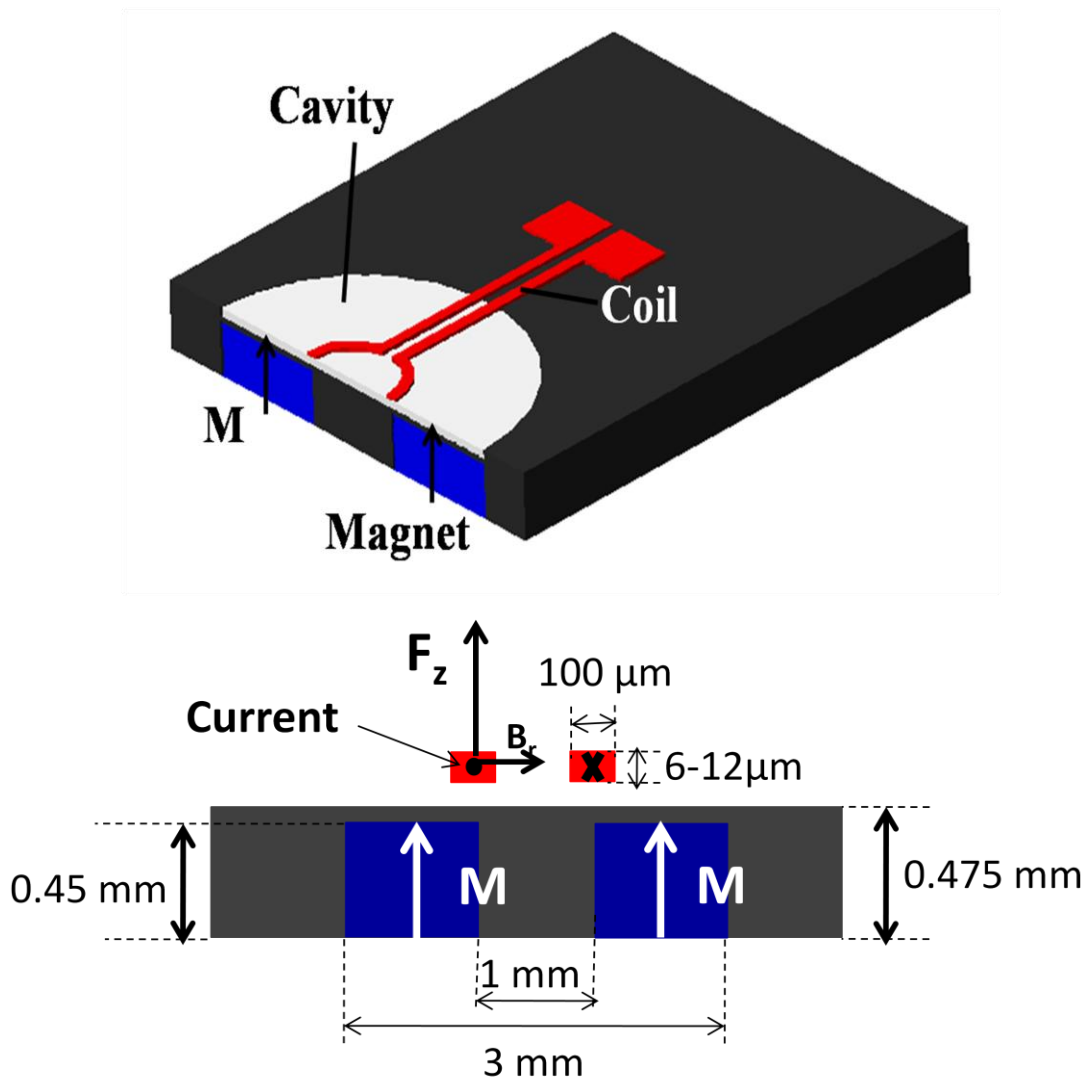


Figure 5-1. Schematic 3-D cut-away and cross-section view of a cantilever-type microtransducer.

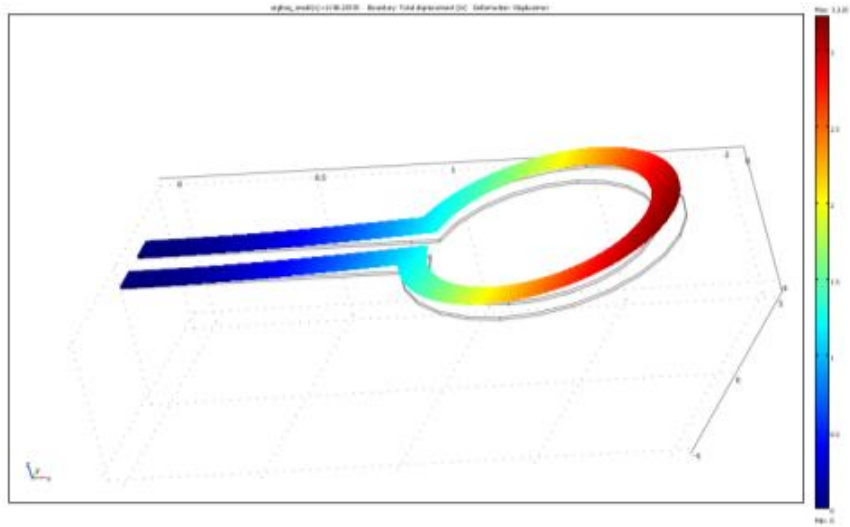


Figure 5-2. Simulated deflection of a cantilever-type microtransducer.

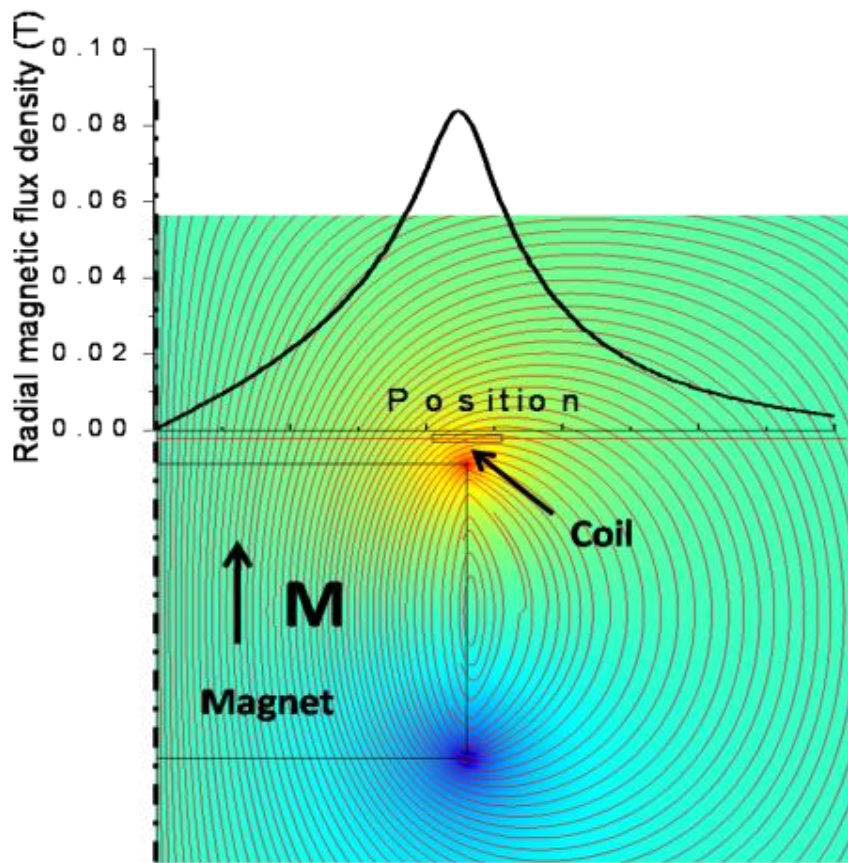


Figure 5-3. 2D axisymmetric FEM simulation of distribution of magnetic field lines and the radial magnetic flux density in the coil plane as a function of position for the cantilever-type microtransducers.

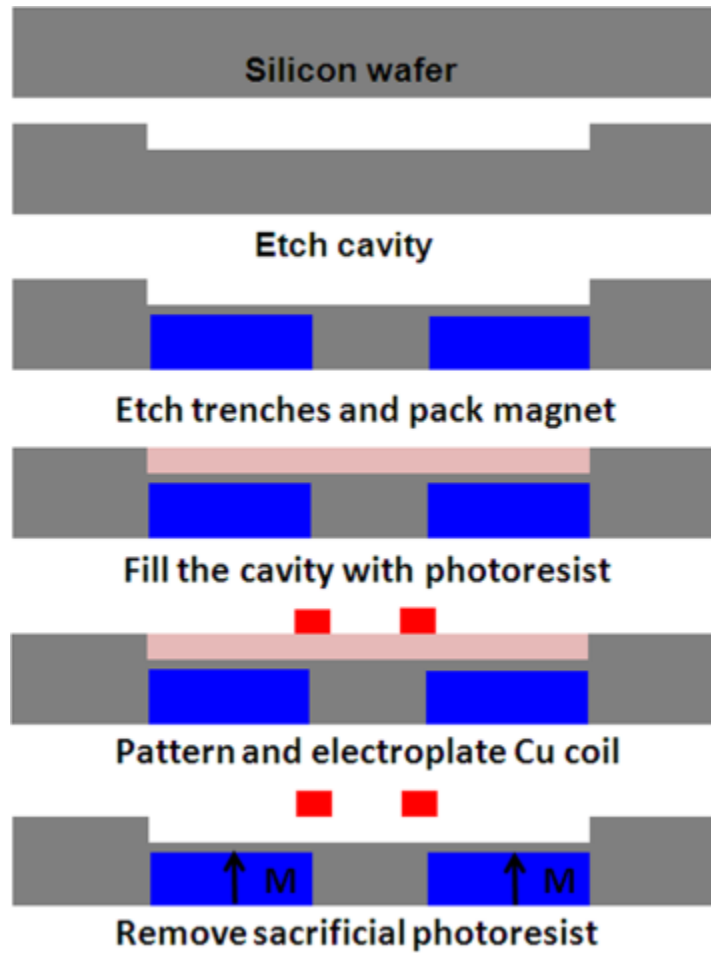


Figure 5-4. Fabrication process of the cantilever-type microtransducers.

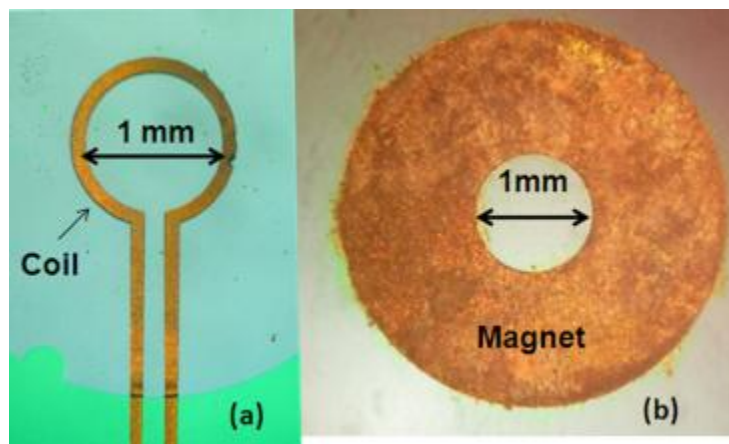


Figure 5-5. A cantilever-type microtransducers (a) front side view of suspended lollipop-shaped Cu coil and (b) back side view of embedded Nd-Fe-B magnet.

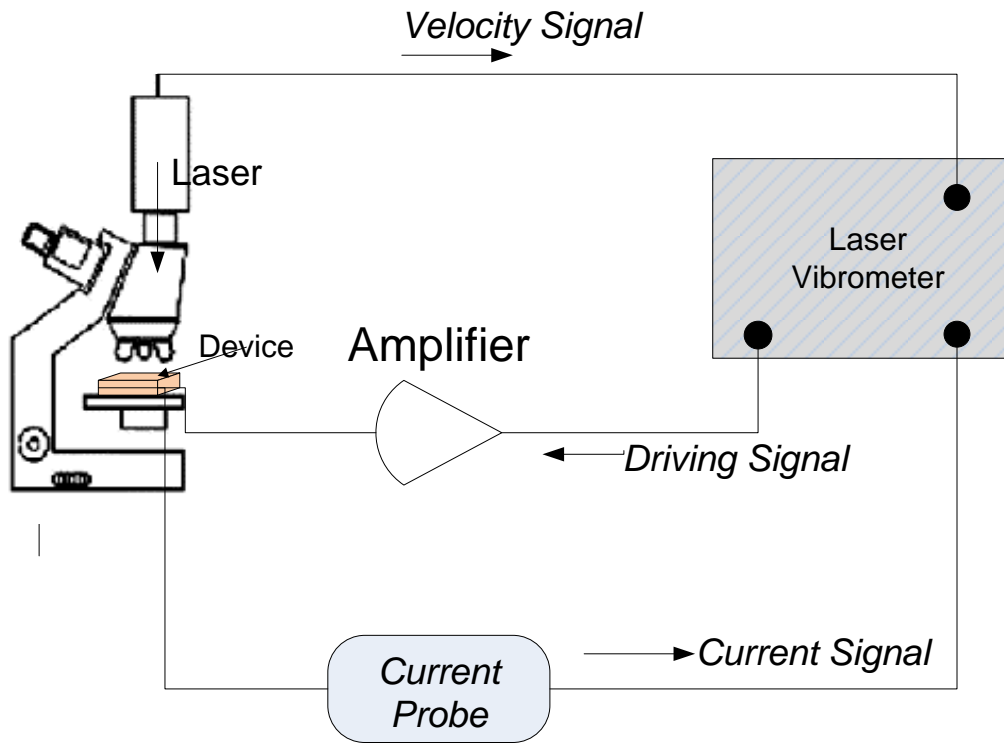


Figure 5-6. Displacement measurement setup.

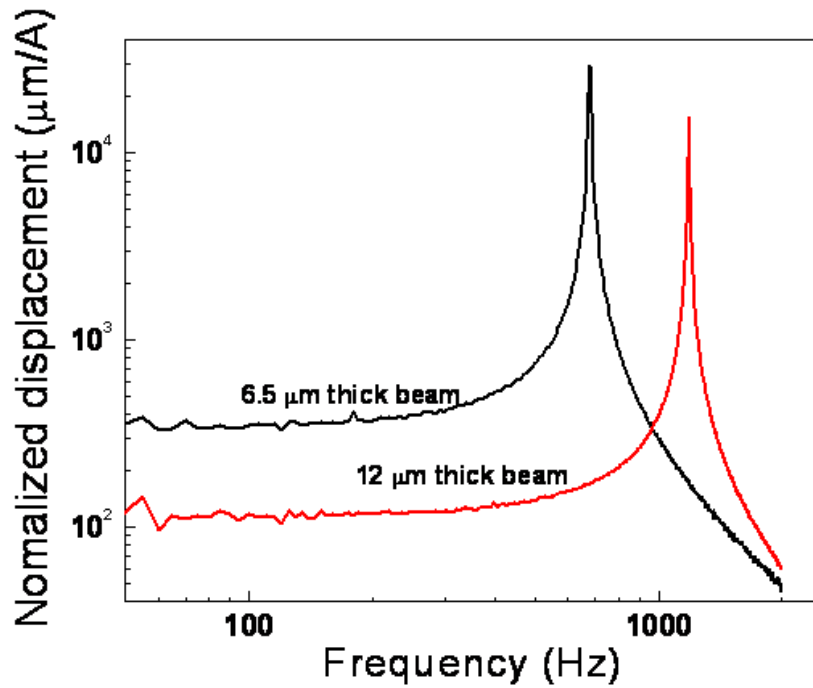


Figure 5-7. Normalized vibration amplitude as a function of the driving frequency for two cantilever-type microtransducers.

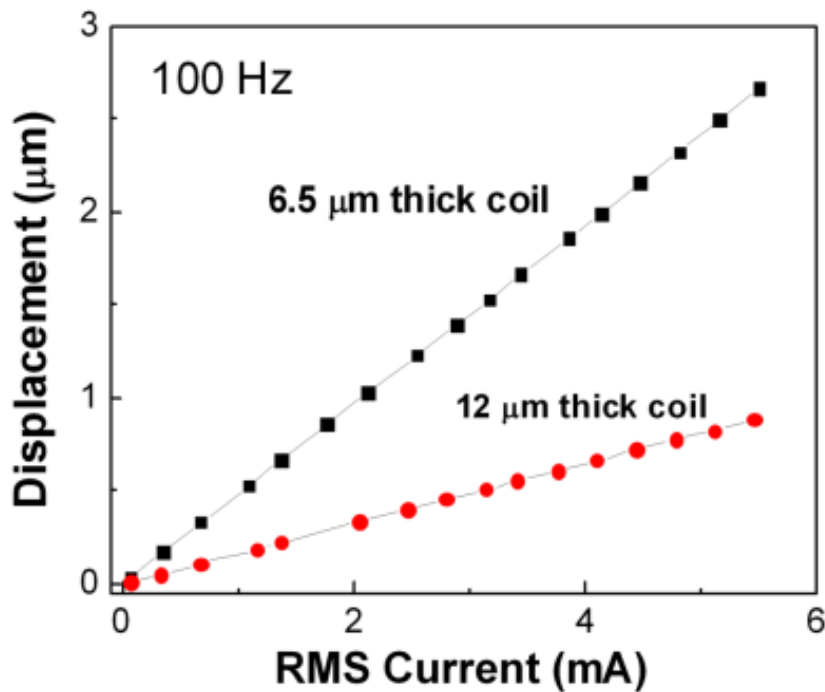


Figure 5-8. Displacement as a function of input rms current of two cantilever-type microtransducers at 100 Hz.

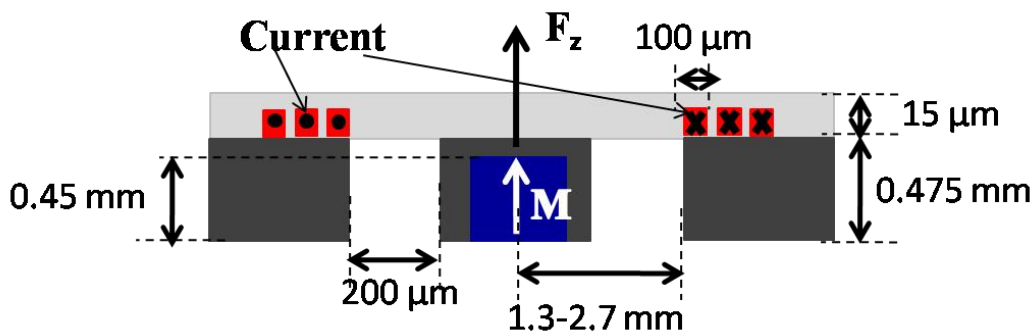
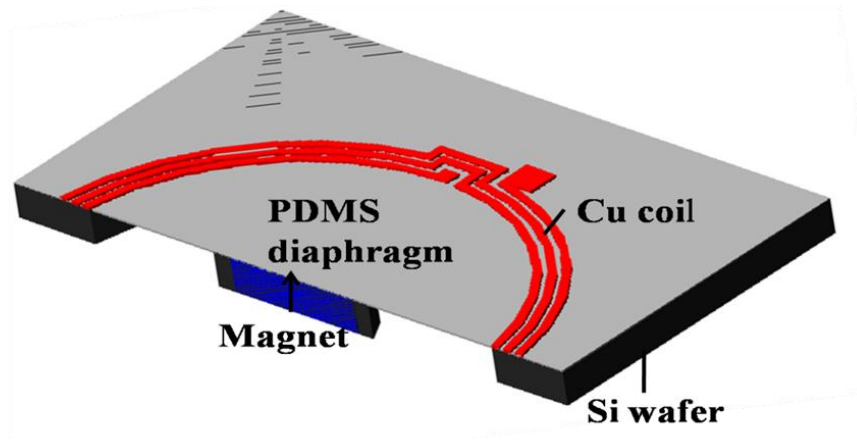


Figure 5-9. Schematic 3-D cut-away and cross-section view of a piston-type microtransducer.

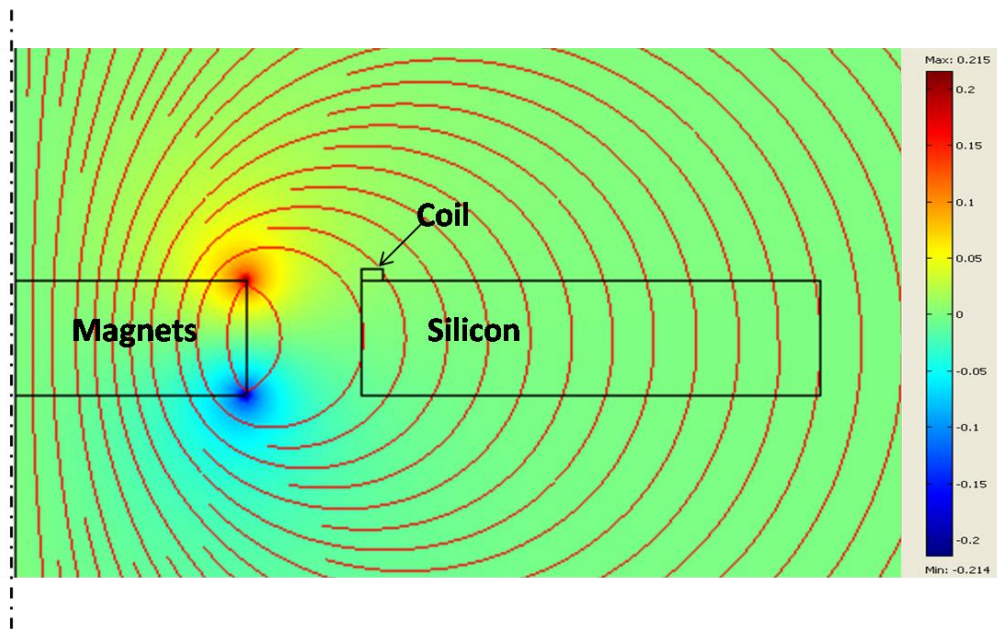


Figure 5-10. 2D axisymmetric FEM simulation of the distribution of magnetic field lines and the radial magnetic flux density for the piston-type microtransducers.

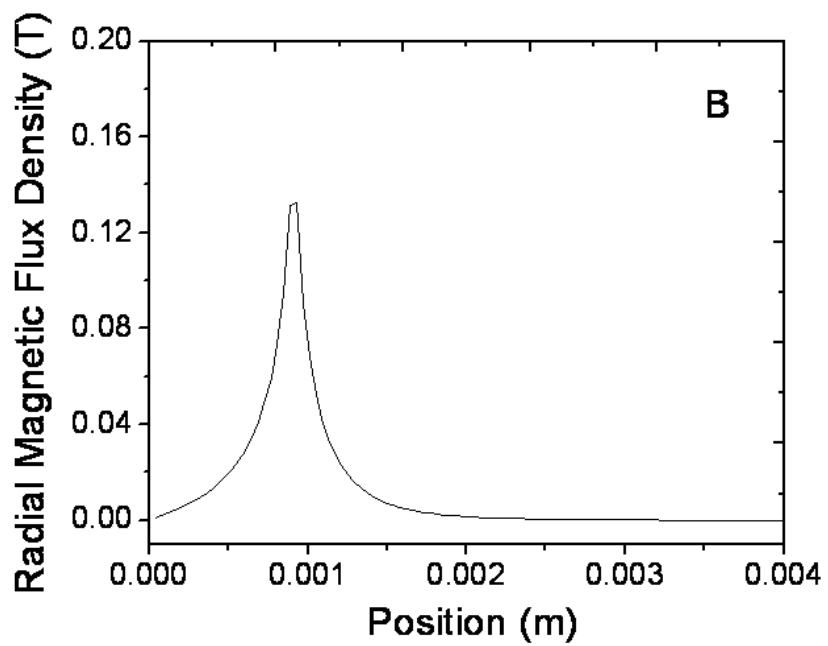
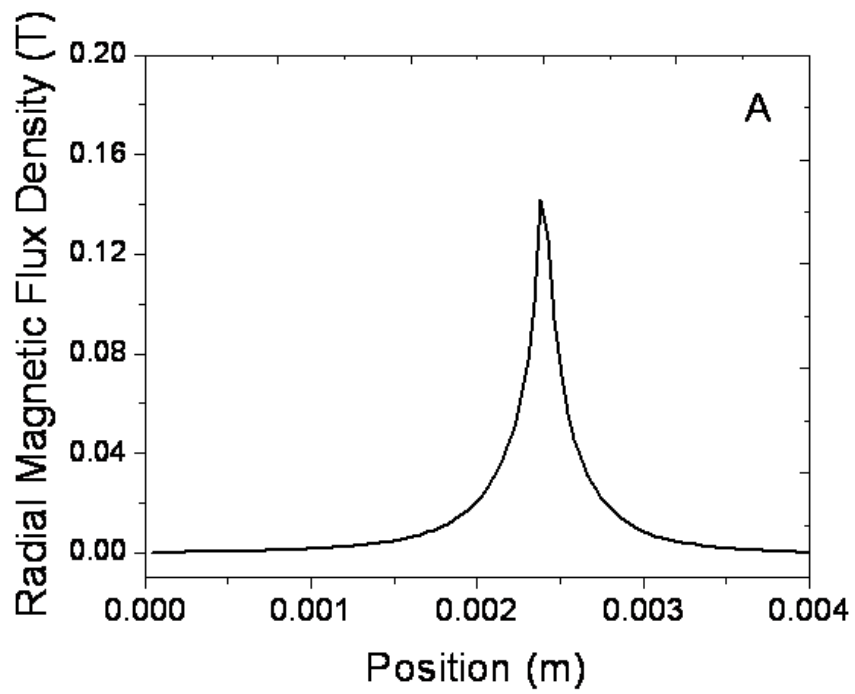


Figure 5-11. The radial magnetic flux density at the coil plane of the piston-type microtransducers for magnets of a) 1.1 mm and b) 2.5 mm in radius.

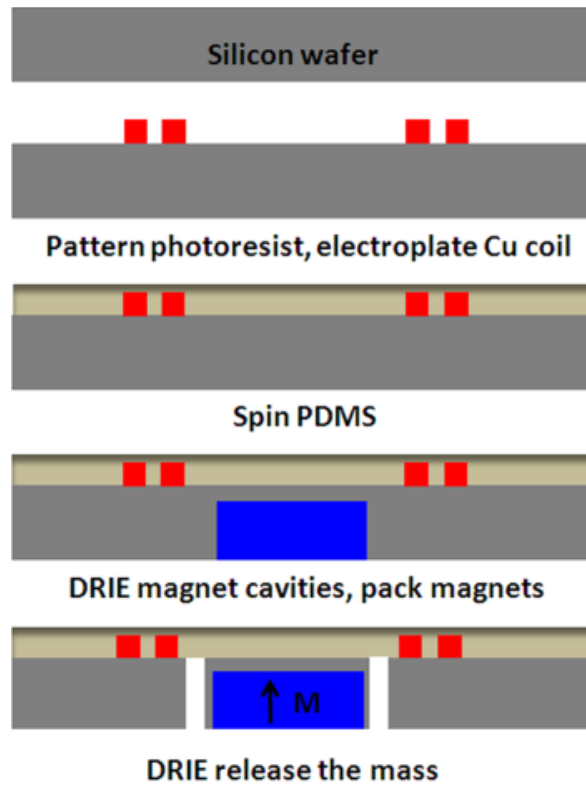


Figure 5-12. Fabrication process of the piston-type microtransducers.

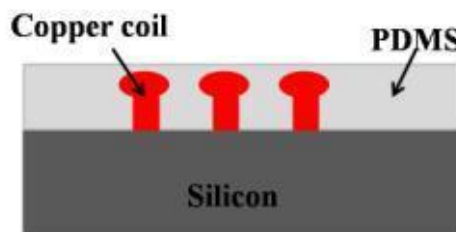


Figure 5-13. Schematic cross-section of copper coil with mushroom head embedded in PDMS diaphragm.

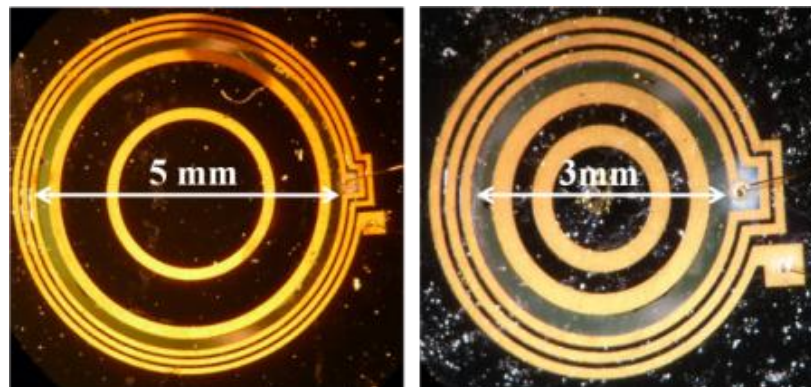


Figure 5-14. Top-view of various microfabricated piston-type transducers with different dimensions.

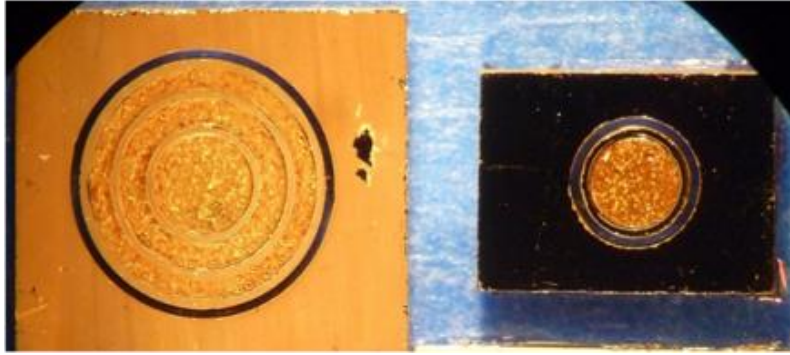


Figure 5-15. Bottom-view of various microfabricated piston-type transducer with different magnet patterns.

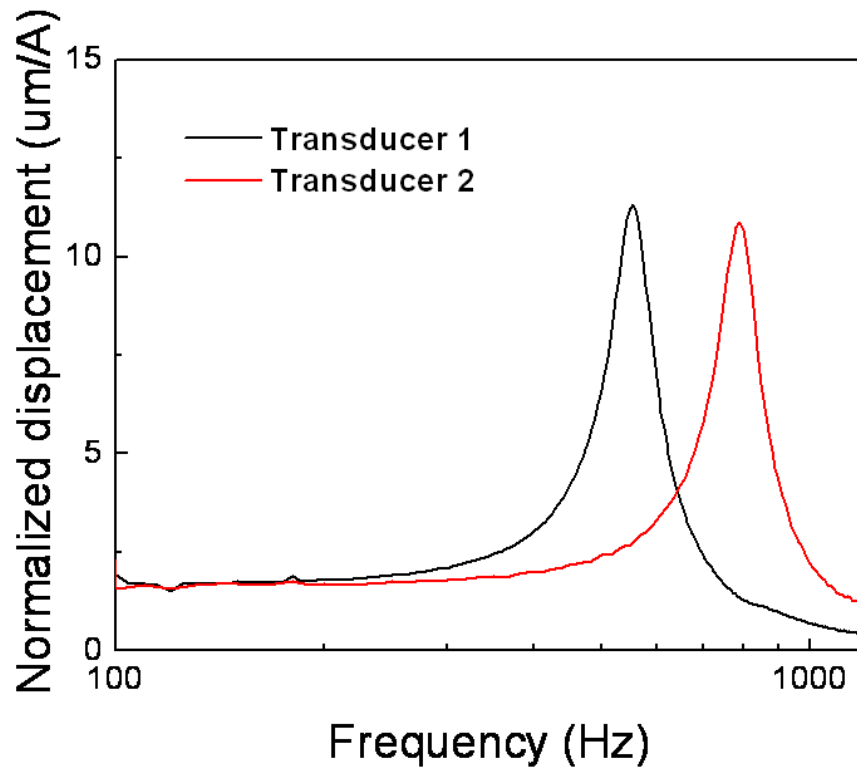


Figure 5-16. Normalized vibration amplitude as a function of the driving frequency for piston-type microtransducers.

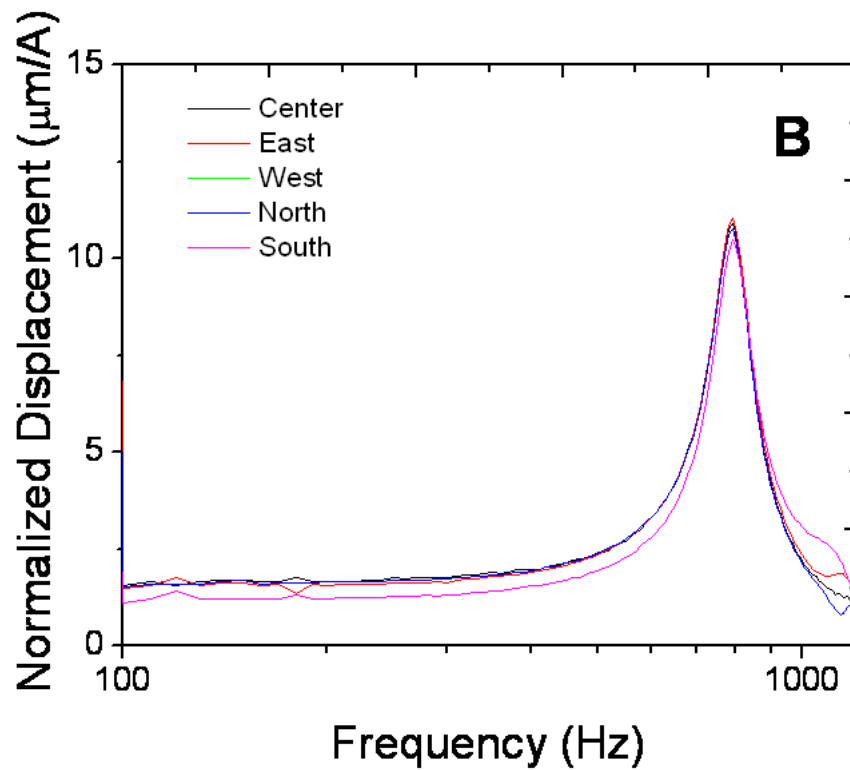
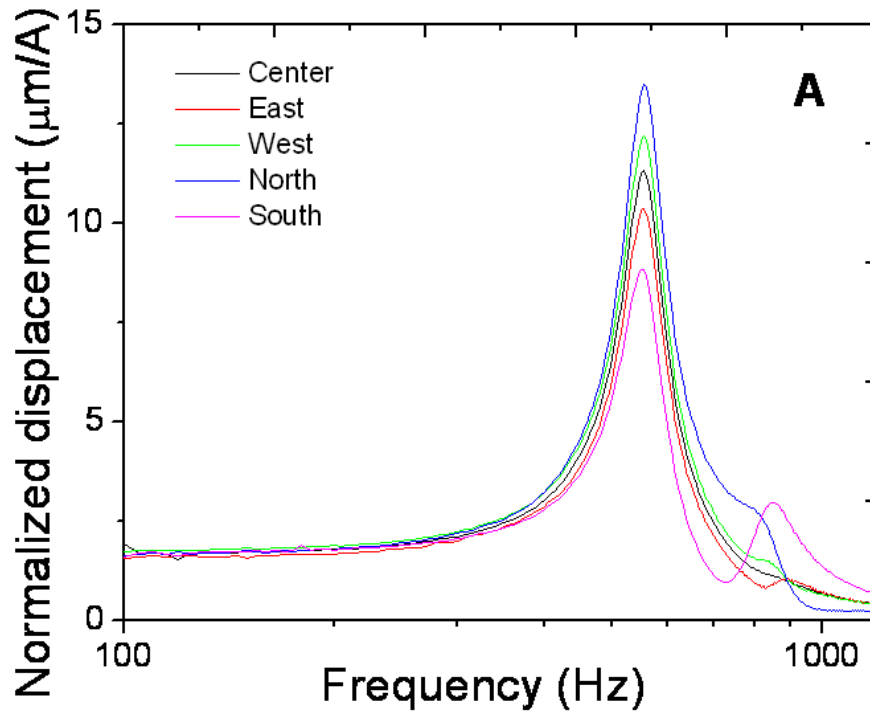


Figure 5-17. Normalized vibration amplitude as a function of the driving frequency for a piston-type (A) Transducer 1 and (B) Transducer 2 at different measurement points.

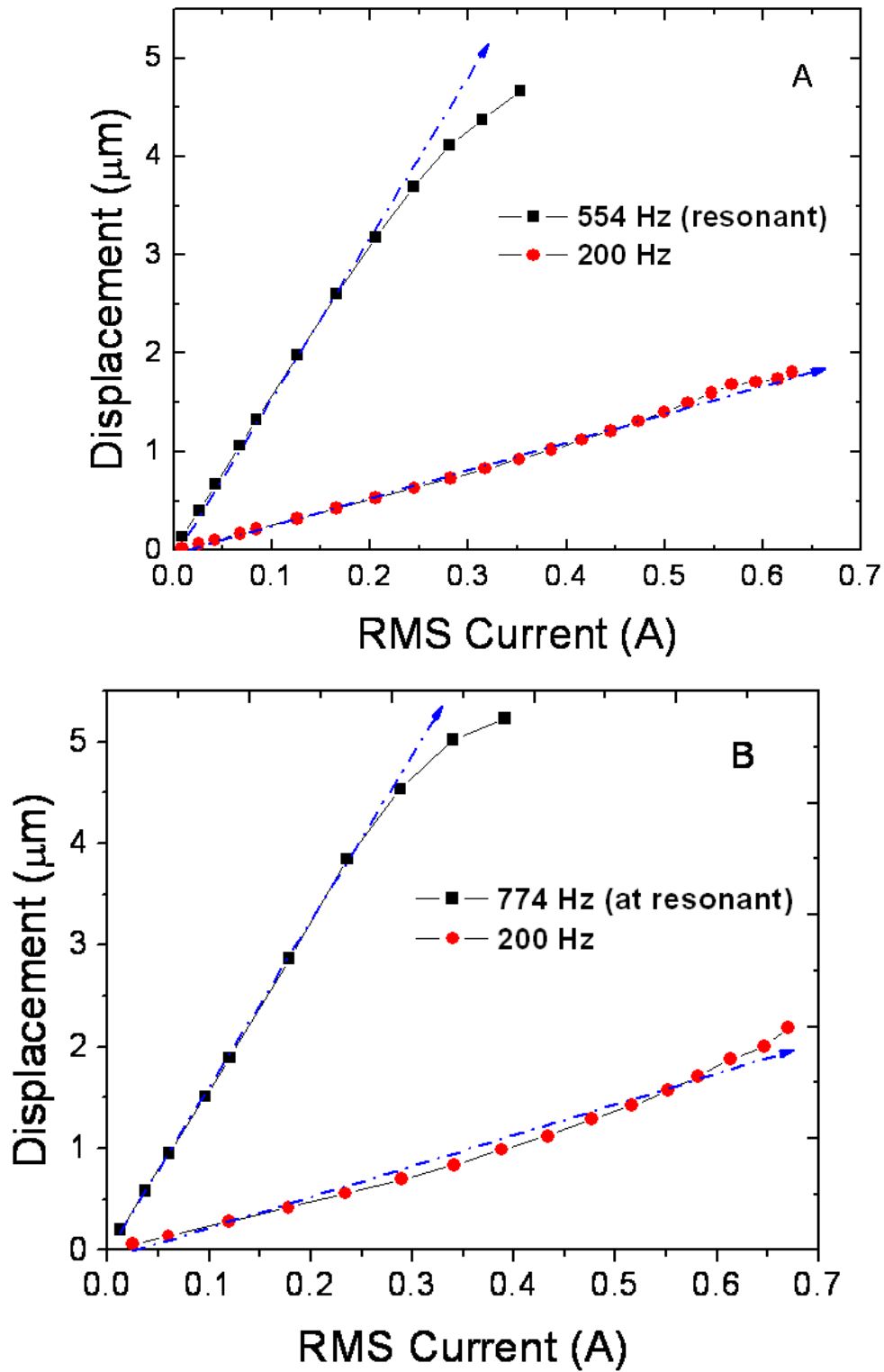


Figure 5-18. Displacement as a function of input rms current of for the piston-type A) Transducer 1 and B) Transducer 2 at flat-band of 200 Hz and at the resonant frequency.

## CHAPTER 6

### LUMPED ELEMENT MODELING OF ELECTRODYNAMIC TRANSDUCERS

In order to expand the prototype microtransducers introduced in Chapter 5 to new applications, a systematic design and modeling approach is required. Lumped element modeling (LEM) has been proven as an effective tool for modeling transducers with multiple coupled energy domains [1, 78]. The physics behind a transducer, such as the effects of device dimensions and materials properties to the device performance, the coupling between multiple energy domains, and coupling between the device and the environment can be systematically represented by an equivalent electrical circuit network. In this chapter, electromechanical LEMs are developed for the piston-type electrodynamic transducer prototypes. First, the basic principle of LEM is introduced, and modeling of electrodynamic transduction is discussed. Then, the piston-type transducers are modeled in two different operating modes: (1) as an electroacoustic actuator (microspeaker) and (2) as a mechano-electrical device (vibrational energy harvester). The modeling principles, physical parameters, governing equations, and overall simulation results are discussed in detail.

#### **6.1 LEM of Electrodynamic Transduction**

The concept behind LEM is to reduce the complexity of an analytical or numerical expression by breaking down a given distributed system into discrete elements based on how the system interacts with energy [1]. More specifically, the total energy going into any given system is divided among three distinct types of interaction: the storage of kinetic energy, the storage of potential energy, and the dissipation of energy [79]. The primary assumption required for LEM is that the length scale of the device or component is much smaller than the characteristic length scale of the physical

phenomena (e.g. wavelength) [79]. For example, the acoustic wavelength at 1 kHz is about 340 mm, which is much larger than the size of the transducers introduced in Chapter 5. Under this assumption, the governing partial differential equations can be simplified to ordinary differential equations, and each of the various energy storage/dissipation mechanisms can be “lumped” into an electrical circuit element to physically represent the transducer’s properties. For example, mass (kinetic energy storage) is represented by an inductor, compliance (potential energy storage) by a capacitor, and damping (energy dissipation) by a resistor [1]. Furthermore the whole transducer system can then be represented by an equivalent electrical circuit network by considering the energy exchange between the lumped elements.

Every element in a transducer interacts with each other and the outside world through “ports”. A port is defined by a pair of domain-specific conjugate power variables, described as “effort”,  $e$ , and “flow”,  $f$ . The product of effort and flow determines the power exchange through a port (energy into or out of the port). In different energy domains, the conjugate power variables are different, as listed in Table 6-1, e.g. voltage/current in the electrical domain and force/velocity in the mechanical domain. By convention, an impedance analogy is often applied, where the impedance of a lumped element is defined as the ratio of the effort and the flow, i.e.  $Z = \frac{e}{f}$ . As a result, elements that share a common effort are connected in parallel, and those sharing a common flow are connected in series. More details about LEM can be found in [1], [78] and [79].

### 6.1.1 Electrodynamic Transduction Model

Electrodynamic transduction involves the interaction between permanent magnets and current-carrying coils. In the piston-type transducers discussed in Chapter 5, this electrodynamic transduction is realized by vibration of the magnet attached to the PDMS diaphragm relative to the coils. In the rest of this section, the model of electrodynamic transduction for electromechanical and electroacoustic coupling will be discussed.

In an electrodynamic conversion model, the voltage induced  $V_{emf}$  on the terminals of the coil, according to Faraday's law with time-constant electromagnetic field [80], equals

$$V_{emf} = \oint_{l_{coil}} (\vec{v} \times \vec{B}) \cdot d\vec{l} \quad (6-1)$$

where  $v$  is the relative velocity of the coil and the magnet,  $l_{coil}$  is the total length of the coil and  $B$  is the flux density at each coil segment. In the piston-type transducer structure, the current flows in the wafer plane and the direction of the velocity is perpendicular to the wafer plane, as shown in Figure 6-1. Therefore, only the radial magnetic flux density contributes to the induced voltage. Additionally, when the transducer displacement is sufficiently small—such that the coil does not experience significant changes in the B-field during the motion—the relationship between voltage and velocity can be simplified to the simple linear equation

$$V_{emf} = B_{avg} l_{coil} v = Kv \quad (6-2)$$

where  $B_{avg}$  is the average radial flux density at the coil position.

Also, the magnetic force on the conductor is given by [80],

$$\vec{F} = I \oint_{l_{coil}} d\vec{l} \times \vec{B} \quad (6-3)$$

where  $I$  is the current. Again assuming the B-field acting on the coil does not significantly change with displacement and only the radial flux density (hence the vertical force) is considered, the force and current are linearly related by

$$F = B_{avg} l_{coil} I = KI \quad (6-4)$$

In both equations, the proportional constant  $K = B_{avg} l_{coil}$  is called the electrodynamic transduction coefficient. Note that only the forces and velocities in the direction of vibration are considered (perpendicular to the diaphragm in the case here). Other transverse forces may exist and induce transverse vibrations, but for simplicity, these effects are ignored in this analysis. The governing equations for electrodynamic transduction can be obtained by combination of equation (6-2) and (6-4),

$$\begin{pmatrix} F \\ u \end{pmatrix} = \begin{pmatrix} 0 & K \\ \frac{1}{K} & 0 \end{pmatrix} \begin{pmatrix} V \\ I \end{pmatrix} \quad (6-5)$$

By convention, an impedance analogy is employed, and thus the electrodynamic transduction can be represented in an equivalent circuit by an ideal gyrator. The gyrator is a two-port electric circuit element that relates efforts and flows between its two ports. “Ideal” means that no power is dissipated when the energy is transferred from one domain to another through the gyrator.

If the acoustic domain is considered, for example an electrodynamic speaker, the acoustic variables are related to the mechanical variables by the physical transducer

structure. For example, the force shown in equation (6-3) and (6-4) can be converted to an equivalent pressure, which is given by

$$P = F / S_{eff} \quad (6-6)$$

where  $S_{eff}$  is the effective area of the diaphragm. An effective area is used instead of the whole area of the diaphragm because, when vibrating, the displacement of the diaphragm is not constant across the entire diaphragm. The calculation of the effective area will be discussed in Section 6.1.3. Similarly, the acoustic volume velocity can be calculated by the velocity of diaphragm multiplied by the effective area

$$Q = vS_{eff} \quad (6-7)$$

Therefore, the characteristic electrodynamic equations that govern the interaction between the electrical and acoustic domain are given by

$$\begin{pmatrix} P \\ Q \end{pmatrix} = \begin{pmatrix} 0 & G \\ \frac{1}{G} & 0 \end{pmatrix} \begin{pmatrix} V \\ I \end{pmatrix} \quad (6-8)$$

where  $G = B_{avg} l_{coil} / S_{eff}$  is the electrodynamic transduction coefficient in electroacoustic variables. The mechanical and acoustic transduction coefficients have a simple relation of

$$G = \frac{K}{S_{eff}} \quad (6-9)$$

Figure 6-2 shows the gyrator models for the electro-mechanical and electro-acoustical couplings, respectively. Similarly, the relation between the mechanical and acoustic impedance is thus given by,

$$Z_{acoustic} = \frac{p}{Q} = \frac{F / S_{eff}}{S_{eff} v} = \frac{F}{S_{eff}^2 v} = \frac{Z_{mechanical}}{S_{eff}^2} \quad (6-10)$$

### 6.1.2 Transduction Coefficient Model

As indicated in equation (6-2) and (6-4), the transduction coefficient depends on the total length of the coil and the radial magnetic flux density at the coil position. In the acoustic domain, the effective area should also be considered, which is given later in equation (6-21). The radial magnetic flux density from a cylindrical magnet can be calculated using an analytic approximation. More details about the calculation can be found in [83], [86]-[87].

Assuming an “ideal” cylindrical magnet of radius  $r_m$  and thickness  $h_m$  sits in a cylindrical coordinate system. The bottom center of the magnet is placed at the origin of a cylindrical coordinate system. Assuming the magnet is uniformly magnetized in the z direction, the z- and r- components of the B-field at a point P(r,  $\theta$ , z) are given exactly by [83], [86]-[87]

$$B_z = \frac{B_0}{2\pi} \int_0^{h_m} \frac{1}{\sqrt{(r_m + r)^2 - (z - z')^2}} \times \left( \frac{(r_m^2 - r^2) - (z - z')^2}{(r_m - r)^2 - (z - z')^2} E(k) + K(k) \right) dz' \quad (6-11)$$

$$B_r = \frac{B_0}{2\pi} \int_0^{h_m} \frac{z - z'}{r \sqrt{(r_m + r)^2 - (z - z')^2}} \times \left( \frac{(r_m^2 - r^2) - (z - z')^2}{(r_m - r)^2 - (z - z')^2} E(k) - K(k) \right) dz' \quad (6-12)$$

where  $B_0$  is the remnant magnetic flux density of the magnet,  $K(k)$  and  $E(k)$  are the complete elliptic integrals of the first and second kind, respectively, and  $k$  is given by

$$k = \sqrt{\frac{4r_m r}{(r_m + r)^2 + (z - z')^2}} \quad (6-13)$$

Using a hypergeometric expansion to approximate the elliptic integrals, the equations of (6-14) and (6-15) can be expressed as [83], [86]-[87],

$$B_z = -B_0 \sum_{n=0}^{\infty} \frac{(-1)^n (2n+1)!}{2^{2n+2} (n!)^2} \left\{ \left[ \left( \frac{r_m}{z} \right)^2 \left( \frac{r}{z} \right)^{2n} \times F \left( n+1, n+\frac{3}{2}; 2; -\left( \frac{r_m}{z} \right)^2 \right) \right] \right\} \\ - \left[ \left( \frac{r_m}{z-h_m} \right)^2 \left( \frac{r}{z} \right)^{2n} \times F \left( n+1, n+\frac{3}{2}; 2; -\left( \frac{r_m}{z-h_m} \right)^2 \right) \right] \quad (6-14)$$

$$B_r = -B_0 \sqrt{\frac{r_m}{2r}} \left\{ \left[ \left( \frac{2r_m r}{(z-h_m)^2 + r^2 + r_m^2} \right)^{3/2} \times F \left( \frac{5}{4}, \frac{3}{4}; 2; \left( \frac{2r_m r}{(z-h_m)^2 + r^2 + r_m^2} \right)^2 \right) \right] \right\} \\ - \left[ \left( \frac{2r_m r}{z^2 + r^2 + r_m^2} \right)^{3/2} \times F \left( \frac{5}{4}, \frac{3}{4}; 2; \left( \frac{2r_m r}{z^2 + r^2 + r_m^2} \right)^2 \right) \right] \quad (6-15)$$

where  $F$  is the Gauss hypergeometric function.

Using equation (6-15), Figure 6-3 A shows the calculated radial magnetic flux density at the coil position as a function of radius of the magnet, compared with the results calculated by finite element methods. In this particular calculation, the coil position  $(z, r)=(475\mu\text{m}, 3\text{mm})$ , the thickness of the magnet  $h_m= 450 \mu\text{m}$  and the remnant flux density of the magnet  $B_0 = 0.3 \text{ T}$  are fixed. Only the radius of the magnet is changed. It can be seen in Figure 6-3 B that the analytical results are 7-60% larger than the FEM results. The closer the magnet is to the coil, the closer of the analytical results agree with the FEM results. .

### 6.1.2 Planar Coil Model

The electrical behavior of the multi-turn planar coil of the piston-type transducer can be modeled by a resistor and an inductor, which are connected in series since they share the same flow (current). The low-frequency resistance is given by

$$R_{coil} = \rho \frac{l_{coil}}{A_{coil}} \quad (6-16)$$

where  $\rho$  is the resistivity of copper, and  $l_{coil}$  and  $A_{coil}$  are the length and cross-section area of the coil, respectively. The inductance of the coil is approximated by [84]

$$L_{coil} = \frac{25\mu_0}{\pi} d_{mean} P N^2 \quad (6-17)$$

where  $d_{mean}$  is the mean coil diameter,  $P$  is called Grover function is a geometric factor depending on the width and length of the coil [84], and  $N$  is the number of turns of the coil. If the length of the coil is much larger than the width of the coil, then the Grover function  $P \sim 1$ .

### 6.1.3 Diaphragm Model

The diaphragm in the piston-type transducer comprises an annular PDMS diaphragm and a stiff center mass that contains the magnet. The whole diaphragm acts as a mass-spring-damper mechanical resonator. Therefore, the diaphragm can be represented mechanically by a capacitor, an inductor and a resistor that are connected in series. The capacitance and inductance associated with the compliance and mass can be modeled analytically, as described in the rest of this section. The resistor representing the damping is obtained experimentally and will be discussed in Chapter 7.

Figure 6-4 shows the schematic cross-section of the composite diaphragm. The mechanical analysis of the clamped diaphragm with a rigid center boss can be found in [81]-[82], [85]. The model of the diaphragm is derived based on a clamped annular diaphragm with outer radius  $a$  and inner radius  $b$ , given by [81]. The assumptions behind the model are: 1) a uniform pressure  $p$  applied on the diaphragm; 2) the center

mass is perfect rigid compare to the compliant diaphragm; 3) the annular plate has uniform thickness  $h_p$  and is isotropic; 4) the maximum transverse deflection is less than 30% of the thickness of the diaphragm; 5) all forces are normal to the plane of the diaphragm; 6) the diaphragm thickness ( $h_p$ ) is small compared to the radius of the diaphragm  $a$  [82]. Note that this model assumes a pressure loading instead of point force. Thus, the acoustic impedances are developed first. The corresponding mechanical impedances are obtained by the mechanical-acoustic coupling equation given by equation (6-10).

According to [81], the transverse displacement of the diaphragm under a uniform pressure load  $p$  is given in two regions by

$$w(r)|_{0 < r < b} = \frac{3p(1-\nu_p^2)a^4}{16E_p h_p^3} \left[ 1 + 4\left(\frac{b}{a}\right)^2 \ln\left(\frac{b}{a}\right) - \left(\frac{b}{a}\right)^4 \right] \quad (6-18)$$

$$w(r)|_{b < r < a} = \frac{3p(1-\nu_p^2)a^4}{16E_p h_p^3} \left[ 1 + 4\left(\frac{b}{a}\right) \ln\left(\frac{r}{a}\right) - 2\left(\frac{r}{a}\right)^2 + 2\left(\frac{b}{a}\right)^2 - 2\frac{b^2 r^2}{a^4} + \left(\frac{r}{a}\right)^4 \right] \quad (6-19)$$

where  $E_p$ ,  $\nu_p$ , and  $h_p$  are the Young's modulus, the Poisson ratio, and the thickness of the diaphragm, respectively;  $a$  and  $b$  are the radius of the diaphragm and the center boss, respectively.

The total volume displacement/change  $|\nabla|$  is calculated by the integration of the displacements across the entire diaphragm,

$$|\nabla| = \int_0^a w(r) 2\pi r dr = \frac{\pi p(1-\nu_p^2)a^6}{16E_p h_p^3} \left[ 1 - 3\left(\frac{b}{a}\right)^2 + 3\left(\frac{b}{a}\right)^4 - \left(\frac{b}{a}\right)^6 \right] \quad (6-20)$$

The effective area, which is defined as the total volume displacement divided by the center displacement, can be calculated as

$$S_{eff} = \frac{|\nabla|}{w(0)} = \frac{\pi a^2}{3} \frac{1 - 3\left(\frac{b}{a}\right)^2 + 3\left(\frac{b}{a}\right)^4 - \left(\frac{b}{a}\right)^6}{1 + 4\left(\frac{b}{a}\right)^2 \ln\left(\frac{b}{a}\right) - \left(\frac{b}{a}\right)^4} \quad (6-21)$$

So, the acoustic compliance  $C_{da}$  of the diaphragm according to Hooke's law is given by,

$$C_{da} = \frac{|\nabla|}{p} = \frac{\pi(1 - \nu_p^2)a^6}{16E_p h_p^3} \left[ 1 - 3\left(\frac{b}{a}\right)^2 + 3\left(\frac{b}{a}\right)^4 - \left(\frac{b}{a}\right)^6 \right] \quad (6-22)$$

where the subscript "d" and "a" refers to "diaphragm" and "acoustic," respectively.

The acoustic mass (inductance) of the diaphragm  $M_{da}$  is calculated by equating the kinetic energy of the diaphragm in acoustic power variables to the total kinetic energy [85], the result given by

$$M_{da} = \frac{M_{rigid}}{S_{eff}^2} + 2\pi\rho_p h_p \int_b^a \left( \frac{w(r)}{\nabla} \right)^2 r dr \quad (6-23)$$

where  $M_{rigid}$  is the mass of the rigid center region, and  $\rho_p$  is the density of PDMS.

Knowing the *acoustic* mass and compliance, the *mechanical* compliance,  $C_{dm}$ , and mass,  $M_{dm}$ , can be calculated according to equation (6-10),

$$C_{dm} = \frac{C_{da}}{S_{eff}^2} \quad (6-24)$$

$$M_{dm} = M_{da} S_{eff}^2 \quad (6-25)$$

where subscript "m" refers "mechanical".

In summary, the complete electromechanical two-port model of the piston-type transducer is illustrated in Figure 6-5 A, and the corresponding electroacoustic model is shown in Figure 6-5 B. These electrodynamic transducer models represent the two-port electromechanical/electroacoustic behavior. These models can be used to simulate either actuation/motor mode or a sensing/generator mode by adding appropriate excitation sources and loads. In the next two sections, complete LEM models will be constructed and analyzed in two different operating modes: (1) as an electroacoustic actuator (microspeaker) and (2) as a mechanoelectrical device (vibrational energy harvester).

## **6.2 LEM of Electroacoustic Actuation Mode**

In this section, a complete LEM is developed to simulate the behavior of the piston-type transducer in an actuator mode. In particular, electroacoustic coupling will be applied so that the transducer is modeled as a microspeaker acting on a  $2 \text{ cm}^3$  cavity (a typical model of the human ear canal). The model predictions will be later compared to experimental measurements in Chapter 7.

The device will be used in the actuation mode so that, when the current flows through the coil, a Lorentz force is generated and actuates the diaphragm to vibrate and radiate sound. The back side of the device will be attached to a 2 cc coupler (FRYE Electronics Inc. Model HA-1), as shown in Figure 6-6. The 2 cc coupler has known acoustic impedance and facilitates connection of the microtransducer to a microphone (B&K type 4138) for acoustic measurement. The vibration of the diaphragm will cause a pressure,  $\Delta P$ , change inside the cavity. Simultaneously, the front side of the diaphragm will also radiate sound into free space.

The electrodynamic transducer model has been discussed in Section 6.1. In this section, the acoustic “load impedances”—the 2 cc coupler on the back side of the diaphragm and the radiation impedance on the front side of diaphragm—are first introduced. Then, the complete LEM is discussed.

### 6.2.1 2cc Coupler

The 2 cc coupler is a rigid-walled cavity with a constant volume of 2 cm<sup>3</sup>. Since the length of the cavity,  $L_c$ , is much smaller than the wavelength of the sound, the cavity is considered “acoustically short.” Thus, the acoustic impedance of the cavity is given by [90],

$$Z_{2cc} = \frac{\rho_0 c_0^2}{j\omega V_{2cc}} \quad (6-26)$$

where  $\rho_0=1.2 \text{ kg/m}^3$  is the density of the air,  $c_0= 343 \text{ m/s}$  is the speed of the sound in air and  $V_{2cc}$  is the volume of the coupler.

This equation is analogous to a capacitor with a capacitive impedance of  $Z_c = \frac{1}{j\omega C}$ . Therefore, the acoustic compliance of the 2 cc coupler can be modeled as a capacitor shown in Figure 6-7 and its compliance can be calculated by

$$C_{2cc} = \frac{V_{2cc}}{\rho_0 c_0^2} \quad (6-27)$$

### 6.2.2 Radiation Impedance

The sound radiation on the front side of the diaphragm can be roughly modeled as a piston in an infinite baffle as shown in Figure 6-8. The radiation impedance is defined by the ratio of average pressure on the piston surface over the volume velocity of the

piston. The details about the derivation can be found in [90]. If the radiation source is a compact source where  $ka \ll 1$ , where  $k$  is the wave number and  $a$  is the radius of the piston, the resulting radiation impedance is given by [90]

$$Z_{rad} = \frac{\omega^2 \rho_0}{2\pi c_0} + j\omega \frac{8\rho_0}{3\pi^2 a} \quad (6-28)$$

For transducers 1 and 2 in this dissertation,  $ka = 0.002$  and  $0.001$ , respectively, at frequency of 500 Hz, thus validating the “compact source” assumption. Note that the radiation impedance has both real and imaginary part, which can be represented by a series-connected resistor and an inductor, respectively, in an equivalent circuit model. Therefore, the radiation mass,  $M_{rad}$ , and radiation resistance,  $R_{rad}$ , are given by

$$M_{rad} = \frac{8\rho_0}{3\pi^2 a} \quad (6-29)$$

$$R_{rad} = \frac{\omega^2 \rho_0}{2\pi c_0} \quad (6-30)$$

### 6.2.3 Complete LEM

With all the models of the acoustic components, the complete equivalent circuit model of the electroacoustic actuator (microspeaker) is shown in Figure 6-9. The model has two energy domains, an electrical domain and an acoustic domain that are electrodynamically coupled via a gyrator. The transducer LEM and the transduction coefficient  $G = B_{avg} I_{coil} / S_{eff}$  where already discussed in Section 6.1. Here, an electrical source and acoustic load are added. On the left side, an ideal current source is assumed (later experiments will directly measure the input current).

On the right side, the 2 cc coupler and radiation acoustic impedances are added. Since the 2 cc coupler and the radiation impedance elements share the same flow/displacement as the diaphragm, they are all connected in series. In other words, the flow (current) is the same for the diaphragm, 2 cc coupler, and radiation. The effort (voltage drop) across the 2 cc coupler capacitance represents the sound pressure inside the 2 cc coupler.

As drawn, the circuit consists of mixed electrical and acoustic domains. However, elements can be reflected from one side of the gyrator to the other to 'eliminate' the gyrator from the circuit model (as commonly done for analyzing transformer circuits). Therefore, the multi-domain circuit can be transformed into an equivalent single-domain representation. For a gyrator, it can be shown that reflected impedances (indicated with a prime) are given by

$$Z' = \frac{G^2}{Z} \quad (6-31)$$

Because of the  $1/Z$  reciprocal relationship, when reflecting impedances, a capacitance becomes an inductance and an inductance becomes a capacitance. A resistance, with no imaginary part, remains a resistance. Also, series connected elements become connected in parallel and vice versa. Additionally, it can be shown that reflected sources are given by

$$e' = Gf \quad (6-32)$$

$$f' = \frac{1}{G}e \quad (6-33)$$

where flow sources become effort sources and effort sources become flow sources. Therefore, the whole circuit can be transformed into an equivalent single-domain representation by eliminating the gyrator, as shown in Figure 6-10. Note that the current source becomes a pressure source

$$P = GI \quad (6-34)$$

Also note the coil inductance transforms to the impedance

$$Z_{Lcoil}' = \frac{G^2}{Z_{Lcoil}} = \frac{G^2}{sL_{coil}} \quad (6-35)$$

which appears like an acoustic capacitor with capacitance of  $L_{coil}/G^2$ . The coil resistance becomes

$$Z_{Rcoil}' = \frac{G^2}{Z_{Lcoil}} = \frac{G^2}{R_{coil}} \quad (6-36)$$

In addition, series connections become parallel connections. Other acoustic impedances are

$$Z_{da} = R_{da} + sM_{da} + \frac{1}{sC_{da}} \quad (6-37)$$

$$Z_{rad} = R_{rad} + sM_{rad} \quad (6-38)$$

$$Z_{2cc} = \frac{1}{sC_{2cc}} \quad (6-39)$$

Where  $s=j\omega$  and  $\omega$  is the angular frequency. Now, the acoustic performance of the transducer will be discussed.

Using this model, we are interested in the sound pressure that can be generated in the 2 cc coupler with a given source current. As indicated in the model, the sound

pressure inside the 2 cc coupler equals the voltage drop on  $Z_{2cc}$ , which can be obtained by using standard steady-state circuit phasor analysis.

$$P_{2cc} = \frac{GIZ_{2cc}}{Z_{da} + Z_{rad} + Z_{2cc}} \quad (6-40)$$

The transfer function defined by the sound pressure ( $P_{2cc}$ ) in the 2 cc coupler normalized by the input current ( $I$ ) is then given by.

$$\begin{aligned} \frac{P_{2cc}}{I} &= \frac{GZ_{2cc}}{Z_{da} + Z_{rad} + Z_{2cc}} \\ &= \frac{G \frac{1}{sC_{2cc}}}{(R_{da} + sM_{da} + \frac{1}{sC_{ad}}) + (R_{rad} + sM_{rad}) + \frac{1}{sC_{2cc}}} \end{aligned} \quad (6-41)$$

### 6.3 LEM of Mechanoelectrical Generator Mode

In this section, LEM is used to model the piston-type transducer in a generator mode, specifically as a vibrational energy harvester. The magnetic mass is attached to the silicon wafer frame via the PDMS diaphragm. When the wafer frame experiences acceleration in the out-of-plane direction, the center magnet will be excited into oscillation, resulting in a change of magnetic flux within the area closed by the Cu coil which is affixed on the silicon wafer frame. Therefore, an induced voltage will be created in the coil based on Faraday's law. When connected to an electrical load, current will flow from the coil, and power can be delivered to an external electrical load.

The complete equivalent circuit representation for the energy harvester is shown in Figure 6-11. The portion to the left of the gyrator represents the mechanical domain, and the portion to the right of the gyrator represents the electrical domain. The transducer parameters were discussed in Section 6.1, so the discussion here focuses

on the appropriate connection of a mechanical source and electrical load. The load in this case is assumed infinite (connected to a high-impedance oscilloscope port in the experiments), so the electrical terminals are modeled as an open-circuit.

The mechanical source is a bit more complicated. In the physical system, the silicon frame surrounding the diaphragm is vibrated at a specific velocity with respect to an external reference point. This input vibration, acting on the silicon frame, is modeled as an ideal time-harmonic velocity source given as  $v_1$ . The source is ‘ideal’ in the sense that the velocity is supplied independent of the force required. The mass moves at velocity  $v_2$  with respect to an external reference point. The velocity difference between the frame and the mass,  $v_1 - v_2$ , gives rise to the relative displacement between the mass and the silicon wafer frame, as indicated in Figure 6-11.

As drawn, the LEM includes mixed energy domains. As shown before, the elements can be reflected from one side of the gyrator to the other to ‘eliminate’ the gyrator from the circuit. Figure 6-12 shows an equivalent circuit entirely in the electrical domain. Note that the velocity (flow) source becomes a voltage (effort) source. Also note the transformations between inductances and capacitances, and between series and parallel connections. In the electrical domain, the impedances of the diaphragm become

$$Z_{dM}' = \frac{K^2}{Z_{dm}} = \frac{K^2}{sM_{dm}} \quad (6-42)$$

$$Z_{dC}' = \frac{K^2}{Z_{dm}} = K^2 sC_{dm} \quad (6-43)$$

$$Z_{dR}' = \frac{K^2}{Z_{dm}} = \frac{K^2}{R_{dm}} \quad (6-44)$$

respectively. The open-circuit voltage,  $V_{oc}$ , can be obtained through standard steady-state phasor circuit analysis

$$V_{oc} = K v_1 \frac{Z_{dC}' // Z_{dR}'}{Z_{dM}' + Z_{dC}' // Z_{dR}'} \quad (6-45)$$

Where // represents connected in parallel. Since in time-harmonic motion the velocity,  $v$ , and acceleration,  $a$ , are related by

$$a = s v \quad (6-46)$$

The transfer function is defined by the open-circuit voltage normalized by the input acceleration is then given by

$$\frac{V_{oc}}{a} = K_S \frac{Z_{dC}' // Z_{dR}'}{Z_{dM}' + Z_{dC}' // Z_{dR}'} = \frac{K s^2 M_{dm}}{R_{dm} + s M_{dm} + \frac{1}{s C_{dm}}} \quad (6-47)$$

Table 6-1. Conjugated power variables in various energy domains

Energy domain	Effort	Flow
Electrical	Voltage	Current
Mechanical	Force	Velocity
Acoustic	Pressure	Volume velocity

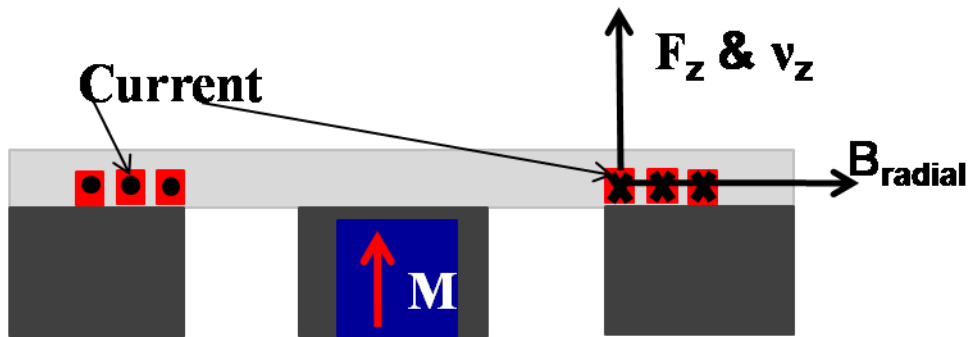


Figure 6-1. Schematic of the direction of force, velocity and radial magnetic flux density.

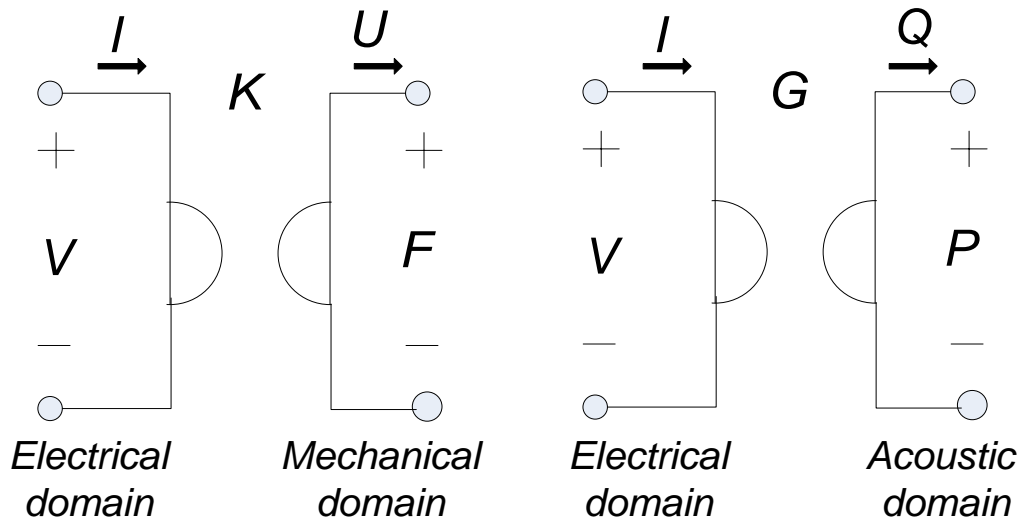


Figure 6-2. The gyrator models for electromechanical and electroacoustical coupling.

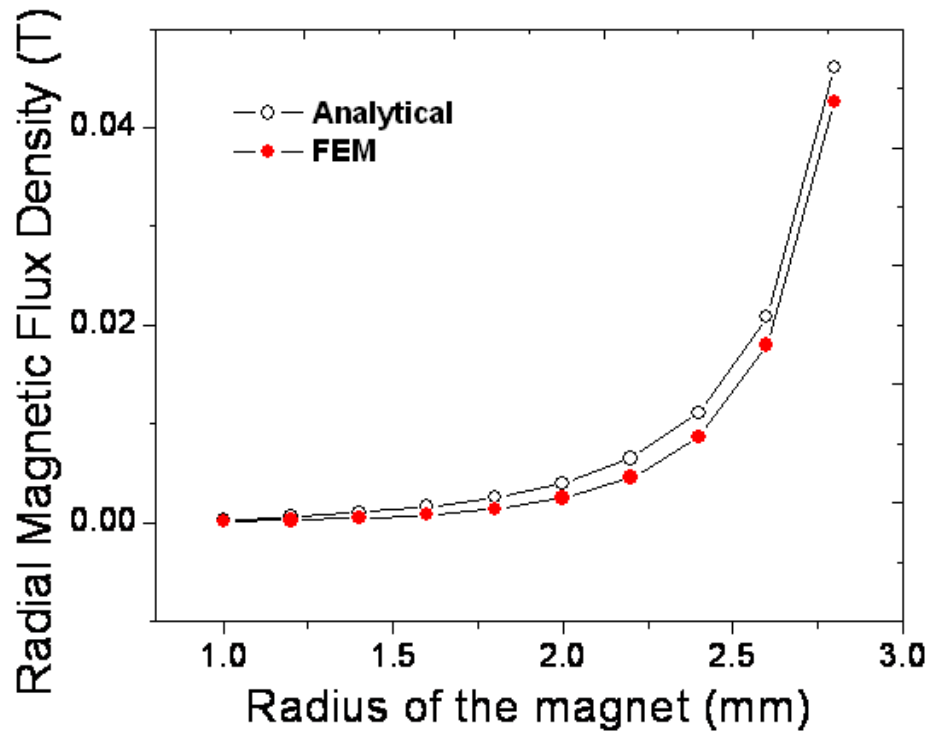


Figure 6-3. Radial magnetic flux density at coil position for increasing magnet radius using analytical and FEM calculations.

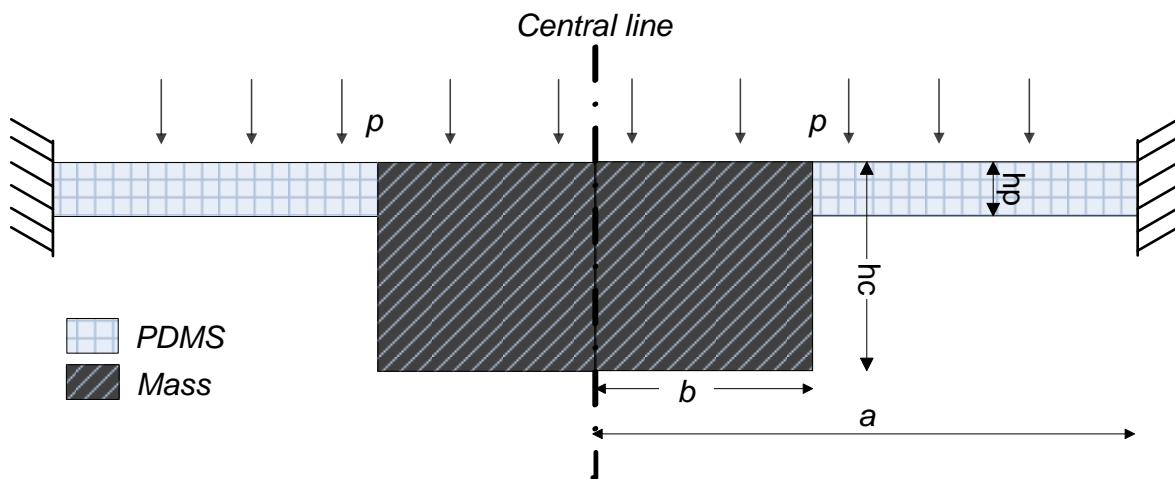


Figure 6-4. The cross-section schematic of the composite diaphragm.

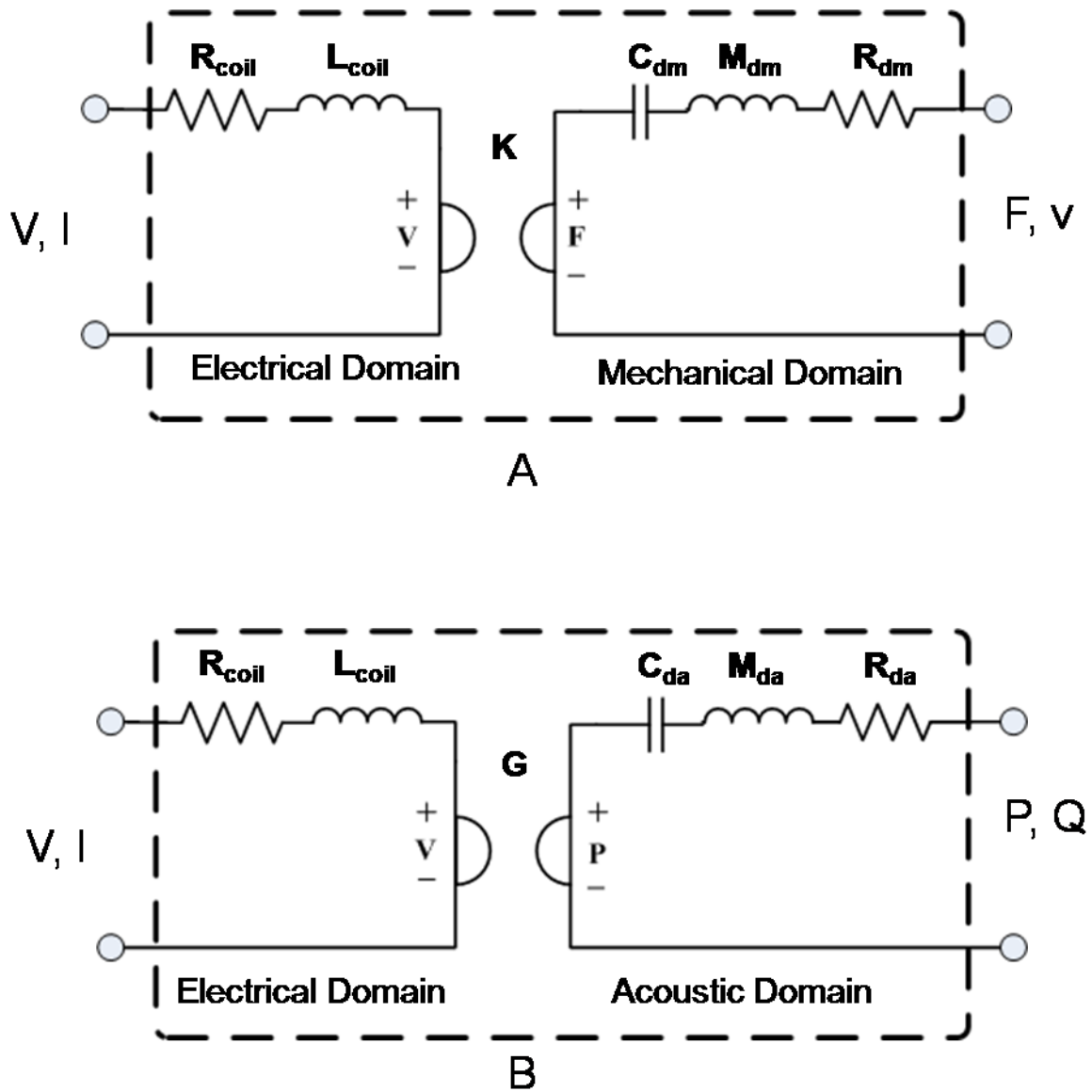


Figure 6-5. The (A) electromechanical model and (B) electroacoustic model of the piston-type transducer.

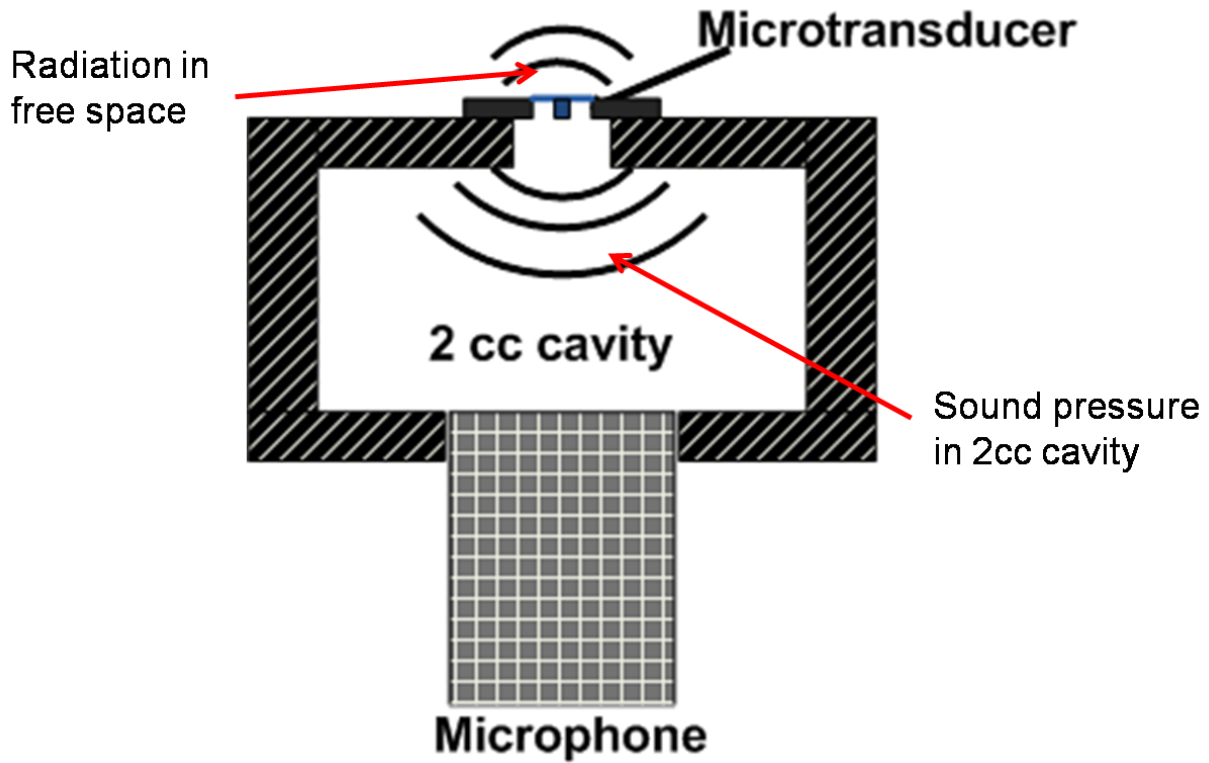


Figure 6-6. Schematic of the setup for using the transducers in acoustic actuation mode.

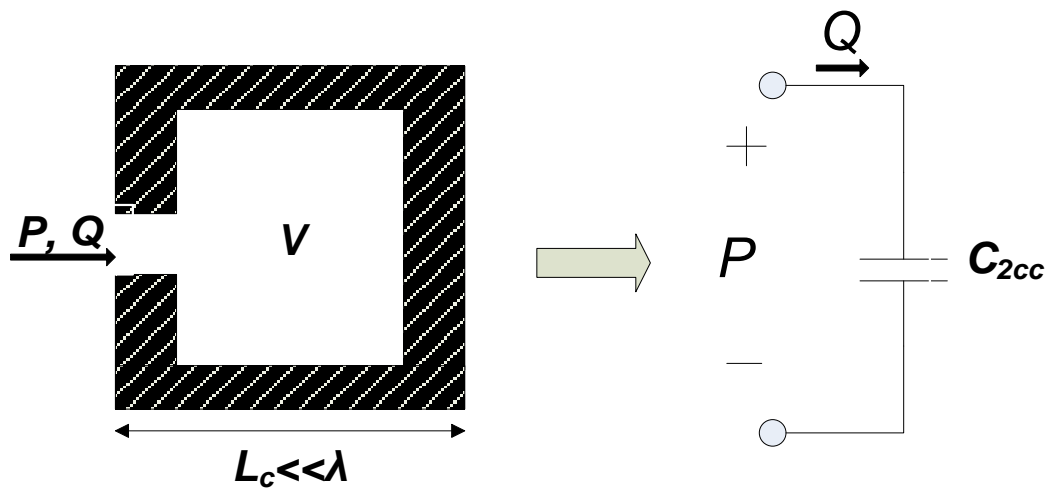


Figure 6-7. Lumped model of an acoustically short cavity.

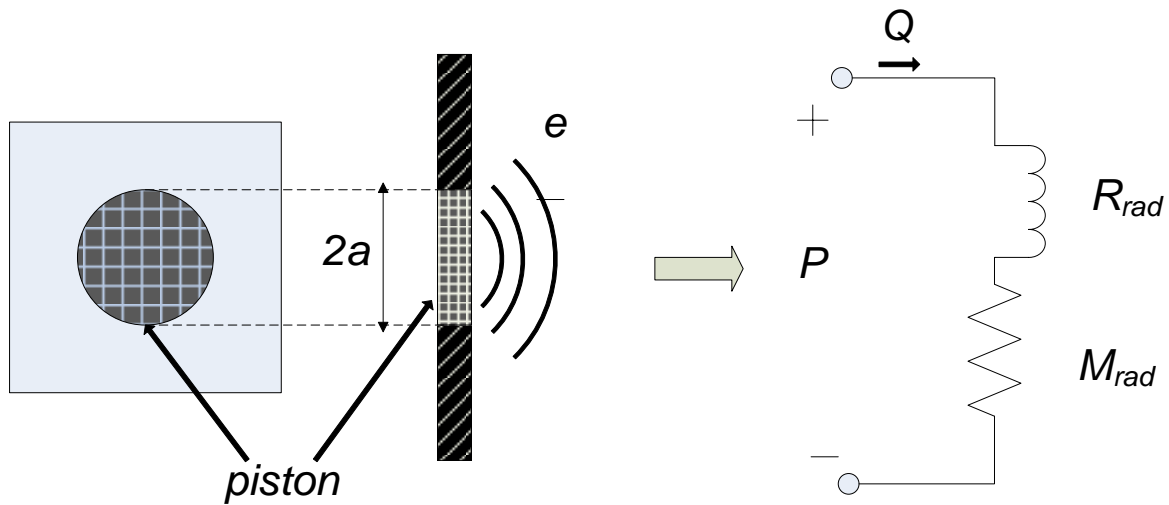


Figure 6-8. Lumped model of radiation impedance based on an infinite baffle.

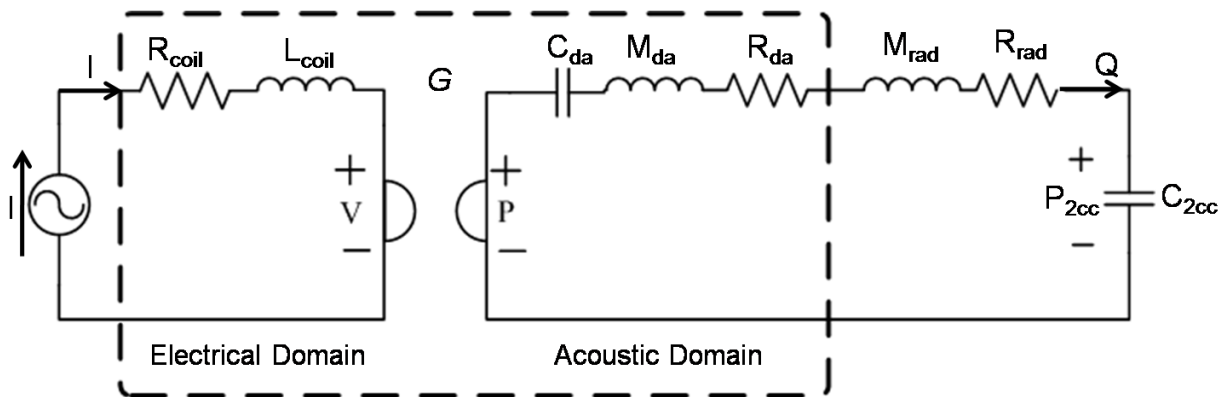


Figure 6-9. A complete LEM circuit model in an electroacoustic actuation mode.

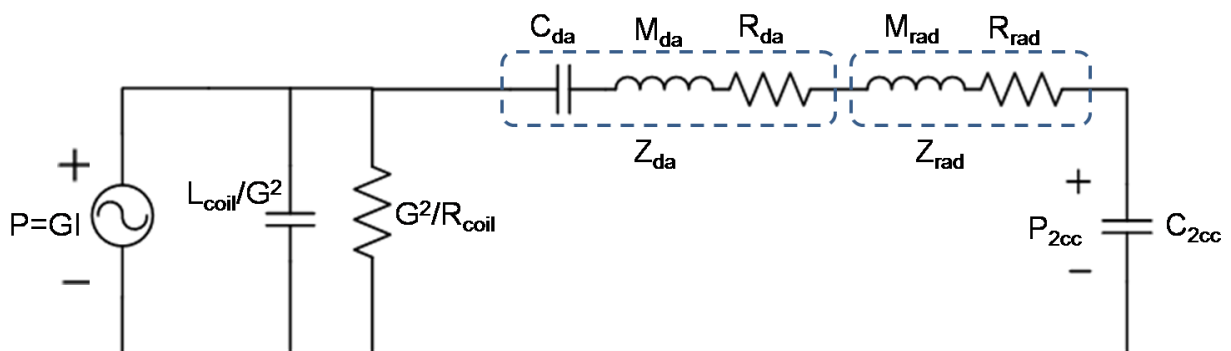


Figure 6-10. Equivalent LEM circuit model in the acoustic domain.

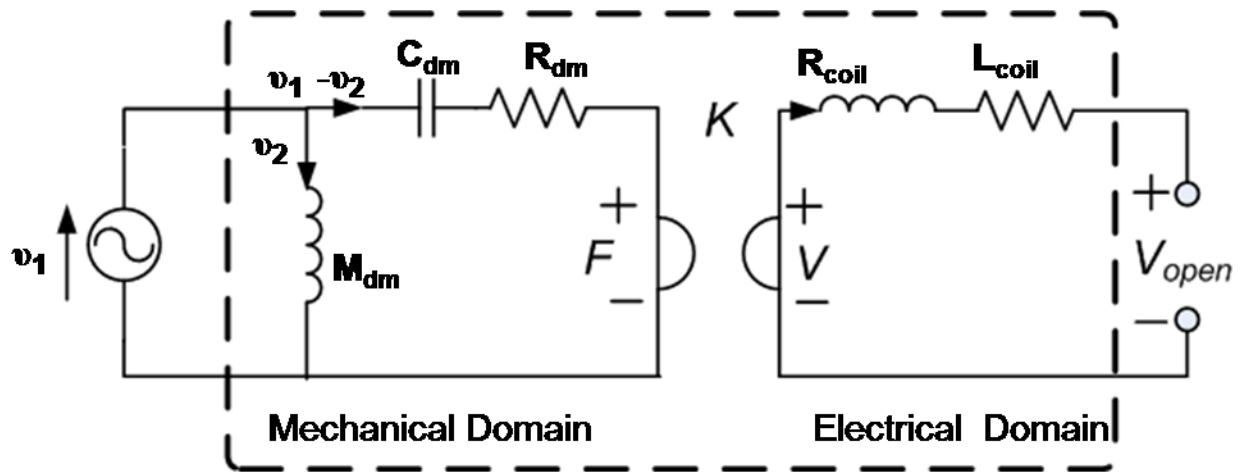


Figure 6-11. A complete LEM circuit model in mechanoelectric generator mode.

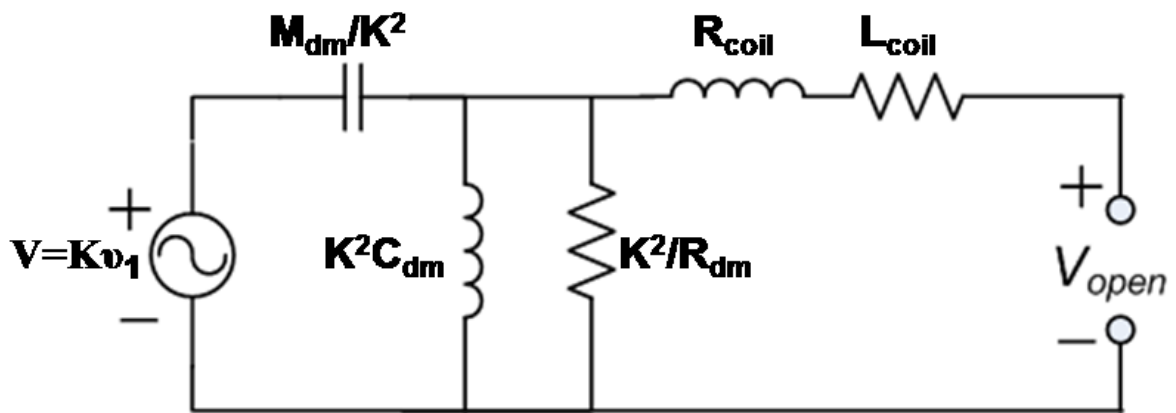


Figure 6-12. Equivalent LEM circuit model in the electrical domain.

## CHAPTER 7 EXPERIMENTAL CHARACTERIZATION AND MODEL VALIDATION OF MICROTRANSDUCERS

In the previous chapter, complete lumped element models of the piston-type transducers were developed for both the actuation mode (microspeaker) and the generator mode (vibrational energy harvester). In this chapter, where possible, the model parameters are experimentally measured/extracted. Then, the acoustic and energy harvesting performance of the two piston-type transducers are measured. Finally, the experimental results are compared with the model predictions (using the extracted parameters).

### **7.1 Lumped Parameter Extraction**

In the equivalent circuit models, some lumped elements—such as the 2 cc coupler and the radiation impedance—only depend on geometric dimensions and well-defined material properties (i.e. properties of air). Thus, their impedances can be accurately calculated. Some parameters—such as the compliance and the mass of the diaphragm, the resistance of the coil, and the transduction coefficient—depend on less controlled material properties. For example, the Young's modulus of the PDMS diaphragm, the density of the center mass, and the remnant magnetization of the magnet vary widely depending on processing conditions, etc. Thus, experimental extraction of these parameters is useful in order to get accurate analytical model predictions. The mechanical damping coefficient, which does not have a simple analytical solution, is usually extracted experimentally. In this section, the relevant lumped parameters are extracted in order to obtain accurate lumped element model predictions.

### 7.1.1 Electrical Impedance

The DC resistances of the coils are measured to be 1.1  $\Omega$  for Transducer 1 and 0.9  $\Omega$  for Transducer 2. The inductances of the winding coils are measured by a HP 4294 Impedance Analyzer. Data is acquired over a frequency range of 100 Hz to 1500 Hz. The inductances are 0.7  $\mu\text{H}$  and 0.6  $\mu\text{H}$  for Transducer 1 and Transducer 2 respectively, compared with calculated value of 0.24  $\mu\text{H}$  and 0.12  $\mu\text{H}$ . The inductive reactances are very small compared to the resistances at low frequencies and will be ignored in the simulation.

### 7.1.2 Diaphragm Impedance

After testing was complete, the mechanical mass of the rigid center mass/magnet was cut off of the diaphragm and directly measured using a digital balance (OHAUS Explorer Pro). The masses are  $0.029 \pm 0.001$  g and  $0.005 \pm 0.001$  g for Transducer 1 and Transducer 2, respectively. The total mass of the PDMS diaphragm is only  $1.5 \times 10^{-5}$  g and  $7.3 \times 10^{-6}$  g for Transducer 1 and Transducer 2, respectively, assuming the density of PDMS is  $1 \text{ kg/m}^3$  [75]. Since the mass of the PDMS is so much lower than the rigid center mass, the effective diaphragm mass is neglected (the second term in equation 6-23). In other words, the rigid center mass dominates the inertial inductance of the diaphragm  $M_{dm}$ .

The mechanical compliance  $C_{dm}$  and the resistance  $R_{dm}$  of the diaphragm are obtained indirectly by performing an impulse test. Figure 7.1 shows the setup of the impulse measurement. The transducers are first excited by inputting a dc current into the coil in order to achieve a static displacement. A mechanical switch, connected in series with the coil, is then switched off to open the electrical circuit. When the switch is turned off, the diaphragm will experience a damped natural oscillation, which is

measured by a laser vibrometer (Polytec MSV 300). The current signal is monitored by a Tektronix TCPA 300 current probe, and the current signal from on to off triggers measurement. The current in the coil stops flowing within a very short period of time; this electrical transient is much faster than the mechanical motion. Since the resulting oscillation is purely mechanical without electrical coupling, the time-series motion data can be used to extract the mechanical damping ratio and the damped resonant frequency according to [82], [91].

Figure 7-2 shows one example time-series data of the velocity of both Transducer 1 and Transducer 2. The initial velocity is zero as expected. The curve shows a characteristic under-damped system response. Assuming the  $v_1$  and  $v_2$  are velocities of two consecutive peaks, the damping ratio  $\zeta$  can be calculated by

$$\zeta = \frac{\delta}{\sqrt{\delta^2 + 4\pi^2}} \quad (7-1)$$

where

$$\delta = \ln\left(\frac{v_1}{v_2}\right) \quad (7-2)$$

Five different time-series data are recorded, and the extracted damping ratio are  $0.086 \pm 0.015$  and  $0.071 \pm 0.015$  for Transducer 1 and Transducer 2, respectively. The damped natural frequency  $f_d$  can also be derived directly from the same curve, which is the inverse of the time difference between the two consecutive peaks. The damped natural frequencies of the two devices are 556 Hz and 791 Hz for Transducer 1 and Transducer 2, respectively.

Using the damped natural frequency and the damping ratio, the natural frequency  $f_n$  of the diaphragm can be calculated by

$$f_n = \frac{f_d}{\sqrt{1-\zeta^2}} \quad (7-3)$$

The natural frequencies of the two devices are  $558.1 \pm 0.7$  and  $793.0 \pm 0.9$  Hz for Transducer 1 and Transducer 2, respectively. The natural frequency is also directly related to the mechanical mass and compliance of the diaphragm by

$$f_n = \frac{1}{2\pi\sqrt{M_{dm}C_{dm}}} \quad (7-4)$$

Thus, the compliance of the diaphragm of the two devices can be calculated by

$$C_{dm} = \frac{1}{M_{dm}(2\pi f_n)^2} \quad (7-5)$$

The calculated mechanical compliance for both Transducer 1 and Transducer 2 are  $0.0028 \pm 0.0012$  m/N and  $0.0078 \pm 0.0012$  m/N respectively. The equivalent diaphragm mechanical resistance can be calculated by

$$R_{dm} = 2\zeta\sqrt{\frac{M_{dm}}{C_{dm}}} \quad (7-6)$$

The corresponding acoustic parameters can then derived based on equation 6.10.

Using this procedure, the Young's modulus of the PDMS diaphragm estimated from the measured compliance (equation 6-22) is about 26 MPa, which is higher than the 0.4 – 2 MPa typically reported for bulk PDMS. The hardening of the thin PDMS film is potentially caused by the plasma that exposed during final release. It is reported that,

plasma can enhance the crosslinking of the PDMS on the surface to form a silica type of thin layer [92]. This thin layer subsequently increases the stiffness of PDMS diaphragm, especially for relatively thin diaphragms.

### 7.1.3 Transduction Coefficient

The remnant magnetization of the micromagnets in the devices is obtained by measuring the hysteresis loop of the micromagnets using a vibrating sample magnetometer (VSM), as shown in Figure 7-3. With the remnant magnetization, the radial magnetic flux density can be estimated by equation (6-15) or by finite element modeling. The total length of the coil for Transducer 1 and Transducer 2 are 18.1 and 9.3 mm, respectively. Therefore, the transduction coefficient can be calculated by

$$K = B_{avg} l_{coil} \text{ and } G = B_{avg} l_{coil} / S_{eff}.$$

Table 7-1 lists all the parameters used in the LEM model.

## 7.2 Acoustic Measurements

The acoustic measurements are performed using a Brüel and Kjær (B&K) PULSE Acoustic Characterization System. The experimental setup is shown in Figure 7-4. The microtransducer is mounted on one end of the 2 cc coupler (FRYE Electronics Inc. Model HA-1). A B&K microphone type 4138 is mounted on the other end of the coupler to record the sound pressure inside of the coupler. The PULSE system supplies a driving signal through a Techron 7540 power amplifier to the transducers. A Tektronix TCPA 300 current probe is used to measure the current flowing in the coils. The measured current signal is then input into PULSE as a reference signal to obtain the transfer function. The frequency response is then recorded in the frequency range of 100 Hz to 1200 Hz.

Figure 7-7 shows the results for the two devices. The devices show resonances at 575 Hz and 804 Hz, respectively. Although both devices show similar displacement response as shown in Chapter 5, the bigger Transducer 1 generates more sound pressure than Transducer 2 due to its larger diaphragm area. In the low-frequency flat band (~200 Hz), normalized sound pressure of 2.2 and 0.4 Pa/A are achieved, which corresponds a sound pressure level (SPL) of 101 and 86 dB for a 1 A drive current. The SPL is given by

$$SPL = 20 \log\left(\frac{P_{2cc}}{P_0}\right) \quad (7-7)$$

where  $P_0$  equals to 20  $\mu$ Pa. At the resonances, normalized sound pressure of 15 and 3.3 Pa/A, corresponding to SPL of 118 and 104 dB for a 1 A drive current, for Transducer 1 and Transducer 2, respectively. The simulation results from LEM are also shown on the same figures. The simulated resonances are 580 Hz and 790 Hz for Transducer 1 and Transducer 2, respectively. The values are very close to the measured results. Moreover, both curves match quite well except the amplitude at resonance. This indicates that the measured damping coefficients may be slightly larger than the true values. Since the measured damping coefficients have relatively large errors (Table 7-1), the amplitude difference at the resonance could also be attributed to experimental uncertainties.

### 7.3 Energy Harvesting Measurements

The experiment setup for energy harvesting measurements is shown in Figure 7-6. The devices are glued and wire-bonded onto a PCB. The whole PCB board is then fixed to a shaker (LDS Test& Measurement V408). An accelerometer (PCB Piezoelectronics

356A16) is also fixed on the shaker to measure the acceleration that generated by the shaker. The excitation amplitude is fixed at 1 g ( $9.8 \text{ m/s}^2$ ). The frequency response of the open-circuit voltage is recorded together with the acceleration signal using a spectrum analyzer (Stanford Research System model SR780).

Figure 7-7 shows the results for the two devices, where the unit of the acceleration  $g=9.8 \text{ m/s}^2$ . The devices show resonance at 530 Hz and 763 Hz, respectively, compared to 557 Hz and 785 Hz from the LEM simulation. The discrepancies between the model and experimental values are larger than the electroacoustic model. At resonance, normalized rms voltages of 13.2 and 5.6  $\mu\text{V/g}$  are measured. Again, the simulated results show lower amplitude at the resonance, potentially caused by the error of the measured damping coefficients. Assuming matched resistive load (i. e.  $P_{match} = V_{rms}^2 / (4 \cdot R_{coil})$ ) the corresponding power is 23.0 and 18.7 pW for Transducer 1 and Transducer 2, respectively. Off the resonance, the measured signal is noisy due to the weak response of the devices, which makes it difficult to compare with the simulated results. The errors on the resonant frequencies and the amplitude are likely caused by non-rigid mounting of the devices. The microdevices are bonded on a flat PCB board, which is then attached to the shaker by a screw. When the shaker is vibrating, the intermediate vibration of the PCB board may cause error between the measured acceleration signal and the actual acceleration applied to the device.

#### 7.4 Conclusion

The relevant transducer parameters used in the LEM are extracted in this chapter. The parameters are then used to obtain LEM model predictions. These predictions are compared against experimental measurements of the piston-type transducers, both as

an electroacoustic actuator and as a mechanoelectric generator. The acoustic performance of both the transducers match very well with the simulation, which provides good validation of the LEM model developed in Chapter 6. Compared to the acoustic performance, the energy harvesting performance deviates from the model, potentially due to experimental error in the measurements. While not performed here, a systematic uncertainty analysis on both the model parameters and experimental results would provide more quantitative validation of the model.

The acoustic performances of the devices indicate promising applications as microspeakers. However, the energy harvesting performances are so far, quite limited. With the LEM models, design optimization and improvements can be made to enhance the performance for applications.

Table 7-1. Extracted parameters for the piston-type transducers

Transducers	Transducer 1	Transducer 2
Coil Resistance ( $R_{coil}$ ) ( $\Omega$ )	1.1	0.9
Coil Inductance ( $L_{coil}$ ) ( $\mu\text{H}$ )	0.7	0.6
Total Length of Coil ( $l_{coil}$ ) (mm)	18.1	9.3
Radial Magnetic Flux Density ( $B_r$ ) (T)	0.0276	0.0167
Mechanical Transduction Coefficient ( $K$ ) (T·m)	$5.0 \times 10^{-4}$	$1.6 \times 10^{-4}$
Diaphragm Mechanical Compliance ( $C_{dm}$ ) (m/N)	$0.0028 \pm 0.0012$	$0.0078 \pm 0.0012$
Diaphragm Mechanical Mass ( $M_{dm}$ ) (g)	$0.029 \pm 0.001$	$0.0052 \pm 0.0008$
Diaphragm Mechanical Resistance ( $R_{dm}$ ) ( $\text{N} \cdot \text{s} / \text{m}^5$ )	$0.018 \pm 0.003$	$0.0037 \pm 0.0008$
Effective Area ( $S_{eff}$ ) ( $\text{m}^2$ )	$2.12 \times 10^{-5}$	$4.49 \times 10^{-6}$
Acoustic Transduction Coefficient ( $G$ ) (T/m)	23.6	35.6
Diaphragm Acoustic Compliance ( $C_{da}$ ) ( $\text{m}^5 / \text{Pa}$ )	$1.3 \times 10^{-12}$	$1.6 \times 10^{-13}$
Diaphragm Acoustic Mass ( $M_{da}$ ) ( $\text{kg} / \text{m}^4$ )	$1.74 \times 10^7$	$2.58 \times 10^5$
Diaphragm Acoustic Resistance ( $R_{da}$ ) ( $\text{N} \cdot \text{s} / \text{m}^5$ )	$3.9 \times 10^7$	$1.8 \times 10^8$
Damped Natural Frequency ( $f_d$ ) (Hz)	556.4	790.7
Natural Frequency ( $f_n$ ) (Hz)	$558.1 \pm 0.7$	$793.0 \pm 0.9$

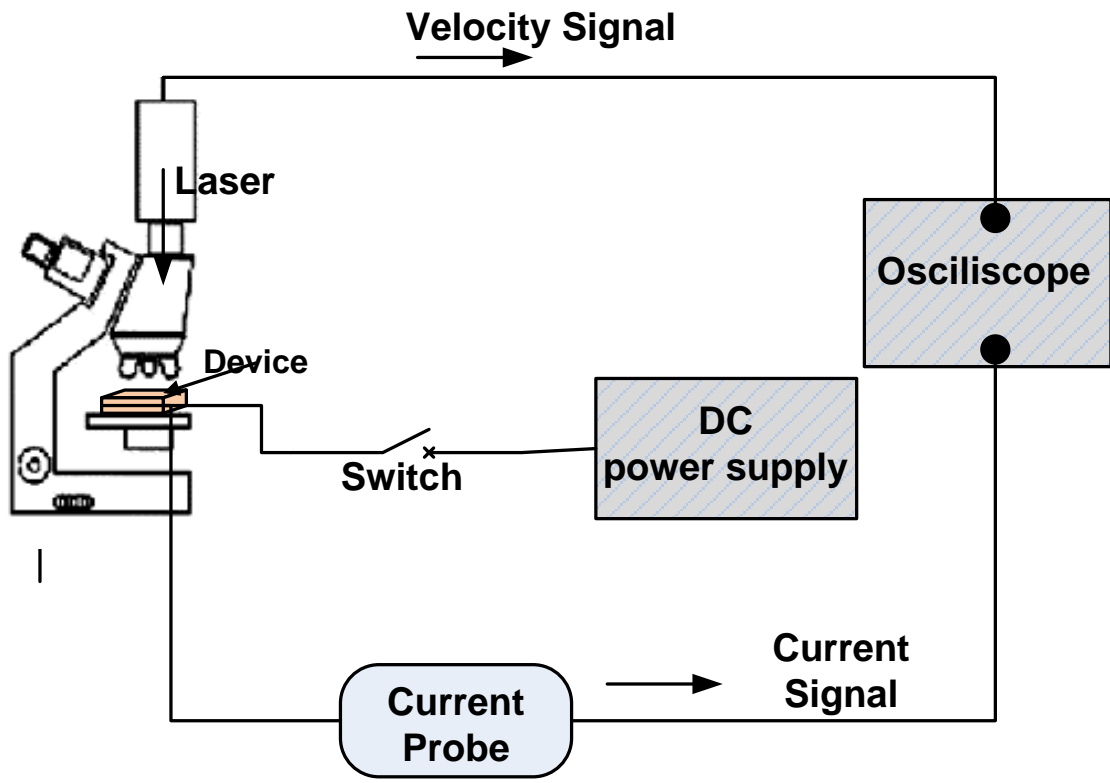


Figure 7-1. Experiment setup for the impulse response test

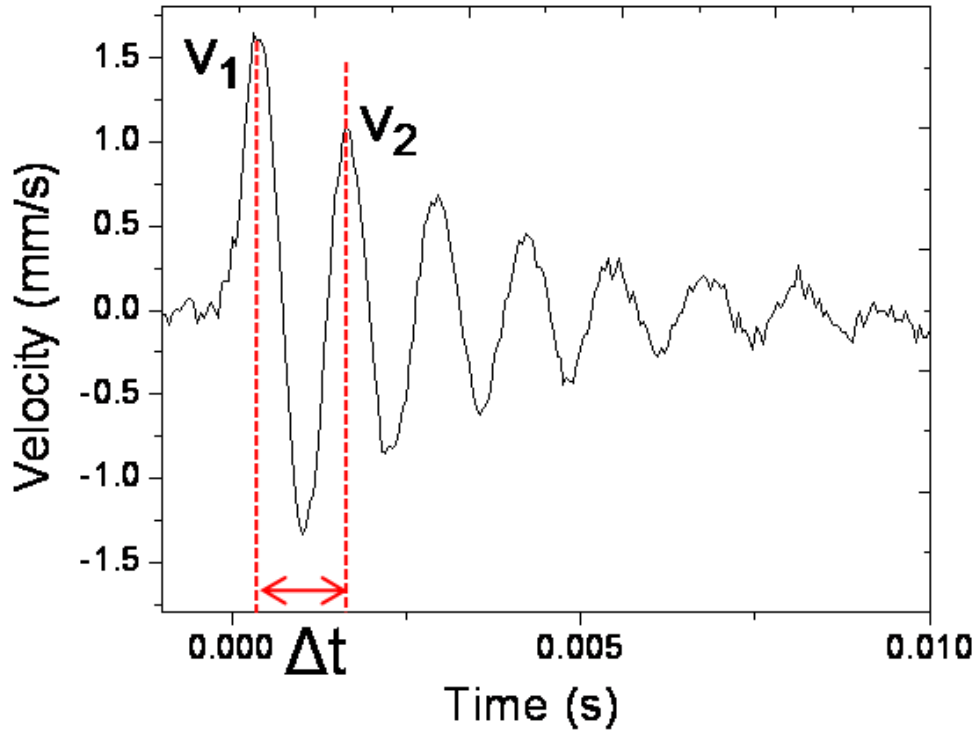
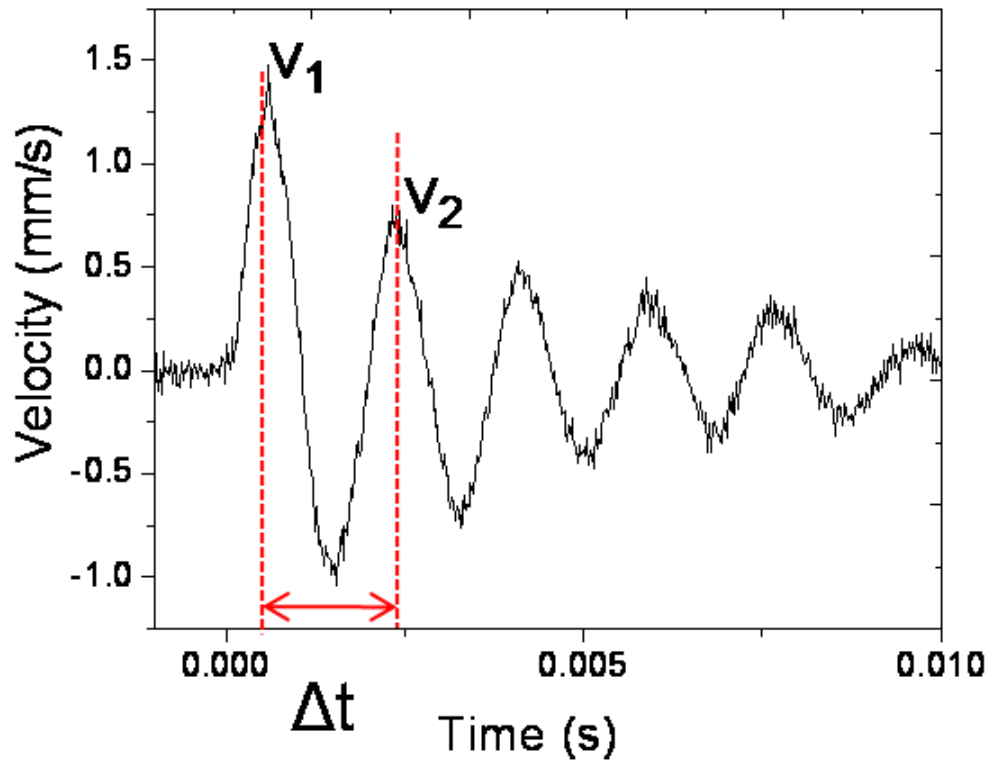


Figure 7-2. Results of the impulse response test of A) Transducer 1 and B) Transducer 2

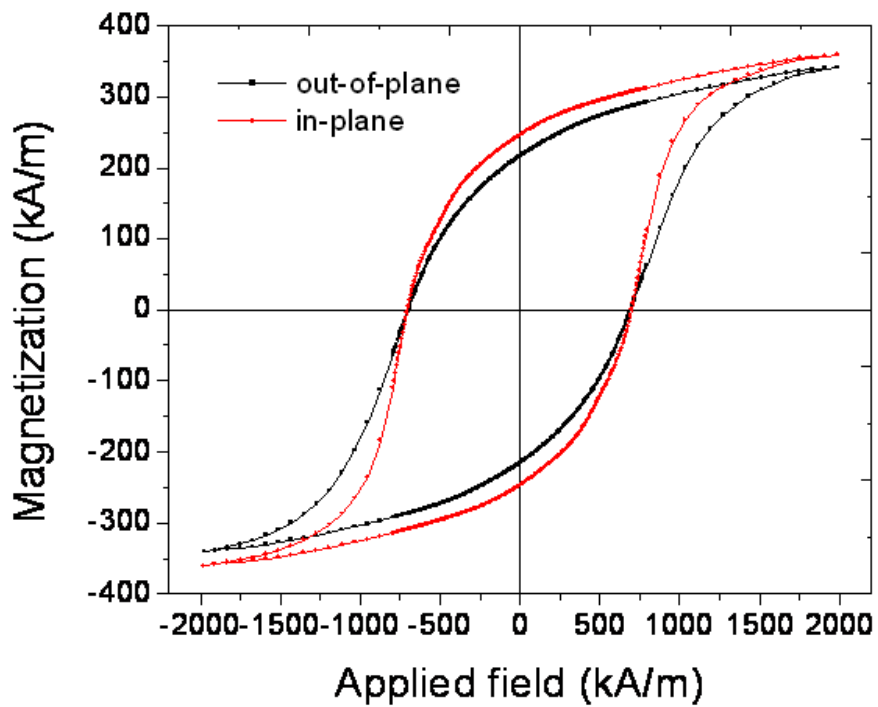


Figure 7-3. A typical magnetic hysteresis loop (disk with 1.8mm diameter and 0.36 mm thickness)

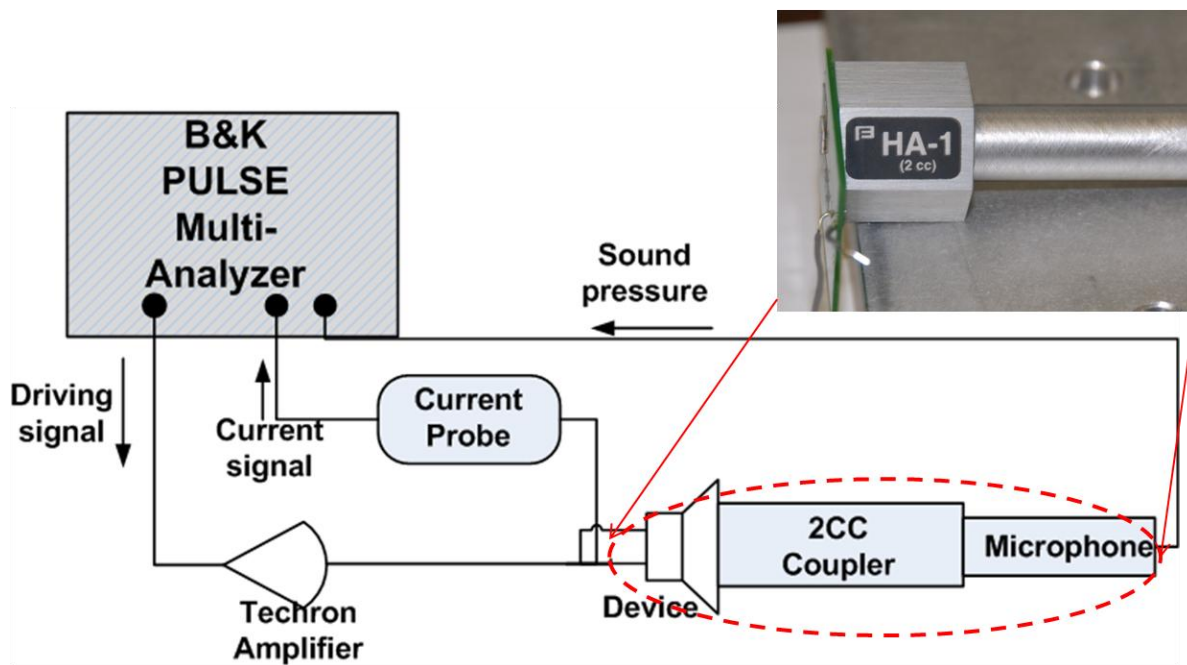


Figure 7-4. Experiment setup for acoustic measurements.

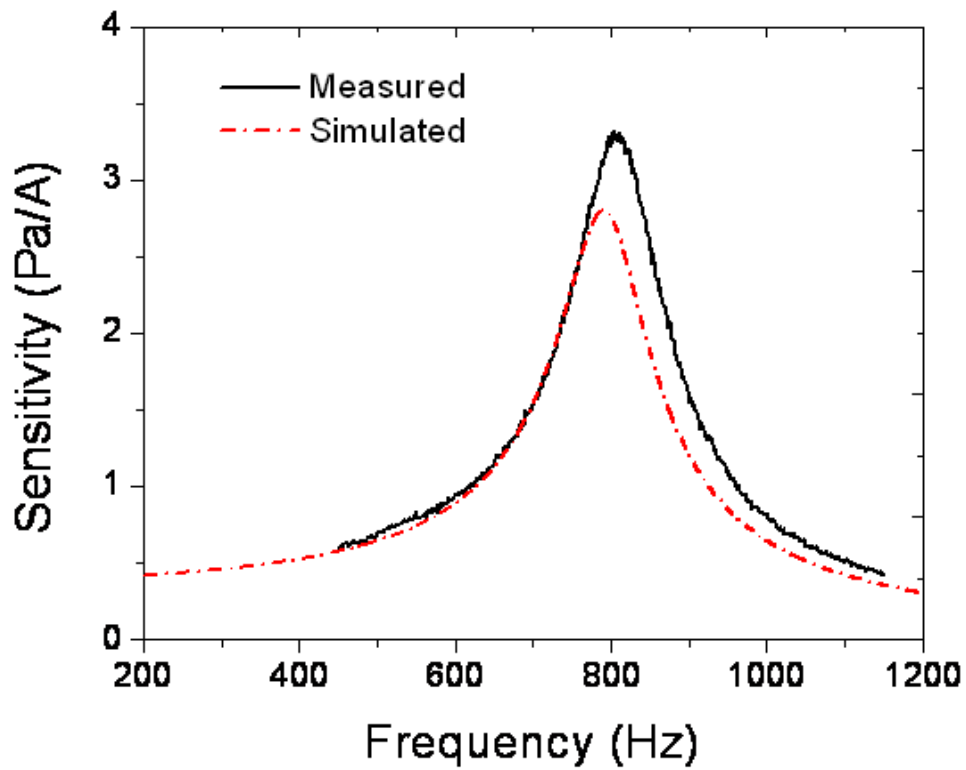
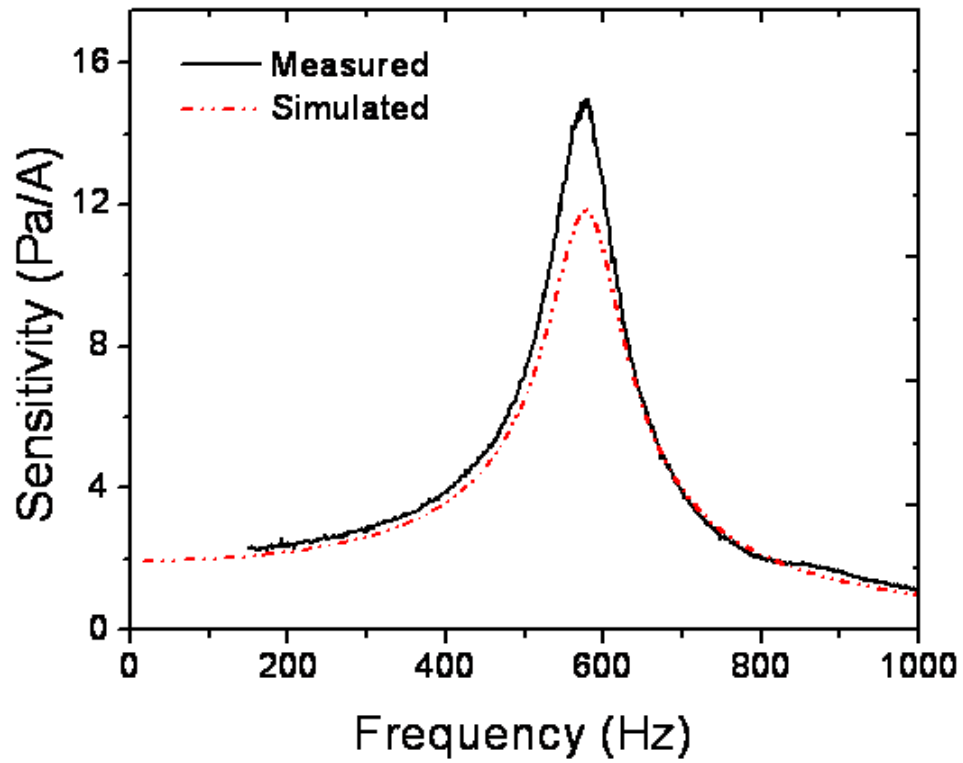


Figure 7-5. Acoustic measurement results and simulated results of A) Transducer 1 and B) Transducer 2.

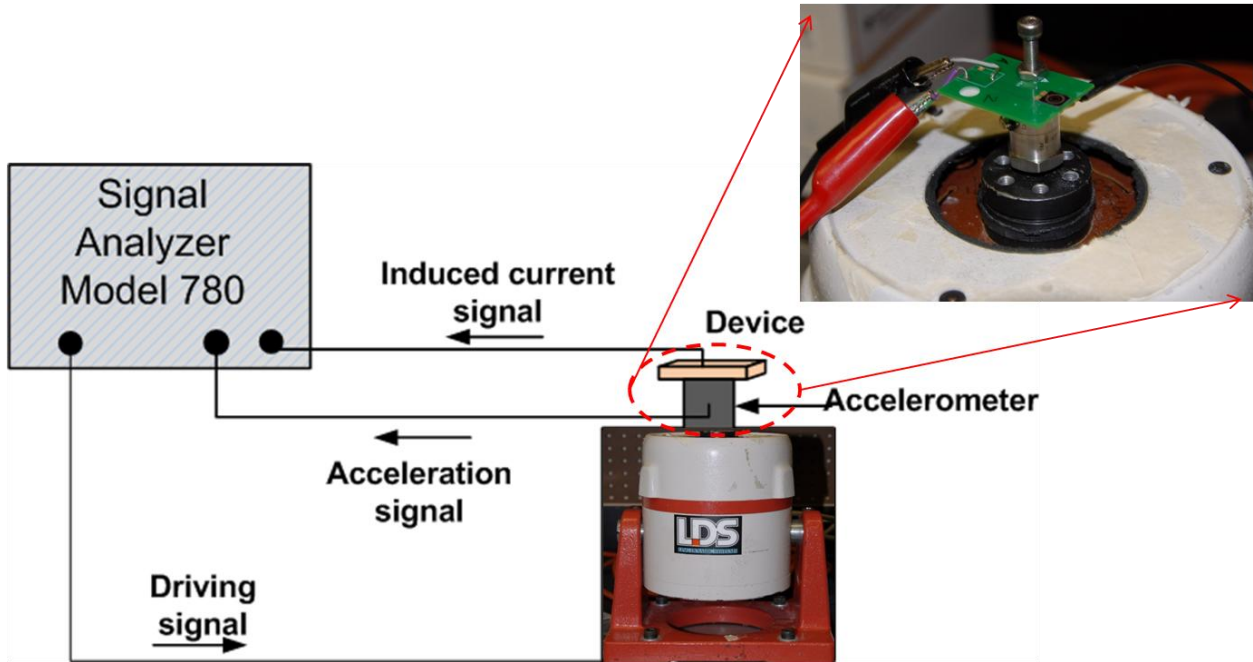


Figure 7-6. Experiment setup for energy harvesting measurements

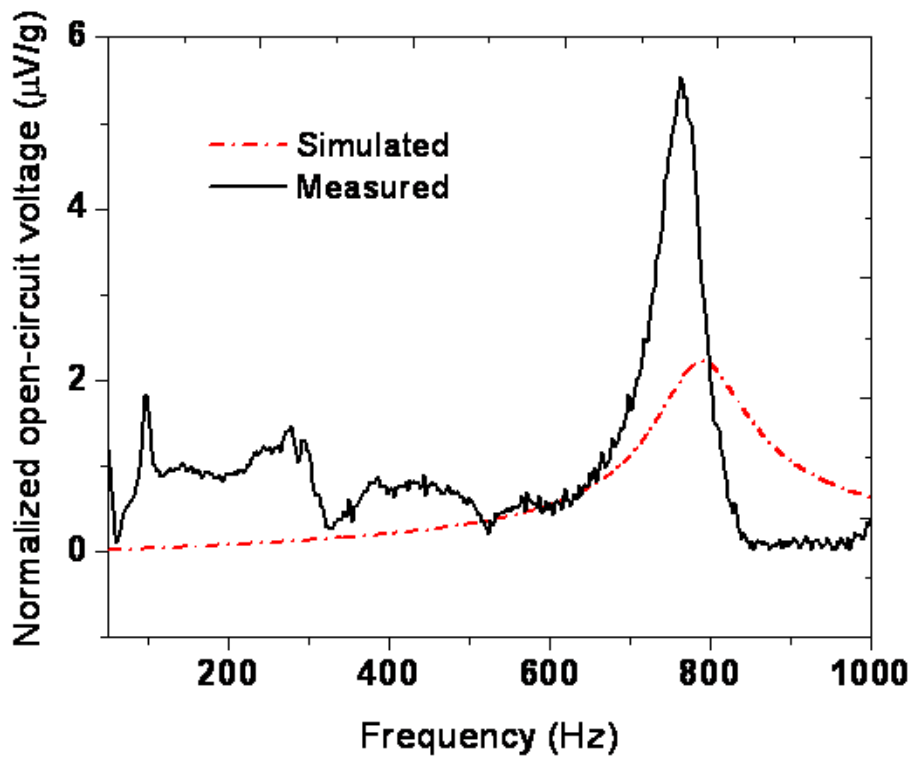
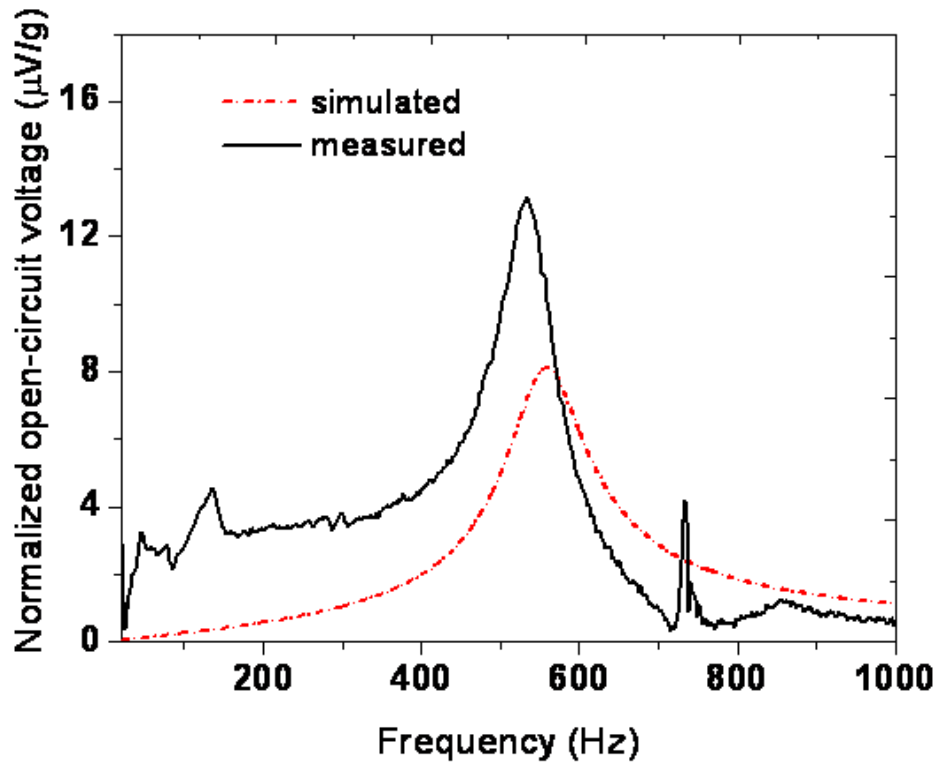


Figure 7-7. Open-circuit voltage response of A) Transducer 1 and B) Transducer 2.

## CHAPTER 8 CONCLUSION AND FUTURE WORK

### 8.1 Summary and Conclusion

Magnetic MEMS transducers involving permanent micromagnets have attracted great attention in the past decades due to their favorable scaling, good energy density, non-contact/remote actuation capability, robustness, and other system-level advantages. However, fabrication and integration of thick, high-energy-product, permanent-magnet materials into MEMS transducers have been a major hindrance. Thus the objective of this work was to develop methods for wafer-level microfabrication of thick (10-100+  $\mu\text{m}$ ), high-performance, PM materials and to demonstrate the integration of these micromagnets in fully batch-fabricated magnetic MEMS transducers.

Two methods were developed to fabricate micromagnets. First, a technique Co-rich Co–Pt magnets were electroplated into patterned arrays with thicknesses  $\sim 10 \mu\text{m}$  on textured and un-textured Cu seed layer. It was shown that enhanced magnetic properties were obtained on both seed layers by careful selection of electroplating conditions. The coercivity and maximum energy product reached as high as 330 kA/m and 64.0 kJ/m<sup>3</sup>, respectively.

The second method was to micro-pack wax-bonded magnets embedded in pre-etched structures with feature sizes of 100  $\mu\text{m}$  - 1 mm. The incorporation of the wax binder was shown to greatly improve the micromagnet coercivity over the raw dry-packed powder (from 287 to 737 kA/m) without detrimental reduction of the magnetic strength. Using this method, 500  $\mu\text{m}$  x 500  $\mu\text{m}$  x 320  $\mu\text{m}$  magnets were demonstrated with a coercivity of 737 kA/m and a maximum energy product of 16.6 kJ/m<sup>3</sup>.

Then, wax-bonded powder Nd–Fe–B permanent magnets were integrated into functional MEMS transducers in order to demonstrate the utility of these magnets for electrodynamic transduction. Both cantilever- and piston-type microtransducers were fabricated using batch MEMS fabrication processes. Initially, the actuation response was measured to verify their functionality. Vertical deflections of 2.66  $\mu\text{m}$  and 2.2 $\mu\text{m}$  were achieved (in the sub-resonant flat band) by cantilever-type and piston-type actuators, respectively, with input currents of 5.5 mA<sub>rms</sub> and 670 mA<sub>rms</sub>.

Then two complete LEM circuits were developed to simulate two different piston-type microtransducer designs in two different operating modes: (1) as an electroacoustic actuator and (2) as a mechanoelectric generator. In order to validate the models, the relevant transducer parameters used in the LEM were experimentally extracted. The parameters were then used to obtain LEM model predictions. These predictions were compared against experimental measurements of the piston-type transducers operating as a microspeaker and as a vibrational energy harvester. The acoustic performances of both transducers matched very well with the simulation, which provides good validation of the LEM. The measured energy harvesting performance deviated from the model, potentially due to experimental error in the measurements.

The acoustic performances of the devices indicate promising applications as microspeakers. However, the energy harvesting performances are so far, quite limited. With the demonstration of fabrication methods and the predictive capability of LEM, design optimization and improvements can be made to enhance the performance for applications.

## 8.2 Suggested Future Work

There are several areas that can be investigated to extend this work. Firstly, the electroplated Co-rich Co–Pt magnets show excellent magnetic properties. However, reliably achieving films thicker than 10  $\mu\text{m}$  is limited so far by finding a stable photoresist that can survive (dissolution and delamination) the alkaline electroplating bath. Thus, finding a more stable plating mask for electroplating Co–Pt magnets is important for future integration of this material into functional magnetic transducers. However, even using the magnets with current thickness, some small scale ( $\sim 100 \mu\text{m}$ ) transducers could be designed for certain applications. In addition, systematic structure-property relation investigations, such as the structure of the seedlayer, the structure of the Co–Pt films, and the role of seedlayer on the texture of the Co–Pt films will be helpful to further improve the properties of the films.

Secondly, the validated LEM models can be used to further optimize the performance of the devices. For example, the piston-type microtransducer acting as a speaker shows reasonably high sound pressure level. However, the bandwidth ( $< 1 \text{ kHz}$ ) is too small for audio applications. Thus, a systematic optimization can be performed to optimize both the bandwidth and SPL. Practically, the bandwidth can be increased by decreasing the size of the PDMS diaphragm, and the SPL can be enhanced by simply increasing the numbers of coil turns.

Lastly, other magnetic MEMS transducers, such as switches, valves, pumps, synthetic jets, flaps, motors, linear actuators, etc can be developed based on the magnets, fabrication processes, and LEM models developed in this work. It is hoped that this work provides some level “proof” that magnetic MEMS are not just possible, but that there is a wide frontier for future investigation.

## LIST OF REFERENCES

- [1] S. D. Senturia, *Microsystem Design*, Norwell, MA: Kluwer Academic Publishers, 2000.
- [2] M. J. Madou, *Fundamentals of Microfabrication: The Science of Miniaturization*, Boca Raton, FL: CRC Press, 2002.
- [3] J. W. Judy, "Microelectromechanical systems (MEMS): fabrication, design and applications." *Smart of Mater. Struct.*, vol. 10, pp. 1115-1134, 2001.
- [4] D. Niarchos, "Magnetic MEMS: key issues and some applications" *Sensors and Actuators A*, vol. 109, pp. 166-173, 2003.
- [5] O. Cugat, J. Delamare, and G. Reyne, "Magnetic micro-actuators and systems (MAGMAS)," *IEEE Trans.*, vol. 39, pp. 3607-3612, 2003.
- [6] P. J. Grundy, "Thin film magnetic recording media," *J. Phys. D: Appl. Phys.*, vol.31, pp. 2975-2990, Nov. 1998.
- [7] D. Weller, "Extremely high-density longitudinal magnetic recording media," *Annu. Rev. Mater. Sci.*, vol. 30 pp 611-644, 2000.
- [8] H. Guckel, "Progress in electromagnetic actuators," in *Proceedings Actuator'96*, 1996, Bremen, Germany, pp. 45-48.
- [9] R. C. O'Handley, *Modern Magnetic Materials, Principles, and Applications*. New York: Wiley-Interscience, 2000.
- [10] B. D. Cullity and C. D. Graham, *Introduction to Magnetic Materials*. Oxford Univ. Press, 2008.
- [11] P. Campbell, *Permanent Magnet Materials and their Application*. U. K.: Cambridge Univ. Press, 1994.
- [12] E. P. Furlani, *Permanent Magnet and Electromechanical Devices: Materials. Analysis and Applications*, New York: Academic Press, 2001.
- [13] R. Skomski and J. M. D. Coey, *Permanent Magnetism*, Bristol, UK ; Philadelphia, PA : Institute of Physics Pub., 1999.
- [14] M. Yue, J. X. Zhang, W. Q. Liu, and G. P. Wang, "Chemical stability and microstructure of Nd-Fe-B magnet prepared by spark plasma sintering," *J. Magn. Mater.*, vol. 271, pp. 364-368, May 2004.
- [15] Magnetic Materials Producers Association, MMPA Standard No. 0100-00, Standard Specifications for Permanent Magnet Materials, 2000. [Accessed Feb. 2009]. [Online]. Available: <http://www.intl-magnetics.org/>.

- [16] Electron Energy Corp. Ultra-High Temperature Samarium Cobalt Magnets product datasheets. 2000. [Accessed May. 2009]. [Online]. Available: <http://www.electronenergy.com/>.
- [17] T. S. Chin, "Permanent magnet films for applications in microelectromechanical systems," *J. Magn. Magn. Mater.*, vol. 209, pp.75-79, Feb. 2000.
- [18] N. V. Myung, D. Y. Park, B. Y. Yoo, and P. T. A. Sumodjo, "Development of electroplated magnetic materials for MEMS," *J. Magn. Magn. Mater.*, vol. 265, pp.189-198, 2003.
- [19] S. Guan and B. J. Nelson, "Pulse-reverse electrodeposited nanograined CoNiP thin films and microarrays for MEMS actuators." *J. Electrochem. Soc.*, vol.152 (4), pp. C190-C195, 2005.
- [20] T.M. Liakopoulos, W. Zhang, and C.H. Ahn, "Micromachined thick permanent magnet arrays on silicon wafers," *IEEE Trans. Magn.*, vol. 32, pp. 5154-5156, Sep. 1996.
- [21] S. Guan and B. J. Nelson, "Electrodeposition of low residual stress CoNiMnP hard magnetic thin films for magnetic MEMS actuators." *J. Magn. Magn. Mater.*, vol. 292, pp.49-58, Apr. 2005.
- [22] Y. Su, H. Wang, G. Ding, F. Cui, W. Zhang, and W. Chen, "Electroplated hard magnetic materials and its application in microelectromechanical systems," *IEEE Trans. Magn.*, vol. 41, no. 12, pp. 4380-4383, Dec. 2005.
- [23] W. B. Ng, A. Takada, and K. Okada, "Electrodeposited Co-Ni-Re-W-P thick array of high vertical magnetic anisotropy," *IEEE Trans. Magn.*, vol. 41, no. 10, pp. 3886-3888, 2005.
- [24] F. M. F. Rhen, G. Hinds, C. O'Reilly, and J. M. D. Coey, "Electrodeposited FePt films." *IEEE Trans. Magn.*, vol.39 (5), pp. 2699-2701, Sep. 2003.
- [25] K. Leistner, J. Thomas, H. Schlörb, M. Weisheit, L. Schultz, and F. Fähler, "Highly coercive electrodeposited FePt film by post annealing in hydrogen." *Appl Phys. Lett.*, vol. 85(16), pp.3498-3500, Oct. 2004.
- [26] S. Thongmee, J. Ding, J. Y. Lin, and D. J. Blackwood, J. B. Yi and J. H. Yin, "FePt films fabricated by electrodeposition." *J. Appl. Phys.*, vol.101, pp. 09K519, Jul. 2007.
- [27] W. F. Liu, S. Suzuki, D. S. Li, and K. Machida, "Magnetic properties of Fe-Pt thick-film magnets prepared by RF sputtering," *J. Magn. Magn. Mater.*, vol. 302, pp.201-205, Jul. 2006.
- [28] M. Nakano, S. Shibata, T. Yanai, and H. Fukunaga, "Anisotropic properties in Fe-Pt thick film magnets," *J. Appl. Phys.*, vol. 105, pp. 07A732, Mar. 2009.

- [29] O. Berkh, Y. Rosenberg, Y. S. Diamand, and E. Gileadi, "Electrodeposited near-equiatom CoPt thick films," *Electrochem. Solid-State Lett.*, vol. 11, pp. D38-D41, 2008.
- [30] S. Franz, M. Bestetti, M. Consonni, and P. L. Cavallotti, "Electrodeposition of micromagnets of CoPtW(P) alloys," *Microelectronic Eng.*, vol. 64, pp. 487-494, Oct. 2002.
- [31] I. Zana, G. Zangari, and M. Shamsuzzoha, "Enhancing the perpendicular magnetic anisotropy of Co-Pt(P) films by epitaxial electrodeposition onto Cu(111) substrates," *J. Magn. Magn. Mater.*, vol. 272-276292, pp.c1775266-c1776280, Apr. 2005.
- [32] L. Vieux-rochaz, d. Dieppedale, B. Desloges, D. Gamet, C. Barragatti, h. Rostaing, and J. Meunier-Carus, "Electrodeposition of hard magnetic CoPtP materials and integration into magnetic MEMS," *J. Micromech, Microeng.*, vol. 16, pp. 219-224, Feb. 2006
- [33] S. Kulkarni and S. Roy, "Development of nanostructured, stress-free Co-rich CoPtP films for magnetic microelectromechanical system applications," *J. Appl. Phys.*, vol. 101, pp.09K524, May. 2007.
- [34] O. Berkh, Y. Rosenberg, Y. S. Diamand, and E. Gileadi, "Deposition of CoPtP films from citric electrolyte," *Microelectronic Eng.*, vol. 84, pp. 2444-2449, Nov. 2007.
- [35] C. Prados, A. Hernando, G. C. Hadjipanayis, and J. M. Gonzalez, "Coercivity analysis in sputtered Sm-Co thin films." *J. Appl. Phys.* 85(8):6148-615, Apr. 1999.
- [36] F.J. Cadieu, L. Chen, and B. Li, "Enhanced magnetic properties of nanophase SmCo<sub>5</sub> film dispersions," *IEEE Trans. Magn.*, vol. 37, no. 4, pp. 2570-2572, Jul. 2001.
- [37] E. Pina, F. J. Palomares, M. A. Garcia, F. Cebollada, A. de Hoyos, J. J. Romero, A. Hernaodo, and J. M. Gonzalez, "Coercivity in SmCo hard magnetic films for MEMS application," *J. Magn. Magn. Mater.*, vol. 290-291, pp. 1234-1236, Apr. 2005.
- [38] T. Budde and H. H. Gatzel, "Thin film Sm-Co magnets for use in electromagnetic microactuators." *J. Appl. Phys.*, vol. 99, pp.08N304, Apr. 2006.
- [39] A. Walther, D. Givord, N.M. Dempsey, K. Khlopkov, and O. Gutfleisch, "Structural, magnetic, and mechanical properties of 5 μm thick SmCo films suitable for use in microelectromechanical systems," *J. Appl. Phys.*, vol. 103, pp. 043911, Feb. 2008.

- [40] K. Yamasawa, X. Liu, and A. Morisako, "Nd-Fe-B films with perpendicular magnetic anisotropy," *J. Appl. Phys.*, vol. 99, pp. 08N302-4, Apr. 2006
- [41] L. Castaldi, M. R. F. Gibbs, and H. A. Davies, "Effect of the target power and composition on RE-Fe-B thin films with Cu and Nb buffer and cap layers." *J. Appl. Phys.*, vol.100, pp.093904, Apr. 2006.
- [42] N. M. Dempsey, A. Walther, F. May, D. Givord, K. Khlopkov, and O. Gutfleisch, "High performance hard magnetic Nd-Fe-B thick films for integration into micro-electro-mechanical systems," *App. Phys. Lett.*, vol. 90, pp.092509, Mar. 2007.
- [43] A. Walther, C. Marcoux, B. Desloges, R. Grechishkin, D. Givord, and N. M. Dempsey, "Micro-patterning of NdFeB and SmCo magnet films for integration into micro-electro-mechanical-systems," *J. Magn. Magn. Mater.*, vol. 321, pp. 590-594, 2008.
- [44] M. Nakano, S. Sato, H. Fukunaga, and F. Yamashita, "A method of preparing anisotropic Nd-Fe-B film magnets by pulsed laser deposition," *J. Appl. Phys.*, vol. 99, pp. 08N301, Apr. 2006.
- [45] S. Guan, B. J. Nelson, and K. Vollmers, "Electrochemical codeposition of magnetic particle-ferromagnetic matrix composites for magnetic MEMS actuator applications." *J. Electrochem. Soc.*, vol. 151(9), pp. C545-C549, 2004.
- [46] S. Guan and B. J. Nelson, "Magnetic composite electroplating for depositing micromagnets." *J. Microelectromech. Syst.* Vol. 15(2), pp. 330-337, Apr.2006.
- [47] L. K. Lagorce and M. G. Allen, "Magnetic and mechanical properties of micromachined strontium ferrite/polyimide composite," *J. Microelectromech. Syst.*, vol. 6, pp. 307-312, Dec. 1997.
- [48] Z. C. Yuan, A. J. Williams, T. C. Shields, S. Blackburn, C. B. Ponton, J. S. Abell, and I. R. Harris, "The production of Sr hexaferrite thick films by screen printing," *J. Magn. Magn. Mater.*, vol. 247, pp. 257-269, Jun. 2002.
- [49] H. J. Cho and C. H. Ahn, "Microsclae resin-bonded permanent magnets for magnetic micro-electro-mechanical systems applications," *J. Appl. Phys.*, vol. 93, pp. 8674-8676, May. 2003.
- [50] Y. I. Rozenberg, V. Krylov, G. Belitsky, and Y. S. Diamand, "Resin-bonded permanent magnetic films with out-of-plane magnetization for MEMS applications," *J. Magn. Magn. Mater.*, vol. 305, pp. 357-360, Oct. 2002.
- [51] B. M. Dutoit, P. A. Bese, H. Blanchard, L. Guérin, and R. S. Popovich, "High performance micromachined Sm<sub>2</sub>Co<sub>17</sub> polymer bonded magnets." *Sens.& Actuat.*, vol.77, pp.178-182, Nov. 1999.

- [52] B. J. Bowers, J. S. Agashe, and D. P. Arnold "A method to form bonded micromagnets embedded in silicon." In *Proc. 14 th Int. Conf. Solid-State Sensors, Actuators, and Micro-systems* (Transducers '07), Lyon, France, June 2007, vol.2, 1581-1584.
- [53] B. Pawlowski, S. Schwarzer, A. Rahmig, and J. Töpfer, "NdFeB thick films prepared by tape casting," *J. Magn. Magn. Mater.*, vol. 265, pp. 337-344, Oct. 2003.
- [54] B. Pawlowski and J. Töpfer, "Permanent magnetic Nd-Fe-B thick films." *J. Mat. Sci.* vol.39, pp.1321-1324, Feb. 2004.
- [55] S. Schwarzer, B. Pawlowski, A. Rahmig, and J. Töpfer, "Permanent magnetic thick films from remanence optimized NdFeB-inks," *J. Mat. Sci.* vol. 15, pp. 165-168, Mar. 2004.
- [56] S. Guan, B. J. Nelson, and K. Vollmers, "Electrochemical codeposition of magnetic particle-ferromagnetic matrix composites for magnetic MEMS actuator applications." *J. Electrochem. Soc.*, vol. 151(9), pp. C545-C549, 2005.
- [57] J.J. Romero, R. Cuadrado, E. Pina, A. de Hoyos, F. Pigazo, F. L. Palomares, A. Hernando, R. Sastre, and J. M. Gonzalez, "Anisotropic polymer bonded hard-magnetic films for micro-electromechanical system applications." *J. Appl. Phys.* 99:08N303, 2006.
- [58] I. Zana and G. Zangari, "Electrodeposition of Co-Pt Films with High perpendicular Anisotropy," *Electrochemical and Solid-state Letters*, vol. 6, no. 12, pp. C153-C156, 2003.
- [59] I. Zana, G. Zangari, and M. Shamsuzzoha, "Enhancing the perpendicular magnetic anisotropy of Co-Pt(P) thin films by epitaxial electrodeposition onto Cu(111) substrates," *J. Magnetism and Magn. Mat.*, vol. 292, pp. 266-280, 2005.
- [60] G. Pattanaik, J. Weston, and G. Zangari, "Magnetic Properties of Co-rich Co-Pt Thin Films Electrodeposited on a Ru underlayer," *J. of Appl. Phys.*, vol 99, pp. 08E901, 2006.
- [61] G. Pattanaik, G. Zangari, and J. Weston "Perpendicular anisotropy in electrodeposited, Co-rich Co - Pt films by use of Ru underlayers," *Appl. Phys. Lett.*, vol. 89, pp. 112506, 2006.
- [62] P. L. Cavallotti et al., "Electrodeposition of magnetic multilayers," *Surf. Coat. Technol.*, vol. 105, pp. 232-239, 1998.
- [63] H. Jiang et al., "Epitaxial growth of Cu(111) films on Si(110) by magnetron sputtering: orientation and twin growth," *Thin Solid Films*, vol. 315, pp. 13-16, 1998.

- [64] P. Bruno, "Magnetic surface anisotropy of cobalt and surface roughness effects within Neel's model," *J. Phys. F*, vol. 18, pp. 1291-1298, 1988.
- [65] Neo Material Technologies, MQP-S-11-9-20001-070 isotropic powder. 2009. [Accessed Jan. 2010]. [Online]. Available: <http://www.amr-ltd.com/>.
- [66] D. J. Bell, T. J. Lu, N. A. Fleck, and S. M. Spearing, "MEMS actuators and sensors: observations on their performance and selection for purpose," *J. Micromech. Microeng.*, vol. 15, pp. S153-S164, 2005.
- [67] M. Khoo and C. Liu, "Micro magnetic silicone elastomer membrane actuator," *Sensor and Actuator A*, vol.89, pp. 259-266, 2001.
- [68] D. Bhailis, C. Mruuay, M. duffy, J. alderman, G. Kelly, and S. C. O Mathuna, "Modelling and analysis of a magnetic microactuator," *Sensors and Actuators A*, vol. 81, pp. 285-289, 2000.
- [69] B. Wagner, W. Benecke, G. Engelmann, and J. Simon, "Microactuators with moving magnets for linear, torsional or multi-axial motion," *Sensor and Actuators A*, vol. 32, pp.598-603, 1992.
- [70] H. J. Cho and C. H. Ahn, "A bidirectional magnetic microactuator using electroplated permanent magnet arrays," *J. Microelectromech. Syst.*, vol. 11, pp. 78-84, 2002.
- [71] C. Dieppedale, B. Desloges, H. Rostaing, J. Delamare, O. Gugat, and J. Meunier-Carus, "Magnetic bistable micro-actuator with integrated permanent magnets," in *Proc. IEEE Sensor*, Oct. 2004, pp. 493-496.
- [72] L. K. Lagorce, O. Brand, and M. G. Allen, "Magnetic microactuators based on polymer magnets," *J. Microelectromech. Syst.*, vol, 8, pp. 2-9. 1999.
- [73] J. Sutanto, A. D. Papania, Y. H. Berthelot, and P. J. Hesketh, "Dynamic characteristics of membrane displacement of a bidirectional electromagnetic microactuator with microcoil fabricated on a single wafer," *Microelectronic Engineering*, vol. 82, pp. 12-27, June 2005.
- [74] J. Sutanto, P. J. Heskth, and Y. H. Berthelot, "Design, microfabrication and testing of a CMOS compatible bistable electromagnetic microvalve with latching/unlatching mechanism on a single wafer," *J. Microeng. Micromech.*, vol. 16, pp. 266-275, Jan. 2006.
- [75] D. Armani, C. Liu, and N. Aluru, "Re-configurable fluid circuits by PDMS elastomer micromachine," *MEMS '99*, Orlando, FL, USA, 17-21 January 1999, pp. 222-227.
- [76] Para Tech Coating, Inc. Parylene Technology. 2008. [Accessed July, 2009]. [Online]. Available: <http://www.parylene.com/>.

- [77] S. Serre, A. Perez-Rodriguez, N. Fondevilla, E. Martincic, S. Martinez, J. R. Monrante, J. Montserrat, and J. Esteve, "Design and implementation of mechanical resonators for optimized inertial electromagnetic microgenerators," *Microsys. Technol.*, vol. 14, pp. 653-658, Dec. 2008.
- [78] M. Rossi, *Acoustics and Electroacoustics*, Artech House: Norwood, MA, pp. 245-308, 1988.
- [79] H. A. C. Tilmans, "Equivalent circuit representation of electromechanical transducers: I. Lumped-parameter systems," *J. Microeng. Micromech.*, vol. 6, pp. 157-176, 1996.
- [80] J. D. Kraus, *Electromagnetics*, 4<sup>th</sup> edn, New York: McGraw-Hill, pp. 420-472, 1992.
- [81] W. C. Young and R. G. Budynas, *Roark's Formulas for stress and strain*. 7<sup>th</sup> ed., New York: McGraw-Hill, 2002.
- [82] J. S. Agashe, "Modeling, design and optimization of electrodynamic ZNMF actuators," Ph.D dissertation, ECE, University of Florida, Gainesville, FL, 2009.
- [83] V. Lavinac, N. Erceg, and D. Kotnik-Karuza, "Magnetic field of a cylindrical coil," *Am. J. Phys.*, vol. 74, pp. 621-627, 2006.
- [84] F. W. Grover, *Inductance Calculations: Working Formulas and Tables*, New York: Dover Pulication, Inc., pp. 110, 1946.
- [85] S. A. N. Prasad, W. Gallas, S. Horowitz, B. Homeijer, B. B. Sankar, L. N. Cattafesta, and M. Sheplak, "Analytical electroacoustic model of a piezoelectric composite circular plate," *AIAA Journal*, vol. 44, no. 10, pp. 2311-2318, Oct. 2006.
- [86] J. S. Agashe and D. P. Arnold, "A study of scaling and geometry effects on the forces between cuboidal and cylingdrical magnets using analytical force solution," *J. Phys. D: Appl. Phys.*, vol. 41, pp. 105001, Apr. 2008.
- [87] D. Craik, *Magnetism-principle and applications*, New York: Wiley, pp. 335, 1995.
- [88] A. I. Rusinov, "High precision computation of solenoid magnetic fields by Garrett's methods," *IEEE Trans. Magn.*, vol. 30, pp. 2685-2688, 1994.
- [89] D. P. Arnold, "Review of microscale magnetic power generation," *IEEE Trans. Magn.*, vol. 43, pp. 3940-3951, 2007.
- [90] D. T. Blackstock, *Fundamentals of Physical Acoustics*, New York: John Wiley & Sons Inc, 2000.

- [91] A. Hadjian and C. Norwalk, *An Extension of the Log-decement Method*. Seismic Engineering, 1987.
- [92] S. Befahy, P. Lipnik, T. Pardoen, C. Nascimento, B. Patris, P. Bertrand, and S. Yunus, "Thickness and elastic modulus of plasma treated PDMS silica-like surface layer," *Langmuir*, vol. 26, pp. 3372-3375, Oct. 2010.

## BIOGRAPHICAL SKETCH

Naigang Wang received a bachelor's degree in materials science and engineering from Jilin University, Changchun, China, in 1999 and a master's degree in materials science and engineering from Virginia Tech, Blacksburg, VA, in 2005. He started the doctoral degree in materials science and engineering at the University of Florida, Gainesville, FL, in 2006.